Integrative, three-dimensional *in silico* modeling of gas exchange in the human alveolus
Integrative, dreidimensionale *in silico* Modellierung des Gasaustauschs in der menschlichen Alveole

Dissertation zur Erlangung des naturwissenschaftlichen Doktorgrades
Julius-Maximilians-Universität Würzburg
Fakultät für Biologie
Center for Computational and Theoretical Biology

vorgelegt von

Kerstin Schmid

aus

Mannheim

Würzburg, March 11, 2024

Eingereicht am:

Mitglieder des Promotionskomitees:

Vorsitzende/r:
1. Betreuerin: Prof. Dr. Sabine C. Fischer
2. Betreuer: Prof. Dr. Christian Stigloher
3. Betreuer: Prof. Dr. Andreas C. Hocke

Tag des Promotionskolloquiums:

Doktorurkunden ausgehändigt am:

Danksagung

Zuallererst möchte ich mich bei Professorin Sabine Fischer dafür bedanken, dass sie mir diese Gelegenheit bot. Sie war mir eine ausgezeichnete Mentorin und hat die Messlatte für zukünftige Vorgesetzte und auch mich selbst sehr hoch gelegt. Ich finde es bezeichnend, dass ich aus Besprechungen mit ihr immer sortiert, zuversichtlich und ermutigt herausging, selbst wenn mir davor auch mal anders zumute war. Ein besonderer Dank gilt auch Professor Andreas Hocke für das nachhaltige Interesse an meiner Arbeit. Ich schätze es sehr, dass er sich viele Male die Zeit nahm, um sich mit uns auszutauschen und mir wertvolles Feedback zu geben. Ebenso schätze ich die Bereitschaft von Professor Christian Stigloher, mein Projekt mitzubetreuen und diese Arbeit zu begutachten. Eine große Stütze für dieses Projekt war die finanzielle Unterstützung des Universitätsbund Würzburg und der European Molecular Biology Organization (EMBO). Mein Dank gilt Professor Oscar Camara Rey und seiner gesamten Arbeitsgruppe, insbesondere Dr. Andy Luis Olivares Miyares, für ihre herzliche Gastfreundschaft, geteilte Expertise und fortwährende Unterstützung. Ebenso danke ich Professor Sebastian von Mammen, Professor Keram Pfeiffer, Andreas Knote und Alexander Mück für die Zusammenarbeit an der Simulationssoftware *Alvin*, die mein Projekt entscheidend voranbrachte. Ich bedanke mich bei Professor Wolfgang Kübler und Professor Matthias Ochs für ihr Interesse und ihren wertvollen Input. Weiterer Dank gilt meinen lieben Kollegen am CCTB in Würzburg, besonders Simon und Andreas, die die gesamte Strecke mit mir gegangen sind. Ich hätte mir keine besseren Doktorbrüder wünschen können! Auch außerhalb des Instituts haben mich wichtige Personen durch diese Zeit begleitet. Michi hat eine Freude am Leben und an der Wissenschaft, die ansteckend ist. Lisa ist wahrscheinlich die coolste Person, die ich kenne. Wegstrecken sind einfach leichter und schöner, wenn sie sie mit mir geht. Nadine zeigt immer wieder ihre wundervolle Art, für mich da zu sein, indem sie mich mit Care-Paketen und gemeinsamen Unternehmungen überrascht. Drei absolute Powerfrauen, für deren Freundschaft ich unendlich dankbar bin. Zu guter Letzt möchte ich meiner ganzen Familie für ihren Zuspruch und ihre Unterstützung danken, die mir die nötige Stärke gaben, diese Herausforderung zu meistern. Liebe Rike, du bist meine große Schwester durch und durch und es ist mir eine Freude zu dir aufzusehen. Zu spüren, dass du auch stolz auf mich bist, macht mich wirklich glücklich. Mama und Papa, ich kann es nicht oft genug sagen: Euch verdanke ich alles.

Kurzfassung

Die Lunge erfüllt durch den Austausch von Atemgasen eine überlebenswichtige Aufgabe. Der Gasaustausch erfolgt durch einen einfachen, aber entscheidenden passiven Diffusionsprozess. Dieser findet in den Alveolen statt, ballonartigen Strukturen, die an die peripheren Atemwege grenzen. Alveolen sind von einem dichten Netz aus kleinen Kapillaren umgeben. Hier kommt die eingeatmete Luft in unmittelbare Nähe zu dem vom Herzen kommenden sauerstoffarmen Blut und ermöglicht den Austausch von Sauerstoff und Kohlenstoffdioxid über deren Konzentrationsgradienten.

Die Effizienz des Gasaustauschs kann anhand von Indikatoren wie der Sauerstoffdiffusionskapazität der Lunge und der Reaktionshalbzeit gemessen werden. Beim Menschen besteht eine beträchtliche Diskrepanz zwischen physiologischen Schätzungen der Diffusionskapazität und der theoretischen Maximalkapazität unter optimalen strukturellen Bedingungen (der morphologischen Schätzung). Diese Diskrepanz wird durch eine Reihe ineinandergreifender Faktoren beeinflusst, darunter strukturelle Elemente wie die Oberfläche und die Dicke der Diffusionsbarriere sowie physiologische Faktoren wie die Blutflussdynamik. Um die verschiedenen Rollen dieser Faktoren zu entschlüsseln, untersuchten wir, wie die morphologischen und physiologischen Eigenschaften der menschlichen alveolären Mikroumgebung kollektiv und individuell den Prozess des Gasaustauschs beeinflussen. Zu diesem Zweck entwickelten wir einen integrativen *in silico* Ansatz, der 3D morphologische Modellierung und Simulation von Blutfluss und Sauerstofftransport kombiniert.

Im Mittelpunkt unseres Ansatzes steht die Simulationssoftware *Alvin*, die als interaktive Plattform für das zugrundeliegende mathematische Modell des Sauerstofftransports in der Alveole dient. Unser räumlich-zeitliches Modell wurde durch die Integration und Erweiterung bestehender mathematischer Modelle entwickelt und liefert Ergebnisse, die mit experimentellen Daten im Einklang stehen. *Alvin* ermöglicht eine immersive Auseinandersetzung mit dem simulierten Gasaustausch, indem sie Parameteränderungen in Echtzeit und die Ausführung mehrerer Simulationsinstanzen gleichzeitig ermöglicht während sie ein detailliertes quantitatives Feedback liefert. Die beteiligten morphologischen und physiologischen Parameter wurden mit einem Fokus auf der Mikrovaskulatur weiter untersucht. Durch die Zusammenstellung stereologischer Daten aus der Literatur und geometrischer 3D-Modellierung erstellten wir ein "sheet-flow" Modell als realistische Darstellung des

menschlichen alveolären Kapillarnetzwerks. Blutfluss wurde mit Hilfe numerischer Strömungsdynamik simuliert. Unsere Ergebnisse stimmen mit früheren Schätzungen überein und unterstreichen die entscheidende Rolle von Viskositätsmodellen bei der Vorhersage des Druckabfalls in der Mikrovaskulatur. Darüber hinaus zeigten wir, wie unser Ansatz genutzt werden kann, um strukturelle Details wie die Konnektivität des alveolären Kapillarnetzes mit dem Gefäßbaum anhand von Blutflussindizes zu untersuchen. Es ist wichtig zu betonen, dass wir uns bislang auf verschiedene Datenquellen stützten und dass für weitere Fortschritte eine experimentelle Vailidierung erforderlich ist.
Die Integration unserer Ergebnisse in *Alvin* ermöglichte die Quantifizierung des simulierten Gasaustauschprozesses über die Sauerstoffdiffusionskapazität und die Reaktionshalbzeit. Neben der Bewertung der kollektiven Einflüsse der morphologischen und physiologischen Eigenschaften erleichterte unsere interaktive Software auch die Bewertung einzelner Parameteränderungen. Die Betrachtung des Blutvolumens und der für den Gasaustausch zur Verfügung stehenden Oberfläche ergab lineare Korrelationen mit der Diffusionskapazität. Die Blutflussgeschwindigkeit hatte einen positiven, nichtlinearen Effekt auf die Diffusionskapazität. Die Reaktionshalbzeit bestätigte, dass der Gasaustauschprozess in der Regel nicht diffusionslimitiert ist. Insgesamt lieferte unser Alveolenmodell einen Wert für die Diffusionskapazität, der in der Mitte der früheren physiologischen und morphologischen Schätzung lag. Daraus lässt sich schließen, dass Phänomene auf Alveolarebene zu 50% der Limitierung der Diffusionskapazität beitragen, die *in vivo* eintreten.
Zusammenfassend lässt sich sagen, dass unser integrativer *in silico* Ansatz verschiedene strukturelle und funktionelle Einflüsse auf den alveolären Gasaustausch aufschlüsselt und damit die traditionelle Forschung in der Atemwegsforschung ergänzt. Zusätzlich zeigen wir seinen Nutzen in der Lehre oder bei der Interpretation veröffentlichter Daten auf. Um unser Verständnis zu verbessern, sollten künftige Arbeiten vorrangig darauf ausgerichtet sein, einen zusammenhängenden experimentellen Datensatz zu erhalten und ein geeignetes Viskositätsmodell für Blutflusssimulationen zu finden.

Abstract

The lung plays a vital role by exchanging respiratory gases. At the core of this gas exchange is a simple yet crucial passive diffusion process occurring within the alveoli. These balloon-like structures, connected to the peripheral airways, are surrounded by a dense network of small capillaries. Here, inhaled air comes into close proximity with deoxygenated blood coming from the heart, enabling the exchange of oxygen and carbon dioxide across their concentration gradients.

The efficiency of gas exchange can be measured through indicators such as the diffusion capacity of the lung for oxygen and the reaction half-time. A notable discrepancy exists in humans between physiological estimates of diffusion capacity and the theoretical maximum capacity under optimal structural conditions (morphological estimate). This discrepancy is influenced by a range of interrelated factors, including structural elements like the surface area and thickness of the diffusion barrier, as well as physiological factors such as blood flow dynamics. To unravel the different roles of these factors, we investigated how morphological and physiological properties of the human alveolar micro-environment collectively and individually influence the process of gas exchange. To this end, we developed an integrative *in silico* approach combining 3D morphological modeling and simulation of blood flow and of oxygen transport.

At the core of our approach lies the simulation software *Alvin*, serving as an interactive platform for the underlying mathematical model of oxygen transport within the alveolus. Developed by integrating and expanding existing mathematical models, our spatio-temporal model produces results in agreement with experimental data. *Alvin* allows for real-time parameter adjustments and the execution of multiple simultaneous simulation instances and provides detailed quantitative feedback, offering an immersive exploration of the simulated gas exchange process. The morphological and physiological parameters at play were further investigated with a focus on the microvasculature. By compiling a stereological database from the literature and 3D geometric modeling, we created a sheet-flow model as a realistic representation of the morphology of the human alveolar capillary network. Blood flow was simulated using computational fluid dynamics. Our findings were in line with previous estimations and highlighted the crucial role of viscosity models in predicting pressure drop across the microvasculature. Furthermore, we showcased how our approach can be

harnessed to explore structural details, such as the connectivity of the alveolar capillary network with the vascular tree, using blood flow indices. It is important to emphasize that so far we have relied on different data sources and that experimental validation is needed to move forward.

Integration of our findings into *Alvin* allowed quantification of the simulated gas exchange process through the diffusion capacity for oxygen and reaction half-time. In addition to evaluating the collective influences of the morphological and physiological properties, our interactive software facilitates the assessment of individual parameter value changes. Exploring blood volume and surface area available for gas exchange revealed linear correlations with diffusion capacity. The blood flow velocity had a positive, non-linear effect on diffusion capacity. The reaction half-time confirmed that under normal conditions, the gas exchange process is not diffusion-limited. Collectively, our alveolar model yielded a diffusion capacity value that fell in the middle of previous physiological and morphological estimates, implying that alveolar-level phenomena contribute to 50% of the diffusion capacity limitations that occur *in vivo*.

In summary, our integrative *in silico* approach disentangles various structural and functional influences on alveolar gas exchange, complementing traditional investigations in respiratory research. We further showcase its utility in teaching and the interpretation of published data. To advance our understanding, future work should prioritize obtaining a cohesive experimental data set and identifying an appropriate viscosity model for blood flow simulations.

Contents

Chapter 1

Introduction

The lung is the central organ of the respiratory system and it performs an essential task: gas exchange. It enables the body to take up oxygen and release carbon dioxide, thereby maintaining vital metabolic processes. This intricate process relies on the passive diffusion of respiratory gases. As described by Fick's law (Fick, 1855), the rate of diffusion depends not only on the concentration gradient but also on structural parameters: the surface area and thickness of the diffusion barrier.

Alveoli, saccular structures opening into the peripheral airways, are the key to gas exchange (Figure 1.1). Their epithelium is extremely thin and collectively constitutes the majority of the lung's surface area (Gehr et al., 1978; Hsia et al., 2016). The alveolar wall is interwoven by a very dense network of small capillaries (Mühlfeld et al., 2010). In some regions, only a barrier thinner than a micrometer, consisting of the alveolar epithelium, the capillary endothelium and a shared basement membrane, separates the alveolar air space from the capillary blood (Gehr et al., 1978; Weibel et al., 1993). In addition to these morphological conditions, the efficiency of gas exchange is also influenced by physiological parameters. In the blood, oxygen binds to hemoglobin in the erythrocytes, a reaction that is influenced not only by the concentration of respiratory gases in the blood but also by factors such as temperature and pH value (Dash and Bassingthwaighte, 2010). The blood volume and the amount of erythrocytes determine how much oxygen can be transported. The flow velocity determines capillary transit time and thus the period available for the diffusion process. If there is an increased demand, for example during exercise, the oxygen uptake can be drastically enhanced by increasing the cardiac output (West, 2012).

One key indicator of the lung's ability to transport oxygen from inhaled air into the bloodstream is the pulmonary diffusing capacity for oxygen (DLO_2). DLO_2 quantifies the rate of oxygen consumption $\dot{V}\mathrm{O}_2$ in liters per minute (l/min) relative to the average oxygen partial pressure gradient between air and blood, ΔpO_2 (Lindstedt, 1984):

$$\mathrm{D}_{\mathrm{L}_{\mathrm{O}_2}} = \frac{\dot{V}\mathrm{O}_2}{\Delta \mathrm{pO}_2} \tag{1.1}$$

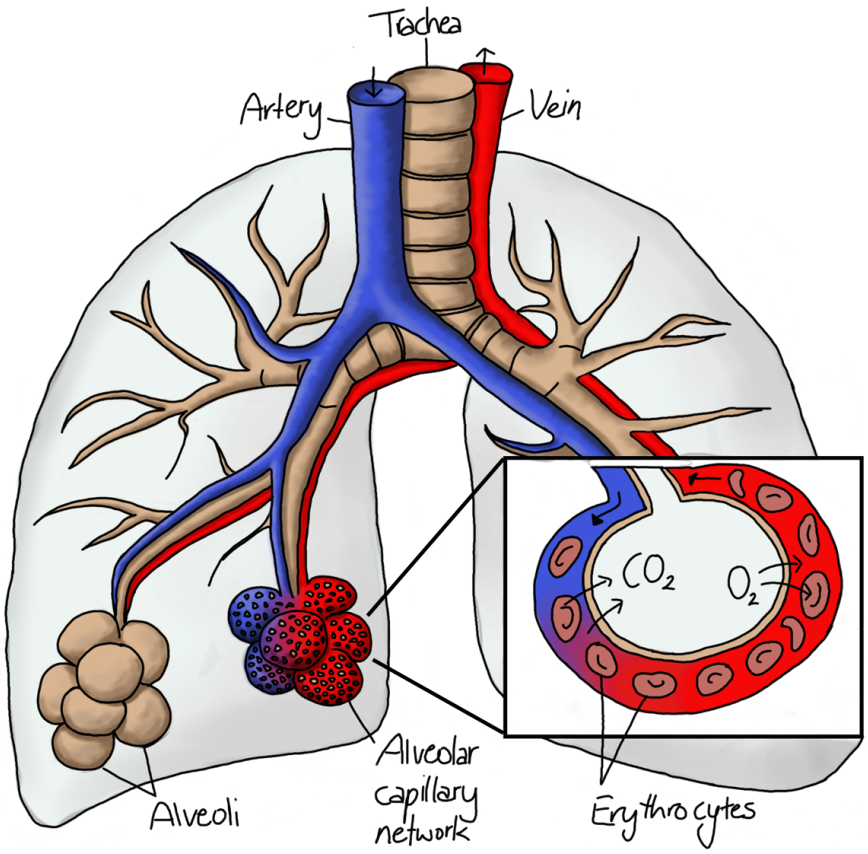

Figure 1.1: Schematic representation of the lung with its alveoli. The alveoli are connected to the peripheral airways. They are surrounded by a dense capillary network and have a remarkably thin epithelium. As a result, the inhaled air comes in close proximity to the blood and gas exchange takes place.

Physiological and morphological estimates of diffusion capacity differ considerably. While the physiological estimate of 30 ml/(mmHg·min) (Hsia et al., 2016) corresponds to the net oxygen consumption at rest, the morphological estimate of 158 ml/(mmHg·min) (Weibel, 2009) describes the maximum capacity under optimal structural conditions. The discrepancy between the two values signifies that the maximal capacity is not being exploited *in vivo*. In addition to the above-mentioned morphological and physiological factors at the alveolar level, these limitations can also be related to higher-level phenomena like the ratio of perfusion to ventilation or to non-pulmonary factors associated with the cardiovascular or skeletal muscle system (Hsia, 2002).

The experimental investigation of the factors that influence the efficiency of gas exchange at the alveolar level represents a major challenge: On the one hand, the tissue is subject to major volume changes and deformations during a breathing cycle. Secondly, the dimensions of the alveolus with a diameter of approximately 200 µm (Hansen and Ampaya, 1975;

Mercer et al., 1994) are below the resolution of current non-invasive characterization and imaging techniques. Consequently, we rely on fixation of the tissue. Depending on the fixation method, however, different biases and information losses must be accepted (Tuğcu et al., 2013; Braber et al., 2010; Hausmann et al., 2004; Javed et al., 1994; Mooi and Wagenvoort, 1983). As a result, although tissue structure and function are closely intertwined, experimental studies are typically not integrating both.

Whenever experimental methods reach their limits in the elucidation of a system, theoretical models emerge. With regard to gas exchange, this involved mathematical formulations for fundamental processes such as the diffusion of oxygen across the tissue barrier (Weibel et al., 1993) or the binding of oxygen to hemoglobin in erythrocytes (Dash et al., 2016). Beyond this, *in silico* models of alveoli have been developed to study gas exchange, taking into account structural and functional influences. These models vary in focus, with some emphasizing oxygen transport in either the air (Hofemeier et al., 2016) or blood space (Zurita and Hurtado, 2022), representing the other compartment and the diffusion barrier as boundary conditions. More holistic approaches have employed simplified, single-compartment models to simulate oxygen diffusion and transport in both air and blood spaces (Ben-Tal, 2006). Remarkably generic, these models can represent different systems, from the entire lung to specific components like an acinus (a whole branch of the airway tree in the respiratory zone) or individual alveoli, depending on the chosen boundary conditions. In a more recent and sophisticated approach, the distribution of oxygen transport in the air, across the tissue barrier and with the blood has been studied taking into account the respiratory dynamics in the alveolus (Si and Xi, 2022). While holding great potential, this work has primarily focused on the physiological processes that govern gas exchange in the alveolus. The tissue structure has been simplified due to the limited computing capacity.

Our objective was to build on this previous work and complement it by developing an integrative *in silico* model of the alveolus that takes into account both morphological and physiological details.

Objective

This thesis addresses the question of how morphological and physiological characteristics collectively and individually influence the process of gas exchange in the human alveolar micro-environment. We investigated this topic with a particular focus on the alveolar capillary network. From Fick's law of diffusion we know that the capillary surface area influences the diffusion rate of the respiratory gases. We also know that the capillary and blood volume determines the capacity to transport gases and that the blood flow velocity sets the time available for the diffusion process. We set out to simulate the interplay between these factors and quantify their influence on gas exchange using key indicators such as the DLO_2

and reaction half-time. This implied the integration of morphological and physiological data. At the heart of the project is the interactive application *Alvin*, which simulates the gas exchange process based on a time-resolved mathematical model (Figure 1.2). In *Alvin*, the simulation results are displayed both visually in the form of a 3D model and quantitatively in the form of dynamic graphs. The model parameters can be configured by the user, the default settings are based on reference values from the literature. It is possible to run several simulation instances simultaneously and compare their results. We present how *Alvin* can be applied in teaching or to interpret and review published data. *Alvin* and its application use cases were published in Schmid et al. (2022). In *Alvin*, the parameters can be configured individually and independently of each other. In reality, however, there are interdependencies between them. This also applies to the factors that are the focus of our interest: the morphology of the capillary network and the dynamics of blood flow. To further investigate these relationships, anatomically realistic models of the alveolar capillary network were created in the next part of this study based on morphometric data from the literature. To predict the dynamics of blood flow in this capillary geometry, we used computational fluid dynamics simulations. This method provides an in-depth understanding of the flow paths and the distribution of flow velocity and static pressure in the model. By introducing variation in morphology, we can quantify its influence on indices such as mean flow velocity within capillaries and arteriole-to-venule pressure drop. Conversely, we demonstrate how this approach can be used to infer structural details from blood flow parameters. Finally, the findings from data-based 3D modelling and blood flow simulation are integrated into *Alvin* to investigate their influence on DLO_2 and reaction half-time.

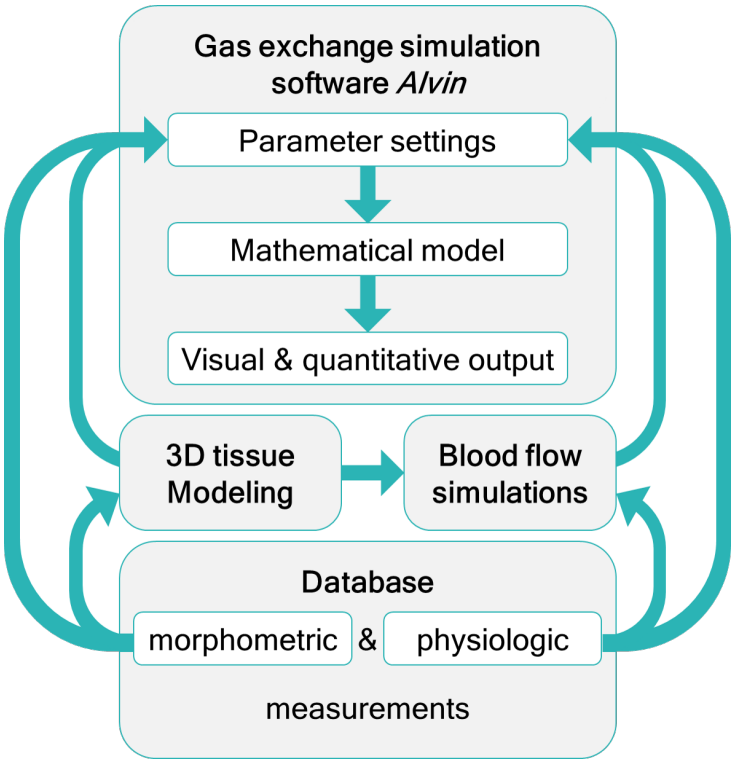

Figure 1.2: The software *Alvin* serves as an interactive platform for simulating gas exchange in the human alveolus. The user may configure the model parameters and results are displayed both visually and quantitatively. A database of morphometric and physiologic measurements forms the basis for the default parameter settings in *Alvin*, for the 3D tissue modeling and for the choice of boundary conditions for the blood flow simulations. The results of the latter two are in turn incorporated into the parameter settings of *Alvin*.

Chapter 2

Methods

Methodologically, the study can be divided into three main parts. In the first and overarching part, the simulation software *Alvin* was developed. *Alvin* and its underlying mathematical model were implemented in Unity, a game engine for creating interactive real-time content (`https://unity.com/`). The second part of the study involved *in silico* modeling of the alveolar tissue, with a specific focus on the alveolar capillary network. We conducted this work in the open-source 3D creation suite Blender® (`https://www.blender.org/`, which provides powerful tools for 3D modelling. Lastly, we performed blood flow simulations in Ansys® Fluent®, a leading commercial CFD software (`https://www.ansys.com/products/fluids/ansys-fluent`). It is worth noting that the coupling between 3D modeling and CFD simulation required several intermediate steps and the use of additional software tools. Cross-software data analysis and plotting of results was performed using the Python programming language v3.11.5 (`https://www.python.org/`). ChatGPT was used to revise the text for this thesis.

2.1 Simulation software *Alvin*

The development of the *Alvin* application was an interdisciplinary project carried out by a team of developers and supervising experts in games engineering, mathematical modeling and physiological education. The design of this software commenced with a requirements analysis, which encompassed the identification of target user groups and the crucial functionalities envisioned for this application. Our primary target group were scientists. *Alvin* was intended to convey the state of the art in gas exchange modeling to peers in the research domain, as well as to undergraduate students as part of their education. The primary aim of *Alvin* was not solely to present finalized simulation outcomes, but also to facilitate dynamic interactions with model parameters during simulations. This, in turn, allows for exploration of the model and testing of new hypotheses.

2.1.1 Requirements analysis

Based on our goals, a catalogue of requirements was developed in a user-centered engineering approach. This involved the formulation of requirement concepts based on the anticipated needs of the target users. In an iterative process, these concepts were reviewed by the supervising experts. Concepts were either approved or returned for further refinement. Later, following the same principle, prototypes of the application were tested by the supervising experts and volunteers. The feedback was actively incorporated into the design and engineering process. The final requirements were divided into three categories based on whether they pertain to Scientific (S), Educational (E), or Accessibility (A) aspects.

Scientific Requirements

- S.1 Gas exchange model suitable for interactive configuration.
  - S.1.1 Model parameters as public variables.
- S.2 Interfaces for interaction.
  - S.2.1 UI that allows configuration of model parameters and a simulation that responds directly to these configurations.
  - S.2.2 The application should allow comparisons of simulations with different model configurations.
  - S.2.3 Possibility to reset the simulation.
- S.3 Quantitative simulation output.
  - S.3.1 Quantitative results in the form of graphs and key conclusion values.
    - S.3.1.1 Dynamic plots that provide immediate feedback to model configurations by the user.
    - S.3.1.2 Readouts that allow comparison with experimental data (for model validation and application in research): DMO_2, DLO_2, reaction half-time.
  - S.3.2 Possibility to follow the simulation time.
- S.4 Visual feedback that emphasizes the connection between structure and function of the alveolus.
  - S.4.1 Zoomed-in system visualization: realistic, three-dimensional model of an alveolus.
  - S.4.2 Illustration of both model configurations (starting partial pressures of O_2/CO_2, blood volume and -flow velocity, thickness of tissue barrier) and simulation output (partial pressures of O_2, erythrocyte O_2 saturation) on the 3D model.
  - S.4.3 Emphasis on the connection between parameter configurations and output.

Educational Requirements

- E.1 Presentation of educationally relevant respiratory phenomena.
  - E.1.1 Consideration of both healthy and common disease conditions (pneumonia, ARDS, COPD, pulmonary fibrosis, pulmonary embolism) and means of comparison.
  - E.1.2 Consideration of the Bohr / Haldane effect.
    - E.1.2.1 The model parameters to be configured must include those that are decisive for the Bohr effect.
    - E.1.2.2 Oxygen binding curve as an additional quantitative output.
- E.2 Facilitate autonomous work with the application.
  - E.2.1 Background information on model parameters, disease conditions and output in the form of explanatory text.
  - E.2.2 Helping the user understand how to relate the simulation to physiology.
    - E.2.2.1 Classification of the parameter configuration in relation to physiological value ranges.
    - E.2.2.2 Classification of the (quantitative) simulation output in relation to physiological value ranges.

Accessibility Requirements

- A.1 Compatibility with common devices (computers or tablets with windows, iOS or linux).
- A.2 Simple and clear GUI (to enhance the intuitive use of the system).
  - A.2.1 A GUI that juxtaposes model configuration and output (visual and quantitative) to provide an overview of the most important functionalities at first glance.
  - A.2.2 Well arranged design of parameter menu.
    - A.2.2.1 Model parameters sorted into meaningful groups.
    - A.2.2.2 Sliders (convenient) and input fields (explicit) for parameter configuration.
  - A.2.3 Detailed information on model parameters and output that appears only when needed (in the form of pop-up windows and tooltips) to avoid overloading the GUI.
- A.3 Applicability to the widest possible range of scientific issues.
  - A.3.1 Possibility to configure a wide range of parameter values.
  - A.3.2 Common gas units (mmHg and SI unit kPa).

2.1.2 An integrative, spatio-temporal model of oxygen transfer from alveolar air to hemoglobin in pulmonary capillary blood.

The core of the *Alvin* application is a mathematical model for gas exchange in the human alveolus. The process of oxygen uptake can be divided into two steps (Roughton and Forster, 1957): 1. The diffusion of O_2 from the air into the blood and the interior of erythrocytes, and 2. the binding of O_2 to hemoglobin. In accordance with these two steps, we structured our mathematical model into two sub models. To account for O_2 and CO_2 pressure gradients within the blood compartment, we discretized a representative capillary into equally sized sections (Figure 2.1). In a first step, the oxygen diffusion from the alveolar air is calculated for each capillary section successively. Let us consider blood entering the first section with a given pO_2. According to Fick's law, the oxygen flow ν across the barrier is a function of morphological parameters and the pressure gradient ΔpO_2 between air and blood (Weibel et al., 1993), such that

$$\nu = \mathrm{DMO_2} \cdot \Delta \mathrm{pO_2} = K_{O_2} \cdot \frac{s}{\tau} \cdot \Delta \mathrm{pO_2} \tag{2.1}$$

The membrane diffusing capacity for oxygen (DMO_2) is the ratio of surface area s to barrier thickness τ multiplied by the permeability coefficient K_{O_2}. The amount of oxygen that diffuses into this capillary segment results from ν and the residence time of the blood in this segment, the latter being dependent on the flow velocity. With this amount of oxygen, the pO_2 of the blood in the next capillary section is updated and a new cycle of calculation as described above is started.

The quantity of CO_2 diffusing out of the capillary and into the alveolus is governed by the respiratory exchange ratio, which is defined as the ratio of CO_2 produced to O_2 consumed. It is determined by analysis of exhaled air in comparison to ambient air and its average value for the human diet is approximately 0.82 (Sharma et al., 2020).

The part of our mathematical model that describes the binding of O_2 and CO_2 to hemoglobin was taken from Dash et al. (2016) and reads:

$$\mathrm{S_{HbO_2}} = \frac{(\mathrm{pO_2}/p50)^{nH}}{1 + (\mathrm{pO_2}/p50)^{nH}}. \tag{2.2}$$

This Hill function sets hemoglobin oxygen saturation (S_{HbO_2}) in relation to pO_2, the Hill coefficient nH and $p50$, the value of pO_2 at which hemoglobin is 50 % saturated with O_2. The Hill coefficient nH depends on pO_2, so that

$$nH = \alpha - \beta \cdot 10^{(-pO_2/\gamma)}, \tag{2.3}$$

where α, β and γ are parameters associated with the apparent cooperativity of O_2 and Hb. The values of these parameters were taken from Dash et al. (2016) and are listed in

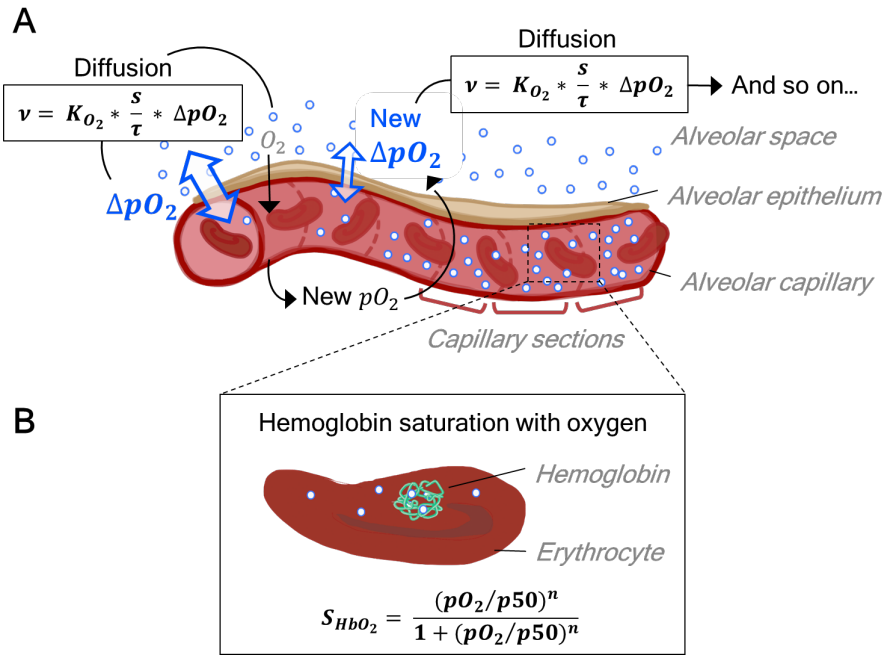

Figure 2.1: Schematic depiction of the model capillary with erythrocytes, isolated from the alveolar space by a single layer of alveolar epithelium. A) To reconstruct O_2 and CO_2 pressure gradients along the capillary, it is discretized into equally sized sections. The pressure gradient (ΔpO_2) between the alveolar space and blood, along with the resultant oxygen flow, is sequentially computed for each section. Subsequent sections are influenced by the oxygen flow of the preceding one, which impacts pO_2 and thus ΔpO_2. Oxygen diffusion, contingent on ΔpO_2, follows Fick's law (Weibel et al., 1993). B) Guided by the pO_2 and pCO_2 gradients across the capillary sections resulting from step 1, the hemoglobin oxygen saturation (S_{HbO_2}) is determined for each section. The corresponding Hill equation has been established and fitted to experimental data (Dash et al., 2016). Adapted from Schmid et al. (2022).

Table 2.2. The parameter $p50$ depends on blood pCO_2, blood temperature (T), erythrocyte pH (pH_{rbc}), and the concentration of the organic phosphate 2,3-bisphosphoglycerate ([2,3]-DPG). Dash et al. (2016) described these dependencies in polynomial expressions and fitted them to experimental data:

$$P_{50} = P_{50,D} \cdot \left(\frac{P_{50,\Delta pH}}{P_{50,D}}\right) \cdot \left(\frac{P_{50,\Delta CO2}}{P_{50,D}}\right) \cdot \left(\frac{P_{50,\Delta DPG}}{P_{50,D}}\right) \cdot \left(\frac{P_{50,\Delta T}}{P_{50,D}}\right) \tag{2.4}$$

$$P_{50,\Delta pH} = P_{50,D} - 25.535(pH - pH_D) + 10.646(pH - pH_D)^2 - 1.764(pH - pH_D)^3 \tag{2.4a}$$

$$P_{50,\Delta CO2} = P_{50,D} + 0.1273(pCO_2 - pCO_{2,D}) + 1.083 \cdot 10^{-4}(pCO_2 - pCO_{2,D})^2 \tag{2.4b}$$

$$P_{50,\Delta DPG} = P_{50,D} + 795.63([DPG] - [DPG]_D) - 19660.89([DPG] - [DPG]_D)^2 \tag{2.4c}$$

$$P_{50,\Delta T} = P_{50,D} + 1.435(T - T_D) + 4.163 \cdot 10^{-2}(T - T_D)^2 + 6.86 \cdot 10^{-4}(T - T_D)^3. \tag{2.4d}$$

The default values for all model parameters from Equation 2.4 and Equations 2.4a-2.4d, indicated with a 'D', were adopted from Dash et al. (2016) and are listed in Tables 2.1 and 2.2.
In our model, the S_{HbO_2} for each capillary section is calculated as a function of the pO_2 and pCO_2 values prevailing there, as determined in step 1.

2.1.3 Implementation

Alvin was implemented in Unity version 2020.1.16f1, using C# as the programming interface. A comprehensive description of the application and its functionalities in meeting the specified requirements is included in the Results Section 3.2. This section presents the model parameters, background information on the simulation output and two different prototypes.

Model parameters

The values of the morphological and physiological parameters used in the mathematical model were chosen according to the existing literature. In *Alvin*, most of these parameters can be configured by the user within a certain range of values (Table 2.1).
Other parameters are not configurable by the user and are not displayed on the user interface of the application (Table 2.2). They are part of the mathematical model in the background (permeability coefficient and capillary length) or are required for the presentation of simulation results in the form of dynamic graphs, as detailed in the next Section.

Simulation output

Parameter changes lead to a run-time update of the simulation and the simulation output. The "Oxygen Saturation along Capillary" plot directly presents the result of the mathematical model by plotting the saturation values along the capillary as a function of transit time. For the simulation output "Oxygen Uptake," further calculations need to be performed, taking into account several parameters (Table 2.2). The amount of oxygen taken up by the representative capillary is calculated from the number of RBCs reaching the end of the capillary and their oxygen saturation, assuming the number of hemoglobin molecules per RBC.

Parameter	**Unit**	**Default value**	**Reference**	**Value Range**
Alveolar pO_2	mmHg	100	Sharma et al. (2020)	1 - 150
Blood pO_2	mmHg	40	Dash et al. (2016)	1 - 150
Alveolar pCO_2	mmHg	40	Sharma et al. (2020)	1 - 150
Blood pCO_2	mmHg	45	Dash et al. (2016)	1 - 150
Surface area	μm^2	121000	Mercer et al. (1994)	0 - 210000
Thickness of tissue barrier	µm	1.11	Gehr et al. (1978); Weibel et al. (1993)	0.1 - 0.3
Blood flow velocity	mm/s	1	Abstracted from: Weibel et al. (1993); Petersson and Glenny (2014)	0.01 - 2
Blood volume	μm^3	410000* (50 % "capillary recruitment")	Abstracted from: Mühlfeld et al. (2010); Okada et al. (1992)	1 - 820000
Blood temperature	℃	37	Dash et al. (2016)	20 - 44
Erythrocyte pH (pH_{rbc})		7.24	Dash et al. (2016)	5.8 - 8.2
Concentration of [2,3]-DPG	mM	4.65	Dash et al. (2016)	1 - 10

Table 2.1: Configurable model parameters in *Alvin* and their default settings. Depending on these morphological and physiological parameters, the mathematical model in *Alvin* predicts the course of gas exchange in one alveolus. The default settings were chosen based on literature values and represent mean values corresponding to a single alveolus. In *Alvin*, these parameters can be configured within the specified value range. *Estimates for the entire lung were scaled down to a single alveolus, assuming a total number of 480 million alveoli in the human lung (Ochs et al., 2004).

Results are extrapolated to the entire alveolus via the number of capillaries per alveolus. Similarly, to calculate the diffusion capacity of the whole lung, the alveolar oxygen uptake is multiplied by the number of alveoli in the human lung. The "Oxygen Dissociation Curve" is calculated independently of the main simulation. Considering the model parameter configurations, the second sub-model (Equation 2.2) is used to predict Hb oxygen saturation for

Parameter	Unit	Value	Reference
Permeability coefficient K_{O_2}	$cm^2/(s \cdot mmHg)$	$5.5 \cdot 10^{-10}$	Weibel et al. (1993)
α		2.82	Dash et al. (2016)
β		1.2	Dash et al. (2016)
γ	mmHg	29.25	Dash et al. (2016)
p50 at default conditions $p50_D$	mmHg	26.8	Dash et al. (2016)
Capillary length	µm	500	Weibel et al. (1993)
Number of capillaries		52	Calculated from capillary volume, radius and length Mühlfeld et al. (2010); Weibel et al. (1993)
Number of Hb molecules per RBC		$270 \cdot 10^6$	Pierigè et al. (2008)
Number of alveoli in human lung		$480 \cdot 10^6$	Ochs et al. (2004)

Table 2.2: Constant model parameters in *Alvin* and their references.

a range of partial pressure values.

Prototypes

Two distinct prototypes of *Alvin* were developed to suit the different use cases detailed in this study. One prototype was tailored for educational purposes (Section 3.3.1), offering two levels of varying complexity. In the initial level, only a single simulation instance can be executed at any given time. Access to the more intricate second level, which unlocks the full complexity, is granted through an access code. The second prototype, designed for research purposes, has additional readouts. In particular, it provides data on the "membrane" diffusion capacity for oxygen (DMO_2) and the reaction half-time, which is crucial for model validation (as discussed in Section 3.1). In addition, this prototype includes the lung diffusion capacity for oxygen, DLO_2, in the simulation output.

2.2 3D *in silico* modeling of the human alveolus and alveolar capillary network

Three-dimensional models of the alveolus and the ACN were created in Blender® (`https://www.blender.org/`) version 2.82 (*Alvin* model) and 3.3 (refined models). A simplified model of the alveolar tissue, including the capillary bed, served as the basis for visualizing the simulated gas exchange process in *Alvin*. The 3D model's proportions were roughly aligned with literature references to represent tissue structure as realistically as possible. As the project progressed, the 3D modeling of the ACN was refined, and its alignment with morphometric literature values was monitored more rigorously. Two different concepts of the ACN geometry, the tube-flow and sheet-flow, were compared, employing different modeling strategies in Blender. To investigate the connection between the capillary network and the vascular tree, the sheet-flow ACN model was linked to different configurations of arterioles and venules.

2.2.1 3D visualization of the alveolus and alveolar capillary network for *Alvin*

The 3D model of the alveolus in *Alvin* was aimed to realistically represent tissue structure and facilitate the visualization of gas exchange. To this end, the sizes of the alveolus and the alveolar capillary network were based on literature values, as summarized in Table 2.3. The alveolus was modeled as a truncated sphere, with an opening, the 'alveolar mouth', forming the access to the airways. It comprises a single layer representing the tissue barrier, including connective tissue fibers, epithelial cells, and alveolar lining fluid. The capillary bed, a network of branching tubes, was modeled around this alveolus according to the tube-flow concept. The connection of the ACN to other capillaries and/or the vascular tree is illustrated by two representative connecting vessels. To facilitate the visualization of blood flow processes in *Alvin*, a path along the capillary network was cut open, providing a view into its interior.

2.2.2 Refined data-based model of the human alveolar capillary network

First, an alveolar base in the form of an open 3/4 spheroid was modeled as a scaffold for the ACN (Figure 2.2 A). For this, we drew on input parameters comprising the alveolar volume or diameter (Hansen and Ampaya, 1975; Mercer et al., 1994; Ochs et al., 2004), the diameter of the mouth (Hansen and Ampaya, 1975; Matsuda et al., 1987) as well as the number and diameter of pores of Kohn (Kawakami and Takizawa, 1987; Toshima et al.,

Parameter	Unit	Literature value	Reference	Blender model
Alveolar diameter	µm	225	(Mercer et al., 1994)	225
Alveolar volume	μm^3	$4.2 \cdot 10^6$	(Ochs et al., 2004)	$5.4 \cdot 10^6$
Alveolar surface area	μm^2	121000	(Mercer et al., 1994)	150000
Capillary volume	μm^3	820000*	(Mühlfeld et al., 2010)	787000
Capillary surface area	μm^2	540000*	(Mühlfeld et al., 2010)	335000
Capillary radius	µm	3.15	(Mühlfeld et al., 2010)	4.28
Capillary segment length	µm	5.92	(Mühlfeld et al., 2010)	8.62

Table 2.3: The 3D visualization of the alveolus and the alveolar capillary network in *Alvin* was created in Blender®, based on literature measurements. *Estimates for the entire lung were scaled down to a single alveolus, assuming a total number of 480 million alveoli in the human lung (Ochs et al., 2004).

2004). The resulting surface area, depth and volume or diameter of the alveolar base model were considered output parameters and evaluated by comparison with corresponding literature values (Hansen and Ampaya, 1975; Mercer et al., 1994; Ochs et al., 2004; Stone et al., 1992). All reference values and model measurements are detailed in the Results Section 3.4. Similarly, we applied a set of input parameters to model the ACN and utilized others as output parameters for evaluation purposes. We considered two distinct concepts of ACN geometry that have been proposed in the literature: the tube-flow (Mühlfeld et al., 2010) and the sheet-flow (Fung and Sobin, 1969). The differences between these geometric concepts are reflected in different input parameters for modeling (Figure 2.2 B). The tube-flow ACN is constructed based on the diameter and the length of capillary segments (Mühlfeld et al., 2010). For the sheet-flow ACN, the thickness of the sheet as well as the diameter of the pillars and their distance to another was taken into account. It is worth noting that for the sheet-flow input parameters, we only found reference data from feline models (Sobin et al., 1970). To accurately represent the morphology of the human ACN in the context of the sheet-flow concept, we made these assumptions: the thickness of the sheet corresponds to the capillary diameter, and the spacing between pillars matches the length of capillary segments. The diameter of the pillars was derived by assuming the ratio of pillar diameter to interpillar distance of about 0.5 observed in cats (Sobin et al., 1970). The output parameters assessed were ACN volume and surface area (Mühlfeld et al., 2010; Gehr et al., 1978). In addition, the surface area of the ACN in contact with the alveolar base was measured and interpreted as the surface area available for gas exchange. Again, reference

values and model measurements are provided in Results Section 3.4.

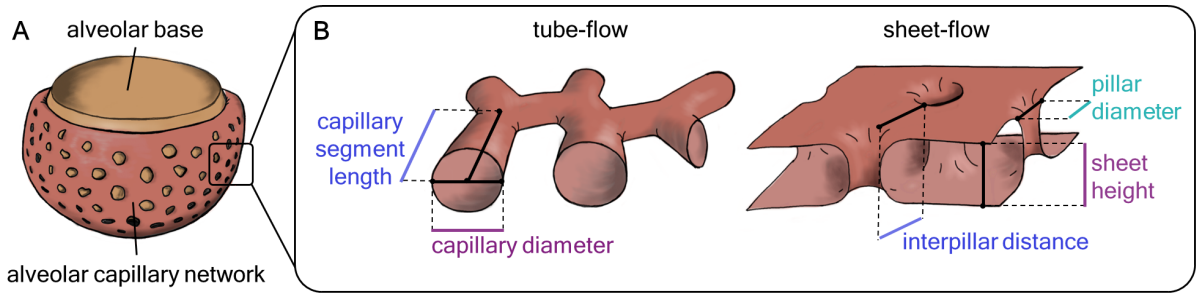

Figure 2.2: A) The alveolar base in the form of an open 3/4 sphere served as the basis for modeling the capillary network. B) Two distinct concepts of the capillary bed geometry, tube-flow and sheet-flow, were compared. The tube-flow capillary network is characterized by the length and diameter of its capillary segments. In contrast, the sheet-flow capillary bed is determined by the sheet's height, the diameter of the tissue pillars, and the spacing between them (interpillar distance).

2.2.3 Modeling strategies in Blender

In Blender, different modeling workflows were used to create the tube-flow and the sheet-flow geometries of the ACN (Figure 2.3). The initial step involved extending a surface around the alveolar base, which formed the basis for the subsequent construction of the ACN. We call this surface the capillary base surface. For the tube-flow model, this surface was positioned at a distance equal to the capillary radius from the alveolar base (Figure 2.3 AI). Drawing inspiration from published electron microscopy images of the ACN (Mühlfeld, 2021; Du et al., 2020; Buchacker et al., 2019), which predominantly displayed trivalent nodes between capillary segments, we opted for a topology featuring hexagonal and pentagonal faces for the capillary base surface. This choice resulted in trivalent vertices and was achieved using Blender's Tissue add-on's Dual Mesh algorithm. This algorithm transforms a triangular mesh into a polygonal mesh by subdividing the faces and subsequently dissolving the original vertices. The edges of these faces would later form the centerlines of the capillary tubes. The face centers would be replaced by voids which, depending on their diameter, represent capillary loops or interalveolar pores of Kohn. Subsequently, a voluminous body was formed from the capillary base. In the tube-flow model, this transformation was achieved using the Wireframe modifier, which systematically processed all faces and converted edges into quadrilateral polygons (Figure 2.3 AII). The thickness setting of the modifier controlled the width of these polygons and thus the later capillary diameter. Lastly, the capillary geometry was smoothed using two iterations of the Subdivision Surface modifier (Figure 2.3 AIII). For modeling the sheet-flow geometry, the capillary base surface was positioned directly at the alveolar base (Figure 2.3 BI). The positions for

tissue pillars were randomly distributed across this surface using a simple script, ensuring a specified average distance between them. The script enforced a minimum spacing of one and a half times the pillar diameter. Additionally, positions for the necessary number of pores of Kohn were allocated manually. These positions were then punctured on the capillary base surface with holes that matched the diameters of the tissue pillars and pores of Kohn, respectively. By extruding the capillary base surface away from the alveolar base by the desired sheet thickness, a voluminous body was obtained (Figure 2.3 BII). Again, two iterations of the Subdivision Surface modifier were applied to smooth the capillary geometry (Figure 2.3 BIII).

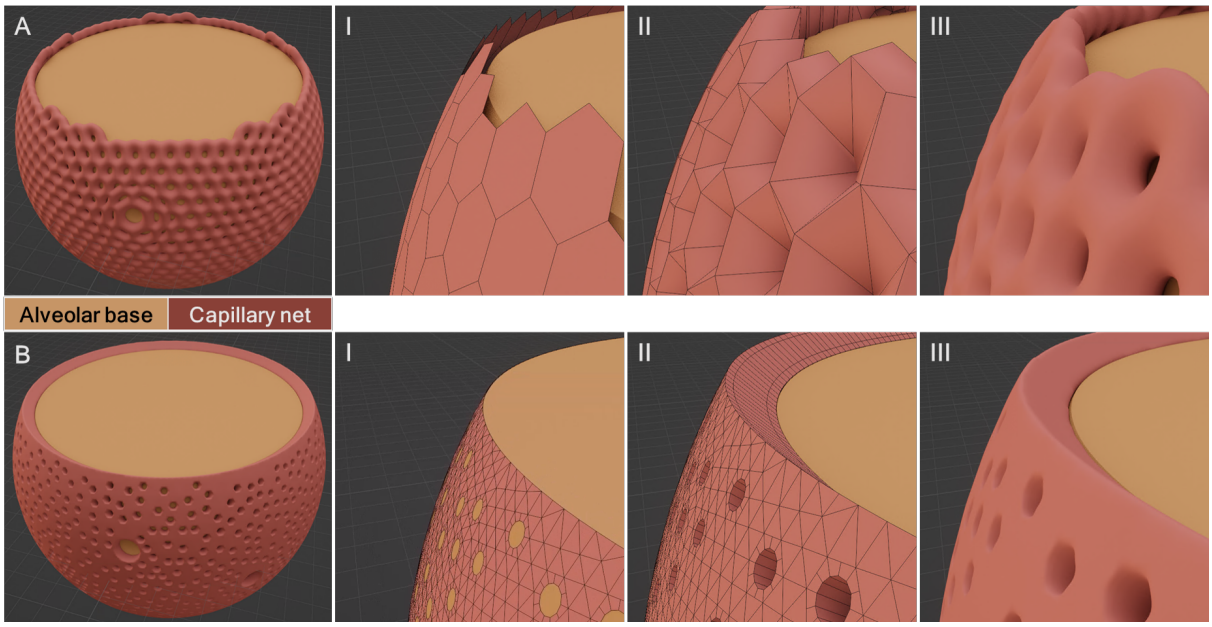

Figure 2.3: Tube-flow (A) and sheet-flow (B) models of the alveolar capillary network were modeled in Blender following different workflows. The first step (I) involved creating a base surface for the capillary network (red) around the alveolar base (brown). In second step (II) a voluminous body was formed from the capillary base surface. In a final step (III), the capillary geometry was smoothed using two iterations of the Subdivision Surface modifier.

2.2.4 Model geometries for connectivity analyses

Since the alveolar parenchyma including the capillary network resembles a sponge-like continuum, it is difficult to quantify the connection between the ACN and the arterial and venous vascular trees (Zhuang et al., 1985). To investigate this linkage, the 3D sheet-flow model was connected to a pair of cylindrical vessels facing each other (Figure 2.4). One arteriole and one venule, both with a diameter of 20 µm, were chosen as the default configuration. There are different specifications in the literature for the diameter of the pre-capillary

arterioles. This has led us to create further models with vessels of increasing diameter from 20 µm to 60 µm in steps of 10 µm. The ACN is a continuous structure associated to multiple arterioles and venules and extending across multiple alveoli (Mühlfeld, 2021). The delineation of a distinct perfusion unit that is supplied by one arteriole and drained by one venule is difficult. Therefore, to characterize the tissue structure, it is sensible to assess the ratio of arterioles and venules to alveoli. In addition, therefore, we included models with gradually increasing numbers of vessels from one to five. In so-called symmetrical model sets, these vessel configurations were applied to both arterioles and venules. Furthermore, asymmetric model sets comprised models with variations in only one of the vessel types (arterioles or venules), while the other vessel retained the standard configuration.

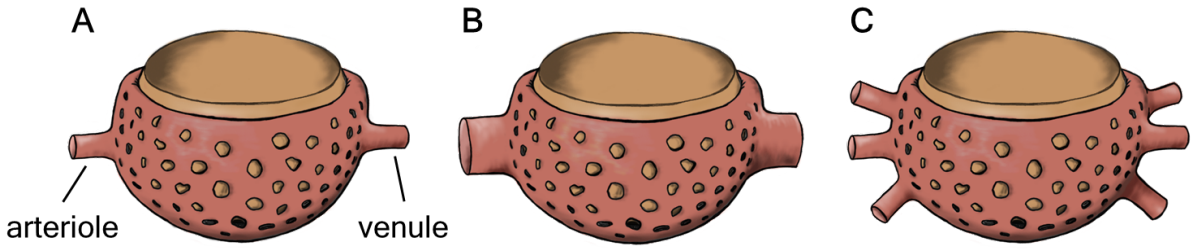

Figure 2.4: The capillary network was linked to arterioles and venules. The default configuration (A) involved one arteriole and one venule, each with a diameter of 20 µm. Further configurations were introduced by changing either the diameter (B) or the number (C) of these vessels.

2.3 Computational fluid dynamics

Computational Fluid Dynamics (CFD) served as a powerful tool in our study, enabling us to simulate blood flow dynamics within our 3D models of the ACN. Based on our model geometries, flow domains were defined and high-quality computational meshes were built. On these meshes, a physical model describing the flow was solved numerically. The quality of the solution was assessed systematically.

2.3.1 Introduction to CFD

CFD is based on the Navier-Stokes equations, a system of non-linear partial differential equations of second order that can fully describe the flow of a fluid (Ferziger et al., 2020; Versteeg and Malalasekera, 2007; ANSYS, 2009a). This system of equations can generally not be solved analytically. In order to solve them, discretization methods are employed and simplifying assumptions are introduced.

Conservation of mass and momentum

Fluid flow through a control volume is described by the conservation equations for mass (Equation 2.5) and momentum (Equation 2.7). Detailed derivations of these are available in established literature such as Bird et al. (2006) and Ferziger et al. (2020). In short, the conservation of mass, often referred to as the continuity equation, states that the rate of change of mass within the control volume is equal to the net mass flux across its boundaries. In differential form, this can be expressed with the divergence of the mass flux density vector ($\rho\vec{v}$), where ρ represents the fluid density, and $\vec{v}$ is the velocity vector:

$$\frac{\partial \rho}{\partial t} + \nabla \cdot (\rho \vec{v}) = 0. \tag{2.5}$$

For incompressible fluids, $\frac{\partial \rho}{\partial t}$ can be neglected. In the three-dimensional Cartesian form, the continuity equation then reads

$$\nabla \cdot (\rho \vec{v}) = \frac{\partial (\rho u)}{\partial x} + \frac{\partial (\rho v)}{\partial y} + \frac{\partial (\rho w)}{\partial z} = 0, \tag{2.6}$$

where u, v and w represent the Cartesian components of the velocity vector $\vec{v}$.
The momentum conservation equation is derived from Newton's second law of motion and states that the rate of change of momentum within the control volume is balanced by internal and external forces. In differential form, this principle can be expressed as:

$$\frac{\partial (\rho \vec{v})}{\partial t} + \nabla \cdot (\rho \vec{v} \otimes \vec{v}) = -\nabla p + \nabla \cdot \bar{\bar{\tau}} + \rho \vec{g}. \tag{2.7}$$

The term on the left hand side includes the rate of change of momentum and the convective acceleration. On the right hand side, the pressure gradient $-\nabla p$ and the divergence of the stress tensor $\nabla \cdot \bar{\bar{\tau}}$ represent the internal forces and friction within the fluid, while the gravitational body force $\rho \vec{g}$ represent external forces. The stress tensor is directly influenced by the fluid's viscosity. In three-dimensional Cartesian form, the conservation of momentum can be represented as follows:

$$\begin{aligned}
\frac{\partial (\rho u)}{\partial t} + \frac{\partial (\rho u u)}{\partial x} + \frac{\partial (\rho u v)}{\partial y} + \frac{\partial (\rho u w)}{\partial z} &= -\frac{\partial p}{\partial x} + \frac{\partial \tau_{xx}}{\partial x} + \frac{\partial \tau_{xy}}{\partial y} + \frac{\partial \tau_{xz}}{\partial z} + \rho g_x \\
\frac{\partial (\rho v)}{\partial t} + \frac{\partial (\rho v u)}{\partial x} + \frac{\partial (\rho v v)}{\partial y} + \frac{\partial (\rho v w)}{\partial z} &= -\frac{\partial p}{\partial y} + \frac{\partial \tau_{yx}}{\partial x} + \frac{\partial \tau_{yy}}{\partial y} + \frac{\partial \tau_{yz}}{\partial z} + \rho g_y \\
\frac{\partial (\rho w)}{\partial t} + \frac{\partial (\rho w u)}{\partial x} + \frac{\partial (\rho w v)}{\partial y} + \frac{\partial (\rho w w)}{\partial z} &= -\frac{\partial p}{\partial z} + \frac{\partial \tau_{zx}}{\partial x} + \frac{\partial \tau_{zy}}{\partial y} + \frac{\partial \tau_{zz}}{\partial z} + \rho g_z
\end{aligned} \tag{2.8}$$

Discretization and solution

Ansys Fluent uses the finite volume method (FVM) for discretization of the governing equations (ANSYS, 2009b). In FVM, the solution domain is divided into a finite number of non-overlapping control volumes (Ferziger et al., 2020). The conservation equations are then

integrated over each control volume to obtain a finite, or integral, form of the equations. The variable values are calculated at computational nodes in the centroid of each control volume. The variable values on the control volume surfaces are expressed by interpolation of the values at its computational node and those at computational nodes of neighboring control volumes. The results are algebraic equations for every control volume that can be solved numerically. When solving these equations, one is confronted with the following challenges (Versteeg and Malalasekera, 2007): These equations are intricately coupled as all velocity components contribute to each momentum equation (Equations 2.8) as well as the continuity equation (Equation 2.6). Additionally, the momentum equations involve non-linear terms due to the convective effects. The central challenge revolves around the role of pressure. While it appears in all momentum equations, there is no dedicated equation, such as a transport equation, to describe its behavior. To overcome this, an additional condition for the pressure is derived by reformatting the continuity equation (ANSYS, 2009b).
The system of equations is then solved using an iterative solver. There are pressure-based and density-based solvers. We employed a pressure-based coupled algorithm that operates as follows (ANSYS, 2009b; Versteeg and Malalasekera, 2007): Initially, using the momentum equations, the velocity and pressure fields for the flow domain are implicitly estimated. Subsequently, a correction is applied to ensure the fulfillment of the continuity equation. These two steps, velocity and pressure prediction followed by continuity correction, are iteratively performed until convergence of the velocity and pressure fields.

2.3.2 Finite volume meshes

As noted previously, CFD simulations require a mesh that discretely represents the geometric domain within which fluid flow is to be characterized. To this end, we have developed finite volume (FV) meshes for our 3D ACN models, encompassing the inlet (arteriole) and outlet (venule) vessels. These FV meshes consist of a surface mesh that delineates the geometry's walls, including both inlet and outlet surfaces, as well as a volumetric mesh that defines the interior (Figure 2.5). Ensuring an accurate simulation of fluid-wall interactions demands high-resolution mesh elements in close proximity to the boundary. Consequently, the volumetric mesh includes a high-resolution boundary layer of prism elements positioned near the wall, while the remaining volume is occupied by coarser polyhedral elements.

Preparation of finite volume meshes

Generating FV meshes from the 3D ACN models involved several steps. First, the Blender models had to be converted into a format suitable for finite volume meshing. To this end, the Blender models, consisting of around 2 million faces, were exported in STL (stereolithography) format. STL is a standard file format that represents 3D object surfaces us-

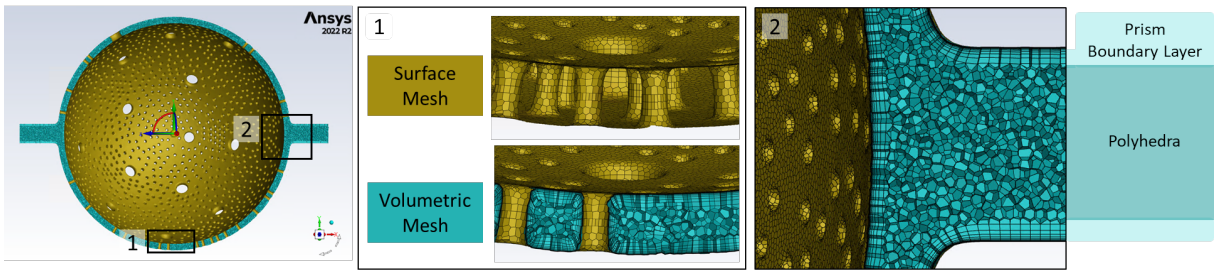

Figure 2.5: The finite volume mesh is divided into a surface mesh (gold) and a volume mesh (turquoise). The surface mesh delimits the geometry and represents the capillary wall and the inlet and outlet surfaces as defined in the Blender model. The volumetric mesh defines the interior of the geometry. It consists of a high-resolution boundary layer of prism elements near the walls and a coarser mesh of polyhedral elements in the centre of the volume.

ing a mesh of triangular faces. These STL files were then processed using Autodesk® Meshmixer™software version 3.5.474 (`https://meshmixer.com/`) to reduce the surface mesh complexity to around 500,000 triangles while maintaining the geometry's integrity. Subsequently, the STL files were converted into CAD (computer-aided design) files using FreeCAD version 0.20.1 (`https://www.freecad.org/`), an open-source software. The CAD format facilitated compatibility with Ansys' SpaceClaim modeling software. Within the SpaceClaim environment, the ACN geometry was organized into distinct zones, which included the inlet, wall, and outlet components necessary for CFD simulations.

Finally, the FV mesh was generated using Ansys Fluent Meshing software, employing a guided 'watertight geometry' workflow. This specific workflow is tailored for creating finite volume meshes from clean boundary meshes, ensuring that the geometries have no leaks or structural issues. The workflow starts by generating the surface mesh along the ACN wall and the inlet and outlet surfaces using a method called 'curvature size function'. This method governs the distribution of mesh sizes on a surface, guided by several user-defined parameters, including minimum and maximum values for the size of the mesh edges, a 'growth rate' determining the maximum size variation between neighboring mesh elements, and the curvature normal angle. The latter specifies the permissible surface curvature that a single mesh element can cover. The result of this method is a surface mesh that has a particularly high resolution in areas with strong curvature. Subsequently, the boundary layer of prism elements was generated, commencing from the surface mesh at the wall zone, utilizing the 'last ratio' meshing method. This technique governs the distribution of the prism layers based on the innermost layer, which serves as the transition to the polyhedral elements. The transition ratio, representing the ratio of height to length for individual elements in this transition layer, was specified. Moreover, the number of layers and the height of the initial layer (the layer nearest to the wall) were determined. The prism layers were arranged

in such a way that their height gradually increased from the wall toward the center of the volume. Lastly, the remaining volume was filled with polyhedral elements. The size function settings for this step, encompassing maximum element size and growth rate, mirrored those employed for the surface mesh. For each ACN model geometry, two FV meshes of distinct complexity were generated. The input parameters for the meshing workflow were scaled from the coarser mesh to the finer mesh by a factor of 1.6 (Table 2.4).

	Coarse mesh	**Fine mesh**
Surface mesh		
Minimum size (µm)	0.02	0.0125
Maximum size (µm)	2	1.25
Growth rate	1.2	1.2
Curvature normal angle (°)	9.6	6
Boundary layer		
Number of layers	6	10
Transition ratio	0.5	0.5
First height (µm)	0.02	0.0125
Volumetric mesh		
Growth rate	1.2	1.2
Max cell length (µm)	2	1.25

Table 2.4: Finite volume meshes for computational fluid dynamics were generated using the 'Watertight Geometry' workflow in Ansys Fluent Meshing. The surface mesh, the boundary layer mesh and the volumetric mesh were generated successively, taking into account a number of user-defined input parameters. The input parameters between the coarse and fine meshes differ by a refinement factor of 1.6.

Quality of finite volume meshes

Mesh quality significantly influences the accuracy and stability of numerical computations. The quality of our FV meshes was assessed using three different parameters (Table 2.5). The first parameter, inverse orthogonal quality (IOQ), is a measure of how closely each mesh element conforms to orthogonality with respect to its faces. IOQ values can vary between 0, signifying an ideal scenario where all element angles are 90°, and 1, indicating poor mesh quality. The IOQ of a mesh impacts its scalability, as well as the discretization error and iterative convergence of numerical solutions. Our meshing process required all elements to have an IOQ below a threshold of 0.95 to ensure high mesh quality. The mean IOQ of our meshes ranged from 0.16 to 0.19. The second parameter evaluated was size change, which reflects the volume ratio between adjacent elements. A low value close

to 1 is desirable to minimize errors in interpolation between control volumes. The mean size change in our meshes ranged from 3.8 to 3.9. The aspect ratio is a measure of how stretched a mesh element is. According to ANSYS (2009d), it is calculated as the ratio of the maximum value to the minimum value of any of the following distances: the distances between the element centroid and face centroids, and the distances between the element centroid and nodes.

Mesh size and quality	**Coarse mesh**	**Fine mesh**
Number of cells (10^6)	4.9	7.6
IOQ	0.17	0.2
Size change	3.88	3.92
Aspect ratio	18.0	26.4

Table 2.5: Quality of finite volume meshes was assessed using the parameters inverse orthogonal quality (IOQ), size change and aspect ratio. The specified values are the average of all mesh elements.

2.3.3 Model assumptions and simulation setup

The flow simulations were performed with the software Ansys® Academic Research CFD, release 2022 R2 (ANSYS, 2022). In Ansys Fluent Solution, different flow models and solvers can be used depending on the fluid's characteristics and the specific flow conditions. This includes whether the flow is assumed to be laminar or turbulent, compressible or incompressible and whether it is a Newtonian or non-Newtonian fluid. In this Section, the settings we have made in Ansys (Table 2.6) will be presented and justified.

Incompressible laminar flow

In laminar flow, fluid particles move in parallel, well-defined layers or streamlines, with minimal mixing or intermixing of adjacent layers (Ferziger et al., 2020; Ghaib, 2019). In contrast, fluid particles move in random directions and patterns in turbulent flows, leading to mixing and fluctuations in velocity. One can estimate whether a flow is laminar or turbulent using the dimensionless Reynolds number (Re) (Reynolds, 1883). For flow in a circular tube of diameter D, it is defined as follows:

$$Re = \frac{\rho U D}{\mu}, \tag{2.9}$$

where U is the average flow velocity and μ is the dynamic viscosity of the fluid. Re represents the ratio of convective to diffusive flow. If it exceeds a certain threshold value, the

General	
solver type	pressure-based
time	steady
viscous model	laminar
Material Settings	
type	fluid
density	1050 kg/m^3
viscosity, Newtonian fluid	0.002 kg/(m·s)
viscosity, non-Newtonian fluid	Carreau model (Equation 2.10)
Boundary Conditions	
inlet	velocity magnitude 0.0023 m/s
wall	stationary, no-slip
outlet	gauge pressure 1127 Pa
Solution Methods	
pressure-velocity coupling - scheme	coupled
spatial discretization - gradient	Green-Gauss node based
spatial discretization - pressure	second order
spatial discretization - momentum	second order upwind

Table 2.6: Parameter settings for the computational fluid dynamics simulations in the Ansys® Fluent Solution software. Fluid viscosity was either set constant or expressed by the non-Newtonian Carreau model.

probability that the flow is turbulent is high. A commonly applied rule of thumb suggests that the transition from laminar to turbulent flow typically occurs at a Reynolds number of approximately 2300 (Rotta, 1956). With a capillary diameter of 6.3 µm and our settings for fluid properties and boundary conditions (Table 2.6), Re is 0.0076. Hence, we opted for a laminar flow model.

The choice between modeling a flow as compressible or incompressible depends on the magnitude of density variations in the flow. If the density of the fluid remains nearly constant throughout the flow field, incompressible flow assumptions are adequate and simplify computational modeling. In CFD studies, it is common practice (Albors et al., 2023; Sousa et al., 2012; Figueroa et al., 2006) to approximate blood flow as an incompressible flow. Accordingly, we chose a constant density of 1050 kg/m^3 (Pries et al., 1996) and a pressure-based solver.

Newtonian and non-Newtonian viscosity models

The classification of a fluid as Newtonian or non-Newtonian depends on the behavior of its viscosity (Oertel et al., 2015). A Newtonian fluid exhibits a linear relationship between shear stress and shear rate, thus maintaining a constant viscosity regardless of applied stress or shear rate. In contrast, a non-Newtonian fluid does not have a constant viscosity. The latter changes with the applied shear rate or shear stress, resulting in a non-linear relationship between shear stress and shear rate. In our simulations, we considered both fluid types: the first being a Newtonian fluid with a constant viscosity of 0.002 kg/(m·s), and the second, a non-Newtonian fluid characterized by the Carreau viscosity model (Carreau, 1972). In this model, the apparent viscosity η is expressed as a function of shear rate γ as follows:

$$\eta = \eta_\infty + (\eta_0 - \eta_\infty)[1 + \gamma^2\lambda^2]^{(n-1)/2}, \tag{2.10}$$

where η_0 = 0.056 kg/(m·s) and η_∞ = 0.0035 kg/(m·s) represent the upper and lower limiting values of fluid viscosity, respectively, λ = 1.902 s is a time constant and n = 0.3568 the power-law index. The parameter values were adopted from Albors et al. (2023) and represent blood conditions (Figure 2.6).

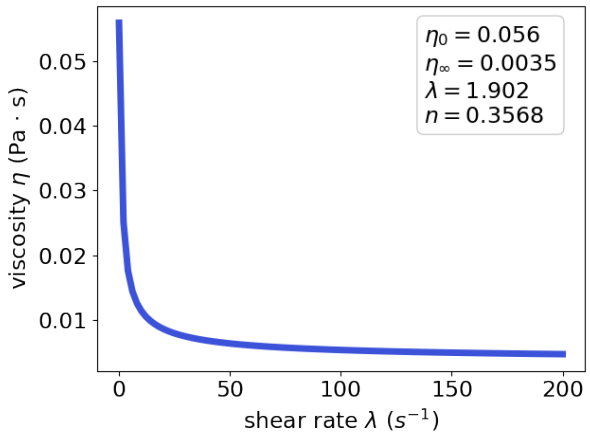

Figure 2.6: The Carreau model for non-Newtonian behaviour expresses the apparent viscosity as a function of shear rate. Model parameters include η_0 and η_∞, the upper and lower limiting values of fluid viscosity, respectively, the time constat λ and the power-law index n. We used parameter values suitable for blood conditions as suggested by Albors et al. (2023).

Boundary conditions

Boundary conditions are a critical component of any CFD analysis, as they provide the necessary context for the simulated flow within its surroundings. The boundary conditions specified in our study were a velocity at the inlet and a pressure at the outlet. The inlet

velocity was 0.0023 m/s, based on a value measured in the bullfrog (2.3 mm/s (Horimoto et al., 1979)). The outlet pressure was set to 1127 Pa, corresponding to the measured pressure in feline venules (11.5 cmH_2O (Nagasaka et al., 1984)). A no-slip boundary condition was applied at the walls, which were assumed to be rigid.

Discretization scheme

When discretizing the governing equations using the finite volume method, face values are interpolated from the centroid of the control volume using the second-order upwind scheme (ANSYS, 2009b). Gradients were derived using the Green-Gauss node-based gradient evaluation.

Simulation output

The solution was recorded on surfaces placed in parallel at several locations in the 3D model: At the inlet, in the capillary network near the junction with the arteriole(s), in the center of the capillary network, in the capillary network near the junction with the venule(s) and at the outlet. We focused on two target values: the flow velocity within capillaries and the pressure drop from arteriole to venule. To this end, we measured the mass-weighted average of flow velocity at the plane crossing the center of the capillary network. The pressure drop was calculated from the mass-weighted average values at the inlet and outlet surfaces. The results presented in this work correspond to the mean of four technical replicates, with the coefficient of variation indicated.

2.3.4 Error analyses

Since numerical solutions are approximations, there will always be differences between the calculated results and reality. The types of systematic errors that numerical solutions introduce are: physical model error, iterative convergence error, discretization error and computer rounding error (Ferziger et al., 2020; Schwarze, 2013; Versteeg and Malalasekera, 2007). In order to conduct a high quality CFD study, these errors must be controlled and minimized.

Physical model error

Physical model errors result from uncertainties in the model formulation and deliberate simplifications of the model (Versteeg and Malalasekera, 2007). They relate to the choice of governing equations and assumptions about fluid properties. Estimating model errors requires validation against experimental data. In this work, we could not determine the model

error because no suitable experimental data was available. However, we could ensure the other systemic errors were as small as possible, as they must be substantially smaller in magnitude than the model error in order to be able to estimate the latter in the future.

Iterative convergence error

The iterative convergence error is defined as the difference between the numerical (iterative) and the exact solution of the discretized equations (Versteeg and Malalasekera, 2007). The error magnitude depends on the stopping point of the iterative method. To identify an ideal stopping point at which the iteration error is sufficiently small, certain sensors are monitored and convergence criteria are introduced. These sensors include residual values, solution imbalances and coefficients of variation of target values (Figure 2.7). For every iteration, the residual values indicate the local imbalances of variables within each control volume (ANSYS, 2009c). For each variable, residual values from all control volumes are summed, scaled by a flow rate representative scaling factor, and then normalized. Convergence criteria are met and the iteration process is stopped when residual norms fall below a specific threshold. We set this threshold to $1 \cdot 10^{-5}$.
Furthermore, we applied a "human-in-the-loop" approach to verify the other sensors. After convergence was indicated, manual checks were performed to ensure the global mass balance approached zero (values ranged from 10^{-18} to 10^{-13} kg/s). Additionally, we ensured that the target values had stabilized at a constant level. The coefficients of variation for the mean capillary velocity ranged from $8.2 \cdot 10^{-8}$ to $1.5 \cdot 10^{-4}$, while those for the pressure drop ranged from $7.6 \cdot 10^{-7}$ to $3.1 \cdot 10^{-4}$.

Discretization error

The discretization error arises from truncation error, which is the difference between the continuous and the discrete representations of the governing equations (Schwarze, 2013; Ferziger et al., 2020). The discretization error corresponds to the discrepancy between the respective solutions. Both errors are influenced by the choice of discretization scheme and the size and quality of the mesh. Most importantly, they scale with the mesh width, i.e., the size of the control volumes. Moreover, mesh orthogonality enhances accuracy of spatial discretization and interpolation. The same holds for a uniform size ratio among neighboring control volumes. Consequently, the quality of our meshes was evaluated carefully (Section 2.3.2). Using finer meshes reduces discretization errors, but it also demands higher computational resources. Hence, it is crucial to assess the discretization error and determine an optimal mesh width that strikes a balance with the available computational capacity. We compared two meshes with different levels of complexity (Table 2.4). The results presented in this work were obtained using the fine meshes. We estimated the

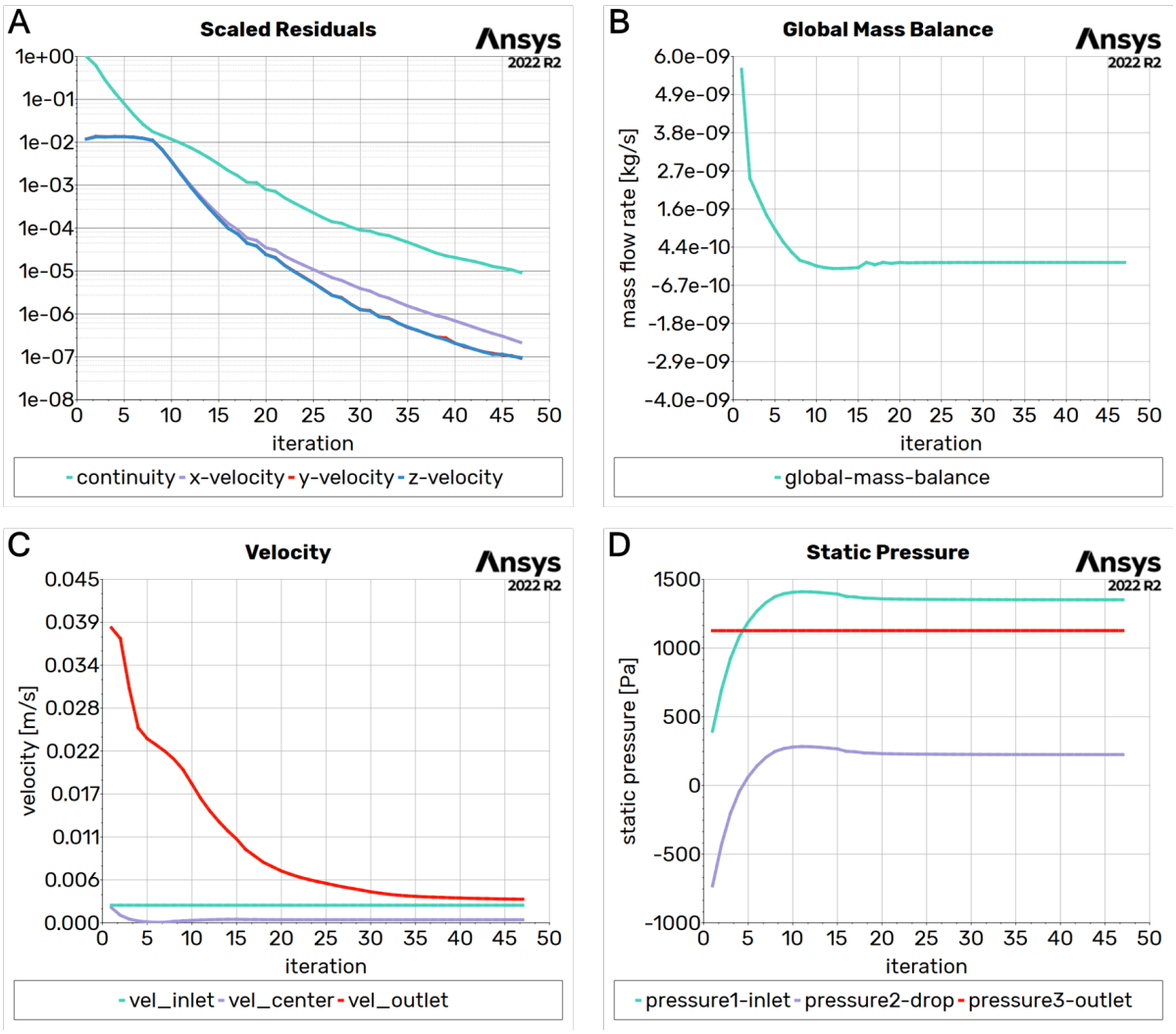

Figure 2.7: The iterative convergence of the computational fluid dynamics solution was systematically assessed using multiple sensors. First, residual values of model variables (A) were employed to gauge their imbalance in the finite volume equations. Our convergence criterion required that these residuals, having been scaled and normalized, fell below a predefined threshold of $1{\cdot}10^{-5}$. Additionally mass balances (B) were monitored by calculating the sum of the mass flow rates of all inlet and outlet surfaces. In the case under consideration, the global mass balance reached $-1.3{\cdot}10^{-15}$ kg/s at the end of the iteration process. Lastly, we ensured the convergence of the target values, mean capillary flow velocity (C) and pressure drop (D). In this specific instance, the mean flow velocity had stabilized at 0.398 mm/s when the simulation had stopped, with a coefficient of variation of $5.7{\cdot}10^{-5}$. The pressure drop, with a value of 1.68 mmHg (224 Pa), exhibited a coefficient of variation of $3.1{\cdot}10^{-5}$ over the last ten iterations.

corresponding discretization errors by applying Richardson extrapolation with the coarse

meshes (Schwarze, 2013), as follows:

$$e_h \approx \frac{f_{fine} - f_{coarse}}{r^p - 1}, \tag{2.11}$$

where f_{fine} and f_{coarse} are the solution on the fine and coarse meshes, respectively, r is the refinement factor between the two meshes and p is the order of the discretization scheme. In our simulation results for the mean capillary velocity, the discretization error ranged from 0.15 % to 0.39 % of the velocity values. For the pressure drop, the discretization error was between 0.09 % to 0.95 % of the result values.

Computer rounding error

Rounding errors in computation depend on the precision with which floating numbers are stored in the computer. In our true-to-scale models, we employed double precision, following Ansys' recommendation for FV meshes with exceptionally small minimum face areas. (The minimum face area in our meshes is on the order of 10^{-19} m^2.)

2.3.5 Sensitivity analyses

We performed sensitivity analyses to assess how the simulation results are affected by variations in the boundary conditions at the inlet and outlet, as well as changes in the fluid properties of density and viscosity. For this purpose, we varied these parameters separately, while keeping the remaining parameters at the standard settings used in our main experiments (Table 2.6). The value ranges for boundary conditions and fluid density were selected to have, in our estimation, reasonable magnitudes, with our standard values positioned approximately in the middle of their respective range: The inlet velocity was varied from 0.5 mm/s to 3 mm/s in increments of 0.25 mm/s. The outlet pressure was varied from 500 Pa (3.75 mmHg) to 1500 Pa (11.25 mmHg) in increments of 100 Pa. The density was varied between 500 kg/m^3 and 1500 kg/m^3 in increments of 100 kg/m^3. The viscosity was varied between 0.001 kg/(m·s) and 0.056 kg/(m·s) in increments of 0.0055 kg/(m·s). This range of values was chosen to encompass both the viscosity value of our Newtonian fluid model (0.002 kg/(m·s)) and all values that can be adopted within the non-Newtonian viscosity model.

Flow velocity within the model depends on the mass flow rate and fluid density (Equation 2.5). Mass flow rate in our system is governed by the inlet velocity boundary condition. Indeed, we observed a linear relationship between inlet velocity and the mean flow velocity within capillaries (Figure 2.8 A). Meanwhile, variations in outlet pressure, fluid viscosity and density did not have any effect on the mean flow velocity within the ACN, as we had anticipated.

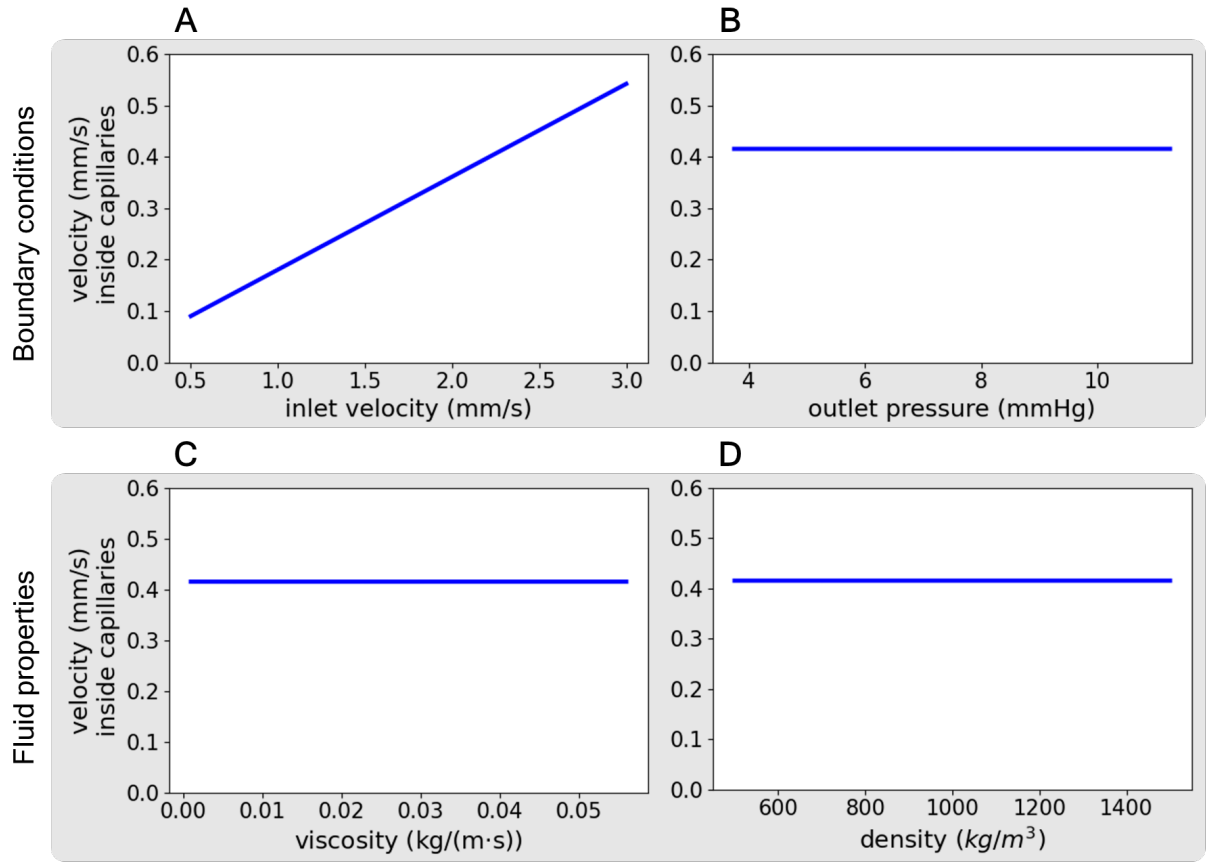

Figure 2.8: Sensitivity analyses for the effects of the boundary conditions inlet velocity (A) and outlet pressure (B), as well as the fluid properties viscosity (C) and density (D) on the target value mean flow velocity within capillaries. Simulations were performed in the default model geometry with one arteriole (inlet) and one venule (outlet), both 20 µm in diameter.

In order to understand the dependence of the pressure drop on the boundary conditions and the fluid properties, the conservation of momentum (Equation 2.7) must be taken into account in addition to the continuity equation. Here, the stress tensor and thus a dependence on fluid viscosity comes into play. The results of the sensitivity analyses are consistent with these expectations (Figure 2.9). The pressure drop depends linearly on both the inlet velocity and the fluid viscosity. While variations in outlet pressure affected the overall pressure in the model, the relative pressure drop remains unchanged. The variation in fluid density did not have an effect on this target value either.

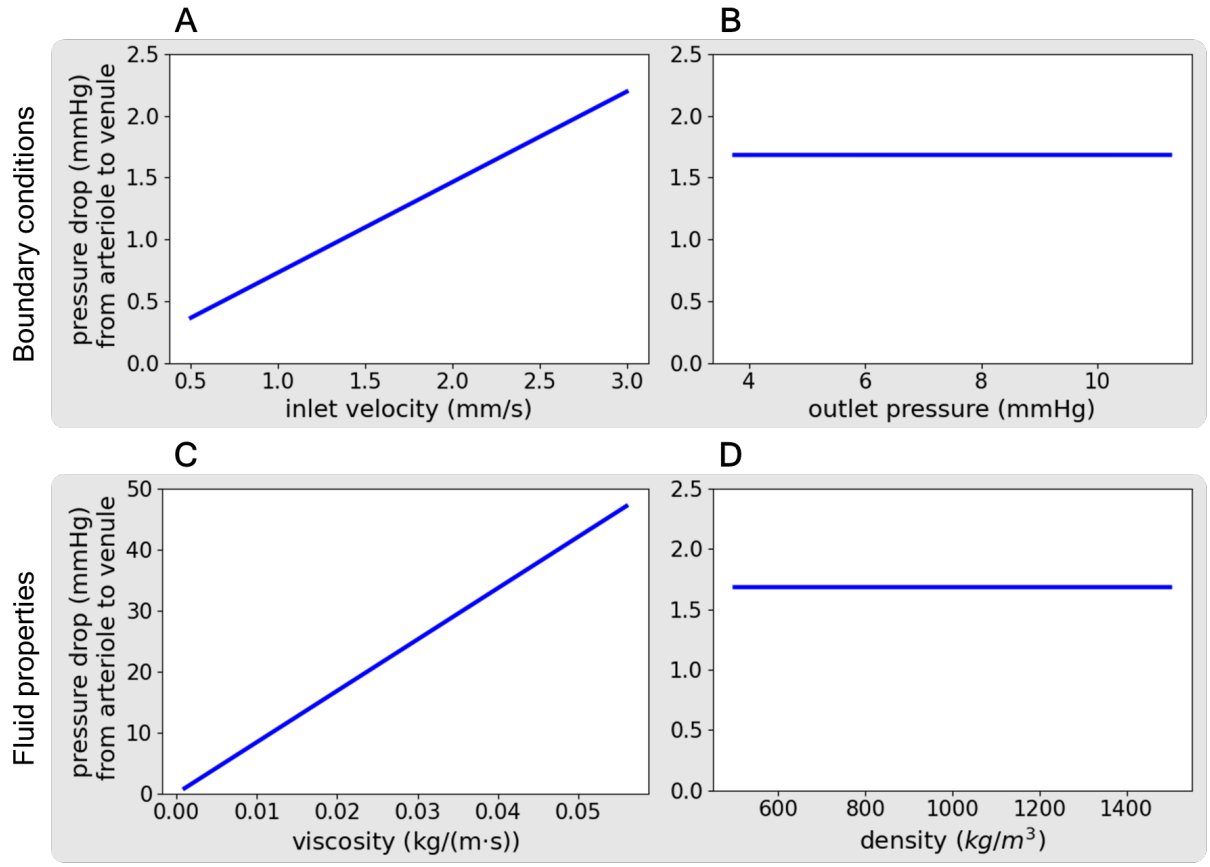

Figure 2.9: Sensitivity analyses for the effects of the boundary conditions inlet velocity (A) and outlet pressure (B), as well as the fluid properties viscosity (C) and density (D) on the target value pressure drop from arteriole to venule. Simulations were performed in the default model with one arteriole (inlet) and one venule (outlet), both 20 µm in diameter.

Chapter 3

Results

3.1 Verification and validation of the mathematical model of gas exchange.

We developed a spatio-temporal model of the entire respiratory oxygen transport from inspired air to the hemoglobin in the blood (Section 2.1.2). All essential model parameters and their default values were taken from the literature. They represent a normal, healthy state (Table 2.1). This model had to be verified and validated. First, we considered our submodels from step 1 and step 2 individually and verified that we had appropriately adopted them from the literature.

Along with their diffusion equation (Equation 2.1), Weibel et al. (1993) have estimated a value of 0.079 ml/(s·mmHg·kg) for the membrane diffusion capacity (DMO_2) of the whole lung relative to body weight (bw). Assuming a standard body weight of 70 kg, this results in a value of $DMO_2^{(\text{Weibel, bw 70 kg})}$ = 5.53 ml/(s·mmHg). Within our model framework, we estimated oxygen diffusion within a single alveolus. To make a meaningful comparison between Weibel's estimate and our model result ($DMO_2^{(\text{model})}$), we needed to extrapolate it to the organ scale. By multiplying $DMO_2^{(\text{model})}$ by a number of $480 \cdot 10^6$ alveoli in the human lung (Ochs et al., 2004), we obtained a $DMO_2^{(\text{model, extrapolated})}$ of 2.88 ml/(s·mmHg), which is markedly lower than the $DMO_2^{(\text{Weibel, bw 70 kg})}$. Weibel et al. (1993) based their estimate on morphometric measurements conducted on fully inflated, fluid-filled lungs. However, it is acknowledged that in an air-filled lung, only approximately 60-70% of the alveolar surface is exposed to air (Gil et al., 1979; Bachofen et al., 1987). Our model's default surface area value (121000 μm^2) was based on a study on perfusion-fixed, air-filled lungs (Mercer et al., 1994). Since DMO_2 is proportional to the gas exchange surface area, it is plausible that the difference between our result for DMO_2 and the estimate from Weibel is due to the different assumptions on the alveolar surface area. Indeed, when we increased the alveolar surface area setting in *Alvin* to 207000 μm^2 (a value measured in fluid-filled lungs (Stone

et al., 1992)), we obtained a DMO_2 of 4.9 ml/(s·mmHg) which was substantially closer to Weibel's estimate. Nevertheless, we consciously opted for the surface area value from the perfusion-fixed lung study as the default setting in *Alvin* to align as closely as possible with the *in vivo* situation.

The submodel that describes the hemoglobin oxygen saturation was taken directly from Dash et al. (2016) without modification. We recreated Hb-O_2 dissociation curves across various parameter ranges outlined in this publication (Figure 4 E-H in Dash et al. (2016)), and these curves indicate a correct implementation of the model (Figure 3.1).

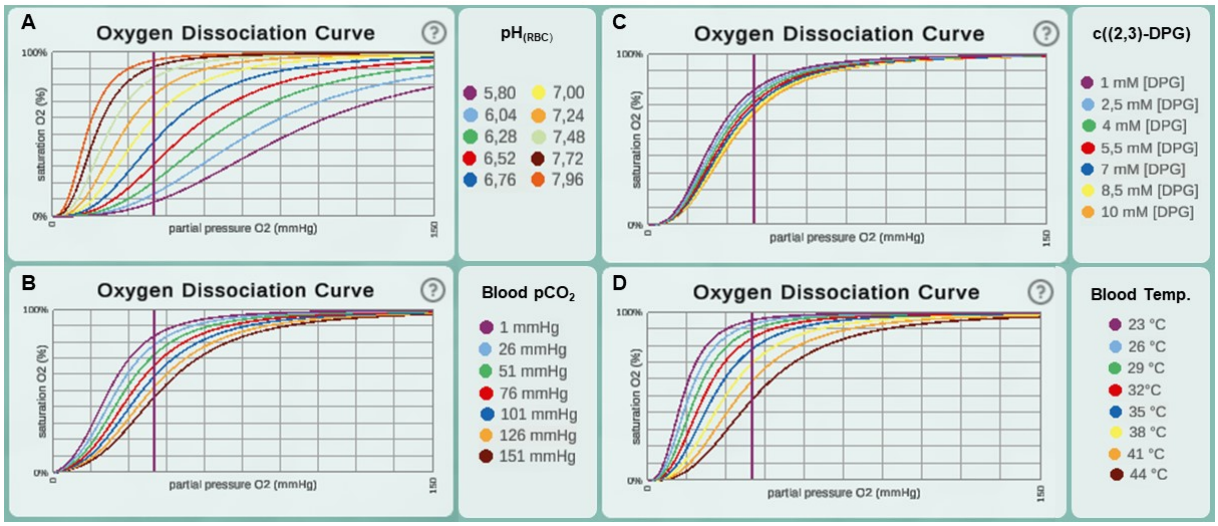

Figure 3.1: Parameter sweep for the oxygen dissociation curve following the example of Dash et al. (2016). This encompasses parameter value ranges for A) pH in erythrocytes (pH_{rbc}), B) blood pCO_2, C) concentration of [2,3]-DPG and D) blood temperature. Taken from Schmid et al. (2022).

Beyond that, we validated the complete model using published experimental data. An essential feature of our model is its temporal and spatial resolution. Instead of mean values, our model provides information about oxygen partial pressure and saturation gradients along the alveolar capillary. We observed that hemoglobin saturation with oxygen reaches equilibrium by the end of the capillary. This temporal resolution permits the determination of parameters of physiological interest such as reaction half-time. Reaction half-time is defined as the time it takes until 50% of the oxygenation that blood undergoes during its transit along the alveolus is completed. With default parameter settings in *Alvin*, this time is 0.04 s for a total increase in saturation from 81% to 97% (Figure 3.2). A corresponding measurement in mice recorded a time of 0.037 s (Tabuchi et al., 2013), and it has been argued that there are only minor variations across species (Lindstedt, 1984).

In summary, we have shown that we have properly adopted and reasonably adapted existing models of different gas exchange processes. As a result, we obtain our integrative,

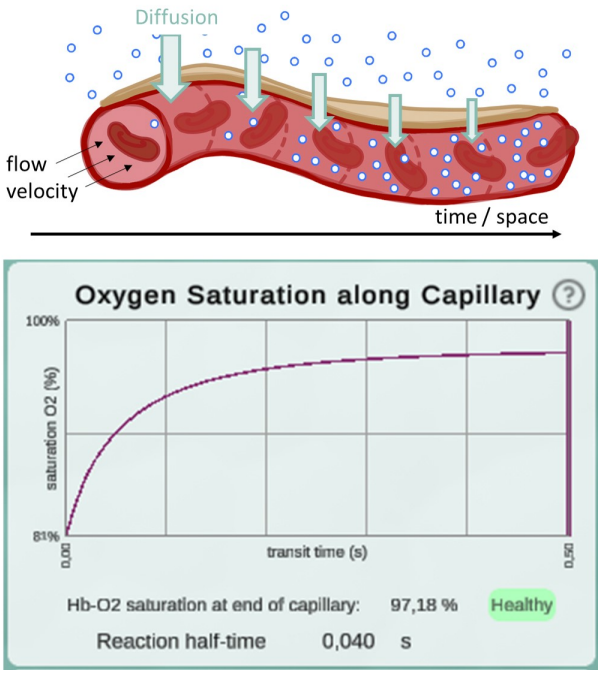

Figure 3.2: The intensity of diffusion gradually decreases along the model capillary (top). Along this trajectory, the oxygen saturation in the blood initially rises rapidly until it approaches a maximum. A screenshot of the output graph for oxygen saturation along the capillary in *Alvin* (bottom) displays this process for a simulation with pO_2 values of 97 mmHg in the alveolar space and 46 mmHg in the deoxygenated blood. All other parameters were retained at their default settings. The reaction half-time refers to the time point when 50% of the blood's oxygenation during its transit along the alveolus is attained. Taken from Schmid et al. (2022).

time-resolved model, which produces results in agreement with experimental data (meeting S.1, Section 2.1.1).

3.2 *Alvin*: An interactive platform for exploring alveolar-level gas exchange

Interaction with content improves the quality of insight (He et al., 2021; Pike et al., 2009) and facilitates deeper exploration of concepts. Following the establishment of our mathematical model, we developed the *Alvin* simulation software to foster the conception and exploration of the process of gas exchange within an individual alveolus.

3.2.1 Visualization

Alvin is a desktop application implemented in Unity. It is accessible across Windows, macOS, and Linux environments (meeting A.1, Section 2.1.1). The following components shape the user interface of *Alvin*: a three-dimensional visualization of an alveolus illustrating the simulation process, a configuration menu for the model parameters and a panel with dynamic graphs (Figure 3.3). One feature worth highlighting is the option to run and compare multiple simulation instances at the same time. Two different prototypes of the application were developed for the use in teaching and in research (Section 2.1.3).

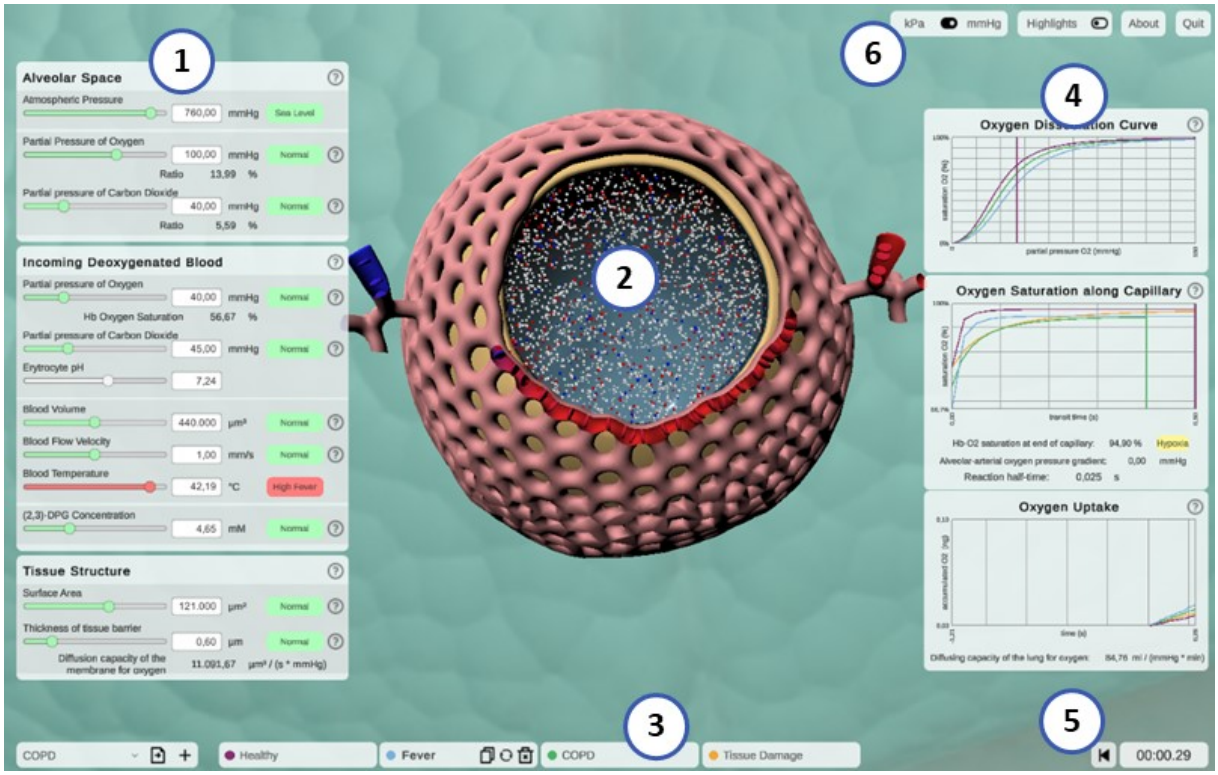

Figure 3.3: A screenshot showcasing the interactive application, *Alvin*. (1) Model parameters are grouped into categories. They can be configured. Colors and information text provide possible real-world context for the values. (2) An animated simulation of an alveolus corresponds to the active parameter set, offering a visual representation of the effect of model parameter values. (3) The possibility to compare multiple simulation instances increases the exploratory value of the application. (4) Dynamic plots color-coded for each active instance of the simulation present quantitative simulation results. (5) Simulation time is monitored and can be reset as needed. (6) Utility functions and settings are available. Taken from Schmid et al. (2022).

The dynamic, three-dimensional model of an alveolus serves as a visual representation of the ongoing simulation (Figure 3.3, center). The alveolus model contains small animated spheres representing air molecules in Brownian motion. Each of these spheres corre-

sponds to approximately $2{\cdot}10^9$ molecules of oxygen (red), carbon dioxide (blue) or nitrogen (white). Changes in the model parameter "thickness of tissue barrier" are visually indicated by the thickening or thinning of the tissue layer. Animated erythrocytes traverse the cut-open capillary, their number resulting from the blood volume setting and a standard value of $5{\cdot}10^6$ cells per µl blood (Pagana et al., 2019). The relative position of an erythrocyte along the capillary path is constantly traced. The model calculates gradients in oxygen partial pressure (Equation 2.1) and hemoglobin oxygen saturation (Equation 2.2) along this same path. Consequently, erythrocytes are color-coded based on their oxygen saturation, and the cumulative amount of oxygen taken up by the erythrocytes throughout the simulation is recorded (Figure 3.3, graph "oxygen uptake"). For visualization purposes, simulation time is decelerated by a factor of 40 compared to the gas exchange process occuring *in vivo*. If several simulation instances are active, only the course of the selected instance is visualized in the 3D model.

Taken together, one can appreciate the simulated gas exchange process by observing the movement of the gas spheres as they cross the tissue barrier and the changes in color of the capillary and erythrocytes. To quantitatively assess the simulation results, three distinct graphs are provided (meeting S.3, Section 2.1.1) (Figure 3.3, right). They show the oxygen saturation of hemoglobin as a function of pO_2 in the blood (oxygen dissociation curve), or as a function of time (oxygen saturation along capillary). The total amount of oxygen acquired is recorded as a function of the time since the start or reset of the simulation (oxygen uptake). Each graph corresponds to a specific simulation instance, distinguished by its unique instance color.

3.2.2 Interactivity

The user can adjust model parameter values via the parameter panel (Figure 3.3, left) whereupon the 3D visualization and the quantitative graphs update in real-time (S.2, Section 2.1.1). A traffic light color code and keywords help to classify the selected parameter values in relation to their healthy or pathological range (E.2, Section 2.1.1). Users can access more detailed information by clicking on the respective info button, indicated by a question mark. To enhance user experience and comprehension, model parameters are categorized based on their association with specific compartments of the tissue (alveolar air, blood or tissue barrier). Visual cues within the 3D alveolus model accentuate these associations (S.4, Section 2.1.1). For example, when the cursor is moved over the window with the model parameters related to the blood, all tissue components except the capillary are color-muted. Users can explore the 3D model in depth by moving, rotating or zooming it. Furthermore, hovering the mouse over a graph provides detailed quantitative information. The instance menu allows multiple simulation instances to be run simultaneously for direct

comparison of different parameter settings (Figure 3.3, bottom). Consistent coloring and customized naming simplify the distinction between different simulation instances. Users can copy, delete, or reset a selected instance to its initial parameter values. Parameter presets are provided for healthy and common pathogenic conditions (E.1, Section 2.1.1) (Table 3.1). Finally, there are control elements for monitoring or resetting simulation time and for switching between pressure units and visual highlighting modes.

Pathogenic Condition	**Pathophysiology / Symptom**	**Parameter Value Shift**
Pneumonia	Fever Tissue damage Accumulation of fluids and dead cells	Temperature ↑ Surface area ↓ Barrier thickness ↑
ARDS (acute respiratory distress syndrome)	Collapse (alveolar aelectasis) Fever	Surface area ↓↓ Temperature ↑
COPD (chronic obstructive pulmonary disease)	Impaired exhalation Impaired exhalation Tissue damage	Alveolar pCO_2 ↑ and blood pCO_2 ↑ Alveolar pO_2 ↓ Surface area ↓
Pulmonary fibrosis	Thickened and scarred connective tissue Impaired inhalation	Barrier thickness ↑ Alveolar pCO_2 ↓
Pulmonary embolism	shunt shunt	Blood volume ↓↓ Blood flow velocity ↓↓

Table 3.1: A set of parameter presets is available to represent pathogenic conditions. Each condition reflects pathophysiological issues or symptoms through increased (↑) or decreased (↓) values of certain model parameters.

In summary, the applications interactivity is highlighted by its real-time parameter adjustments, detailed quantitative feedback through graphs, and the simultaneous execution of multiple simulation instances for easy comparison. In parallel, its visualization features a dynamic 3D alveolus model, where changes in parameter values are visually represented, thus offering users an immersive and informative experience.

3.3 Examples of use of the *Alvin* application in teaching and research.

We present two practical examples of the application of *Alvin*. The first involves the integration of *Alvin* into a virtual lab course at university level. The second is the use of the interactive simulation for interpretation of published data.

3.3.1 Integration of *Alvin* into a university level physiology lab course

In the context of education, the advantages of employing interactive simulations have been recognized and utilized early on (Dewhurst et al., 1988; Davis and Mark, 1990), and this approach continues to be explored today (Jacob et al., 2012; Tworek et al., 2013). Thus, we introduced *Alvin* into a university-level course on human biology, specifically within an online practical session covering topics related to blood and respiration. In this course, *Alvin* served as an interactive tool to illustrate the interplay between the circulatory and respiratory systems. To assess the suitability of *Alvin* for this educational context, we conducted an online questionnaire. The course had a duration of 2 hours and 45 minutes and was attended by students of teaching Biology, specifically of the German levels of *Grundschule* (elementary school), *Mittelschule* (secondary school) and *Gymnasium* (grammar school). The session began with a 45-minute lecture introducing the topic of 'Blood and Respiration.' Subsequently, *Alvin* was briefly presented, demonstrating how to navigate the application, interpret the 3D model, and understand the dynamic graphs. Participants were then given a few minutes to become acquainted with *Alvin*, followed by a request for their feedback on engaging with the application. We provided an online questionnaire to collect feedback from the participants. Participation in the survey was voluntary and attendees had the option to withdraw at any point during the event. Completing the entire questionnaire or responding to individual questions was not mandatory. The questionnaire was divided into four parts, and a translated version of the entire questionnaire can be found in the supplementary material (Section S.1).

The first part comprised a general demographic questionnaire, which was supplemented with specific inquiries about the students' formal background and their familiarity with the

subject. We collected a total of N = 101 submissions. Out of these N = 101 responses, 11 individuals identified as male, while 81 identified as female. The second part included 13 exercises centered around respiratory processes within the alveolus. These exercises contained guidance on how to involve *Alvin* in the solution approaches. They explored various topics, including well-known concepts like the Bohr effect (Riggs, 1988). The average overall score for all participants was 2.07, measured on a scale of 1-4, with 1 indicating perfect answers (Figure 3.4 A). Any unanswered questions were assigned a score of 4. Most exercises were completed correctly, with only a few incorrect answers; the majority of score 4 ratings were due to missing responses. Two standardized questionnaires designed to evaluate the visual aesthetics and the usability of the application formed the third section of our online survey: Visawi-s (Visual Aesthetics of Websites Inventory - short version) (Moshagen and Thielsch, 2010) and QUESI (Questionnaire for Measuring the Subjective Consequences of Intuitive Use) (Hurtienne and Naumann, 2010). Visawi-s (Moshagen and Thielsch, 2010) assesses four fundamental dimensions of aesthetics from the user's standpoint: simplicity, diversity, colorfulness, and craftsmanship. Participants were presented with statements addressing these four dimensions and asked to rate them on a scale from 1 (strongly disagree) to 7 (strongly agree). The collective mean Visawi-s score, comprising N = 72 responses, amounted to 5.8 (Figure 3.4 B). The standardized QUESI questionnaire is grounded on the premise that intuitive use arises from the unconscious application of prior knowledge, leading to effective interaction (Hurtienne and Naumann, 2010). It is a measure for usability, divided into the following subscales: Subjective mental workload, perceived achievement of goals, perceived effort of learning, familiarity, and perceived error rate. The overall score of the questionnaire corresponds to the mean across all five subscales. Generally, higher scores indicate a greater probability of intuitive use. The assessment of *Alvin* by participants (N = 69) yielded a QUESI score of 2.98 (Figure 3.4 C). Published benchmark scores for mobile devices and applications (Naumann and Hurtienne, 2010) vary from 2.39 (Alcatel One Touch 311) to 4.23 (Nintendo Wii). Moreover, it's worth noting that familiar products tend to perform better in the QUESI (Naumann and Hurtienne, 2010). Therefore, participants' previous experience with similar systems in a broader sense, such as computer games in general, is relevant. The majority of our participants (N = 59) reported rarely (yearly to never) playing computer games, while a minority (N = 29) reported frequent usage (monthly to daily).

Furthermore, the questionnaire contained open questions concerning the acceptance of the software in the educational context. One of these questions was "Which benefits do you see in this system compared to a traditional textbook?". An analysis of the responses showed that the most frequently mentioned terms were "parameter", "better", "modify", "changes", "by oneself", "illustrative", "testing", "see", "illustrated", "apparent", "interactive", and "immediate" (Figure 3.4 D). Another question inquiring about general feedback received some

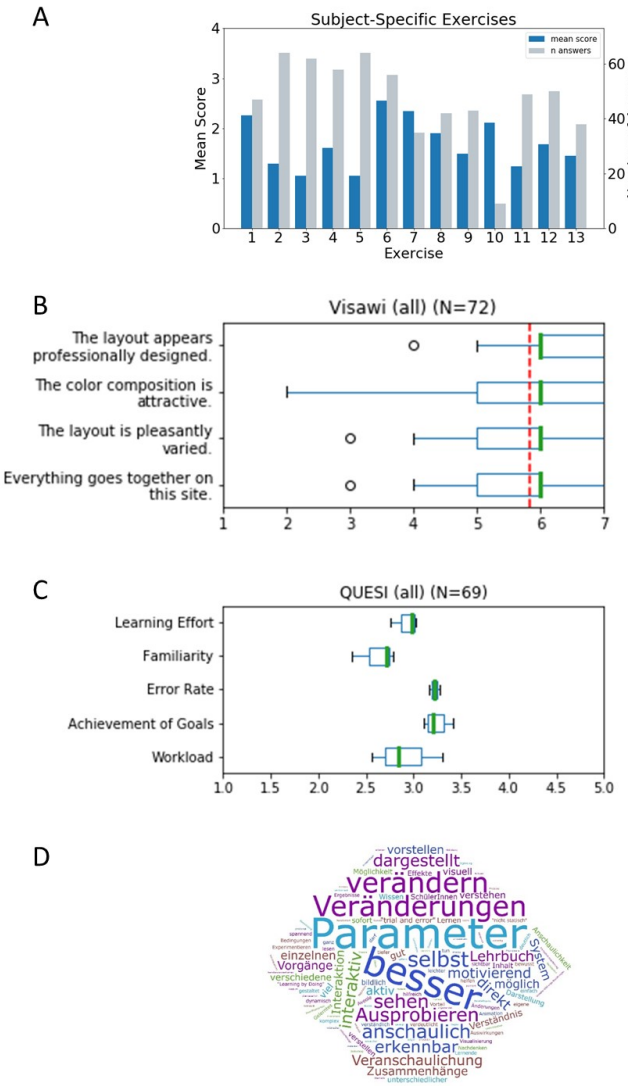

Figure 3.4: Results of a survey involving undergraduate students who engaged with *Alvin* during a physiology lab course. A) Answers to 13 subject-specific exercises were graded as either 1 - correct, 2 - partially correct (e.g., subsequent faults), 3 - unclear or 4 - incorrect / missing. For each exercise, the mean score (blue) and the number of submitted responses (grey) were presented. B) Assessment of visual aesthetics based on the standardized Visawi-s survey (Moshagen and Thielsch, 2010). 72 participant rated statements from 1 (strongly disagree) to 7 (strongly agree), the mean overall score was 5.8. C) Assessment of usability based on the standardized QUESI survey (Hurtienne and Naumann, 2010). The mean overall QUESI score across five sub scales was 2.98, aggregated from 69 surveys. D) Frequency analysis on the participant's answers to the question "which benefits do you see in this system compared to a traditional text book?". Taken from Schmid et al. (2022).

constructive criticism. Participants noted that the content of *Alvin* and the subject-specific

exercises were too complex for this introductory event. Some also expressed that more time would have been needed to become familiar with the application. Additionally, some participants encountered challenges when switching between the German lecture content and the English-language application. The participants successfully completed the subject-specific exercises for the most part, indicating that *Alvin* is a suitable tool to support solving such tasks. Responses to open-text questions revealed specific aspects of working with *Alvin* that were particularly positively perceived. These included the ability to interact with the simulation by configuring model parameters, the freedom to independently test different conditions, and the highly illustrative presentation of simulated processes in *Alvin*.
Overall, the use of *Alvin* in the physiology lab course was considered a success and has been repeated twice in a similar form.

3.3.2 Quantification of DLO_2 as a function of blood flow and available alveolar surface area.

To illustrate a potential research application of *Alvin*, we used the software to assess the plausibility of pulmonary diffusion capacity measurements. There are substantial differences in the estimations of DLO_2 in humans when based on physiological or morphological measurements. Physiological estimates are around 30 ml/(mmHg·min) at rest (Hsia et al., 2016), they are typically derived from measurements of diffusion capacity for carbon monoxide (DLCO) (Forster, 1964; Crapo and Crapo, 1983). Morphological estimates, on the other hand, yielded a value of 158 ml/(mmHg·min) (Weibel, 2009), greatly exceeding the physiological estimate. This discrepancy can be attributed to several factors (Hsia et al., 2016). One such factor is the assumption of complete capillary perfusion and the inclusion of the entire alveolar surface in the morphological estimation calculations (Weibel, 1970). In reality, however, under normal blood flow at rest, only about 50% of the alveolar capillary segments are perfused by erythrocytes and thus contribute to gas exchange (Okada et al., 1992) (Figure 3.5 A). Increased blood pressure, such as that resulting from heightened cardiac output, leads to the recruitment of additional capillary segments. In addition, the lung volume can fluctuate greatly depending on the transpulmonary pressure. At rest, the human lung holds about 3 liters of air, of which about 500 ml are exchanged per breath (West, 2012). During exercise, these values increase, and the total lung capacity is over seven liters. These fluctuations are reflected in the total surface area of the ventilated alveoli. As mentioned above, different fixation methods capture different states, resulting in significant differences between surface area measurements: A surface area of 207,000 μm^2, as measured in inflation-fixed lung tissue (Stone et al., 1992), corresponds to maximum surface exposure (100%). In contrast, Mercer et al. (1994) reported an alveolar surface area of 121,000 μm^2 in a perfusion-fixed lung. This value represents 58% surface exposure and

was chosen as the default setting in *Alvin* as it more closely reflects the physiological scenario of an air-filled lung. Capillary recruitment in *Alvin* is reflected in capillary blood volume, with the default value of 410,000 μm^3 corresponding to 50% recruitment.

We varied the ratios of capillary recruitment and alveolar surface exposure in *Alvin* and observed their impact on DLO_2. For instance, 100% alveolar surface exposure and 100% capillary recruitment in *Alvin* resulted in a DLO_2 of 200 ml/(mmHg·min). The combination of 58% alveolar surface exposure and 50% capillary recruitment lead to a DLO_2 of 62 ml/(mmHg·min).

The effect of alveolar surface area exposure and capillary recruitment on DLO_2 estimates is nearly linear (Figure 3.5 B). Interestingly, their combined effect, which mirrors the coordinated regulation of ventilation and perfusion (reviewed for example by Wagner (1981); Petersson and Glenny (2014)), results in a non-linear increase in DLO_2. This increase is gradual at first and then becomes more rapid. Conversely, an anti-parallel combination of alveolar surface exposure and capillary recruitment generally leads to low DLO_2 estimates, with a peak at 50% for each factor. Following this, we used these insights to interpret published data with the help of *Alvin*. Kulish (2006) have estimated DLO_2 from measurements of DLCO and pulmonary blood flow. We investigated the corresponding predictions of DLO_2 in *Alvin*. To do this, the amount of pulmonary blood flow, expressed as volume per unit time, was controlled by adjusting the capillary blood volume parameter. The appropriate settings for this parameter were calculated assuming a constant blood flow velocity of 1.5 mm/s, a mean capillary length of 500 µm (Weibel et al., 1993) and a maximum capillary volume of 820,000 μm^3 (Mühlfeld et al., 2010). The dependence of DLO_2 on these blood flow settings (3, 10, 20, 30, and 32 l/min) was predicted for different alveolar surface area exposures (Figure 3.5 C). Although the measured DLO_2 values were within the range of values of the published data set, the slope of all our graphs deviated from the ratio observed by Kulish (2006). Consequently, it appeared that Kulish's predictions were not based on constant alveolar surface exposure. Adjustment of alveolar surface area values (100, 87.5, 62.5, 55.0, and 60% surface exposure) together with the increasing pulmonary blood flow finally allowed to reconstruct the results at blood flow values above 10 l/min.

In summary, our exploration within *Alvin* demonstrated the pivotal roles played by parameters like alveolar surface area and capillary recruitment in influencing DLO_2. Beyond conveying such general relationships between physiological and morphological parameters and gas exchange, our showcase study also highlights the utility of *Alvin* in validating and reproducing published data.

The ability to adjust each parameter individually in *Alvin* provides considerable exploratory value and allows the effects of individual parameters to be identified in isolation. Nevertheless, this is quite unrealistic, as there are numerous dependencies among the different model parameters. For example, physiological parameters such as available blood volume

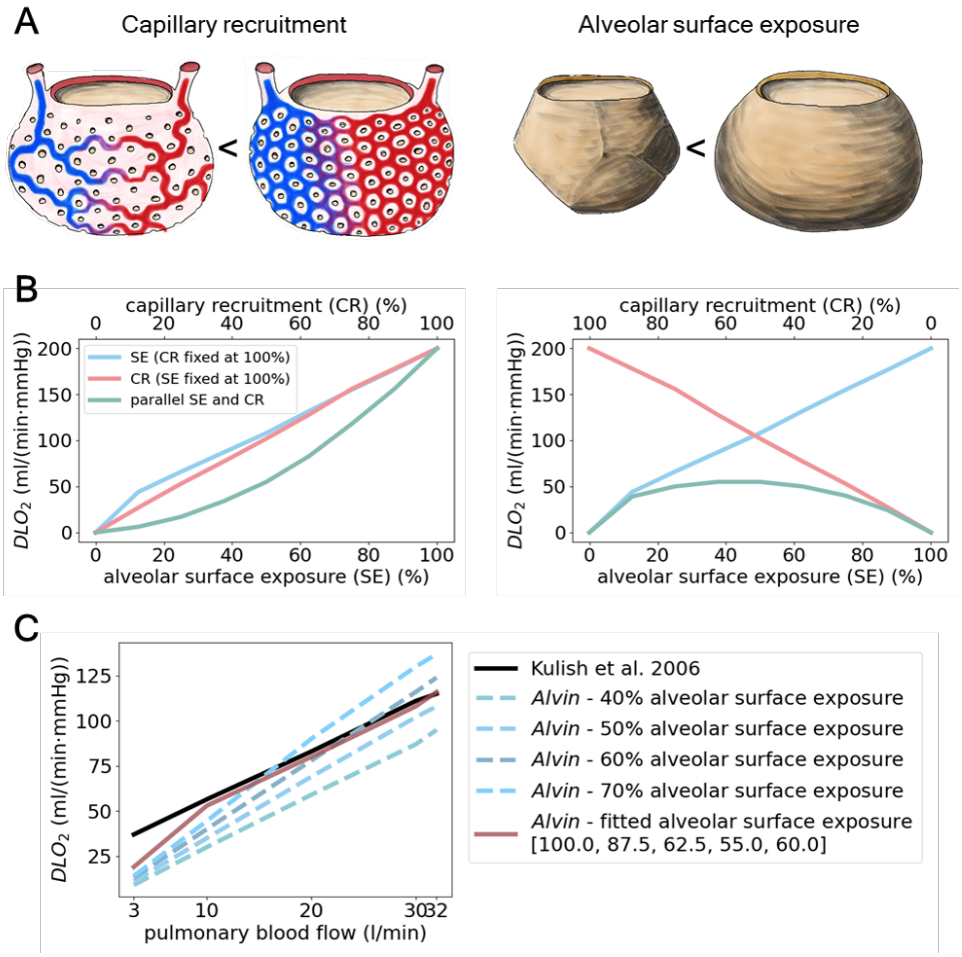

Figure 3.5: At the alveolar level, the pulmonary diffusion capacity for oxygen (DLO_2) is greatly influenced by phenomena such as capillary recruitment and alveolar surface exposure. A) Capillary recruitment in the alveolar capillary network is represented by changes in blood volume. Variations in alveolar surface exposure are a consequence of alveolar expansion during breathing. B) DLO_2's dependence on capillary recruitment and alveolar surface exposure is assessed for both parallel (left) and antiparallel combinations (right). In *Alvin*, alveolar surface exposure is simulated by incrementally increasing alveolar surface area from 0 (0%) to 207,000 µm^2 (100%) in 12.5% steps, while capillary recruitment is portrayed by an incremental increase in capillary blood volume from 0 (0%) to 820,000 µm^3 (100%) in 12.5% steps. C) A comparison with published DLO_2 estimates (Kulish, 2006) (black). In *Alvin*, pulmonary blood flow was represented by blood volume, assuming a flow velocity of 1.5 mm/s and fixed morphological boundary conditions (mean capillary length of 500 µm (Weibel et al., 1993) and maximum volume of alveolar capillary bed 820000 µm^3 (Mühlfeld et al., 2010)). Alveolar surface exposure was either defined as constant values (blue dashed lines) or adjusted with increasing pulmonary blood flow (red line). Adapted from Schmid et al. (2022).

and blood flow velocity strongly depend on the morphology of the capillary network. This led to the next objectives of this work: Firstly, to refine the geometric model of the capillary

network so that it represents stereological measurements from the literature as accurately as possible. Secondly, to assess the direct impact of the morphological properties of the capillary network on blood flow characteristics.

3.4 Data-based, 3D modeling of the human alveolar capillary network morphology

We set out to create a 3D model of the alveolar microvasculature that was true to scale and as close to reality as possible. A first step was to construct a geometric model of the alveolus using the available quantitative morphological data. If we constructed the model using literature values for the diameters of the alveolus and the alveolar opening, the resulting alveolar volume exceeded the measurements reported in the same study (Hansen and Ampaya, 1975) (Figure 3.6). Conversely, when we created an alveolar base model with the appropriate volume, the diameter was smaller than what is specified in the literature (Table 3.2). As a result, we have decided to continue using two different models: one based on the diameter ($Alveolus_D$) and the other on the volume ($Alveolus_V$).
We then constructed tube-flow and sheet-flow capillary beds around the $Alveolus_D$ and $Alveolus_V$ base models. Comparison of the ACN volume and surface area with the corresponding literature values showed that our *in silico* models yielded lower values (Table 3.3). In general, the $Alveolus_D$ ACN models were closer to the literature values than the $Alveolus_V$ ACN models. The same trend applied to the sheet-flow models compared to the tube-flow models. Overall, however, these differences were not substantial, and the truth probably lies somewhere in the middle. We chose the $Alveolus_D$ sheet-flow model for further work because it showed the best agreement with the stereological data and the modelling process was more convenient.

3.5 Prediction of blood flow using computational fluid dynamics simulations

In the next steps of this study, we wanted to gain insight into the blood flow dynamics within the alveolar capillaries. To this end, we connected the sheet-flow ACN model surrounding a single alveolus to an arteriole and a venule, 20 µm in diameter and positioned opposite each other. Using CFD simulations, we predicted the flow paths within the capillary bed, as well as the distribution of flow velocity and pressure (Figure 3.7).
Qualitatively, we observed the same flow behaviour in simulations with Newtonian and non-Newtonian viscosity models. The flow velocity within the capillaries was reduced compared

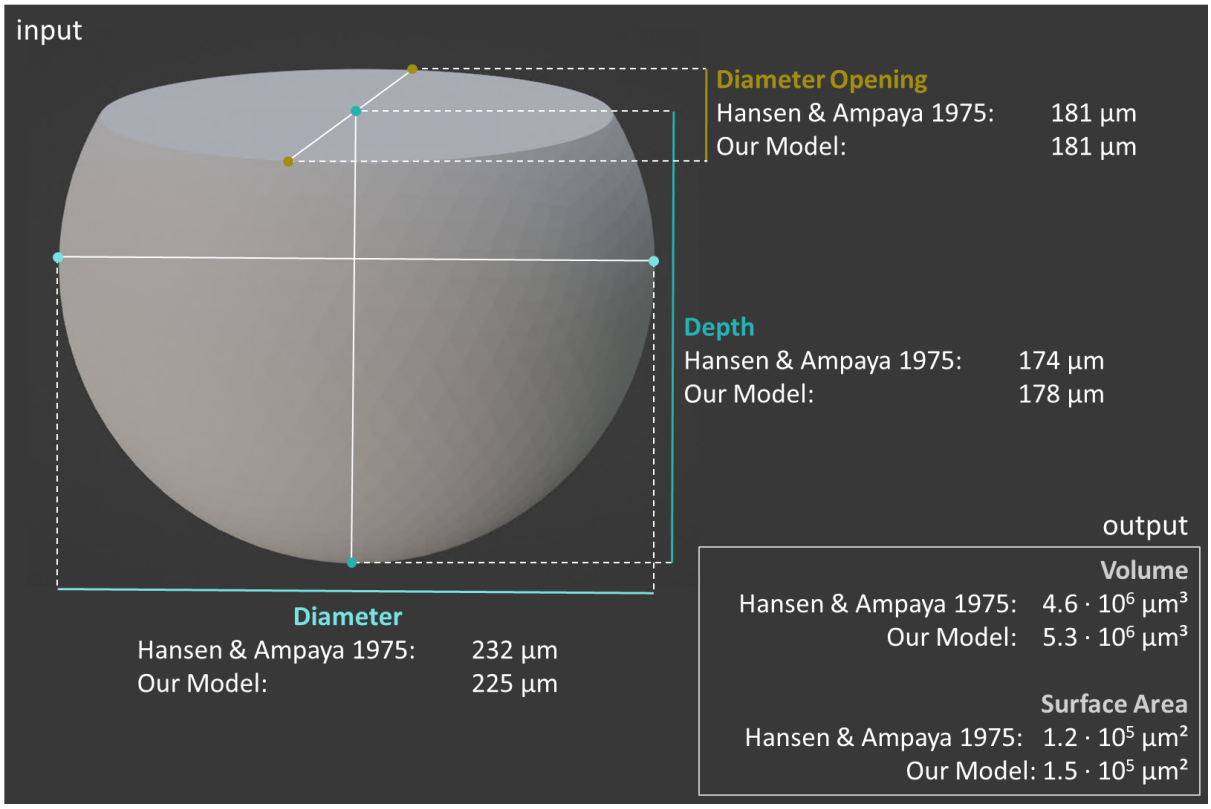

Figure 3.6: Input and output parameter values of the 3D geometrical model of an alveolus compared with morphometric measurements from the literature (Hansen and Ampaya, 1975). The basis of the 3D model was an open spheroid, with the diameter, depth, and diameter of the opening (input parameters) aligned with the corresponding literature-derived values.

to the inflow and outflow vessels, with flow primarily oriented parallel to the arteriole and the venule. This resulted in some regions of the capillary network receiving more perfusion than others. Pressure was evenly distributed across the model, with the highest pressure at the inlet surface. However, there were quantitative differences between the simulation results depending on the chosen viscosity model. The average flow velocity within the capillary network yielded robust results with 0.39 mm/s ($\pm$0.004) or 0.4 mm/s ($\pm$0.003) in the Newtonian or non-Newtonian fluid simulations, respectively. On the other hand, the pressure drop in Newtonian fluid simulations, with a value of 1.64 mmHg ($\pm$0.043), was notably lower compared to the pressure drop of 3.54 mmHg ($\pm$0.08) observed in non-Newtonian fluid simulations.

In summary, we have advanced our *in silico* approach to simulate blood flow dynamics within the morphological model, opening up new avenues for further investigations.

Parameter	Literature	*Alveolus*$_D$ Model	*Alveolus*$_V$ Model
Modeling (input)			
Alveolus - Shape	3/4 spheroid, truncated cone, 1/4 spheroid, ...[1]	3/4 spheroid	3/4 spheroid
Alveolus - Diameter (µm)	225[2], 232[1]	225	-
Alveolus - Volume (10^6 µm^3)	4.6[1], 4.2[3], 3.4[2]	-	4.6
Pores of Kohn - Number	17[4]	17	17
Pores of Kohn - Diameter (µm)	7 - 19[4], 7.2 - 16.5[5]	12.3	12.3
Alveolar Mouth - Diameter (µm)	181[1], 220[6]	181	181
Evaluation (output)			
Alveolus - Diameter (µm)	225[2], 232[1]	-	216
Alveolus - Volume (10^6 µm^3)	4.6[1], 4.2[3], 3.4[2]	5.3	-
Alveolus - Depth (µm)	174[1]	178	167
Alveolus - Surface Area (10^5 µm^2)	1.2[1,2], 2.1[7]	1.52	1.39
Alveolar Mouth - Area (10^5 µm^2)	0.3[1]	0.26	0.24

Table 3.2: Input and output parameter values of 3D geometrical models *Alveolus*$_D$ and *Alveolus*$_V$ are presented along with morphometric measurements from the literature. The key distinction between these models lies in their input parameters: *Alveolus*$_D$ is based on the diameter, while *Alveolus*$_V$ is based on the volume of an alveolus. The models were evaluated by comparing the resultant output parameters with measurements from existing literature. References: [1](Hansen and Ampaya, 1975), [2]Mercer et al. (1994), [3]Ochs et al. (2004), [4]Kawakami and Takizawa (1987), [5]Toshima et al. (2004), [6]Matsuda et al. (1987), [7]Stone et al. (1992).

3.5.1 Connectivity analyses using blood flow simulations with a Newtonian viscosity model.

With our CFD approach at hand, we were able to explore previously unknown aspects of the connection between the capillary bed and the pulmonary vascular tree. Our investigations included connectivity analyses, where we systematically varied the number (ranging from 1 to 5) and diameter (ranging from 20 µm to 60 µm) of the inlet and outlet vessels connected to the ACN model. From Newtonian CFD simulation results, we compared the two target

Parameter	Literature	*Alveolus*$_D$ Model		*Alveolus*$_V$ Model	
		sheet-flow	tube-flow	sheet-flow	tube-flow
Modeling (input)					
Capillary diameter / sheet height (µm)	6.3[1]	6.34	6.31	6.36	6.3
Capillary segment length / interpillar distance (µm)	5.9[1]	6.17	5.75	6.33	5.54
Capillary loop / pillar diameter (µm)	3*	3.1	3.78	3.23	3.56
Evaluation (output)					
Number of loops / pillars	-	1796	1569	1714	1515
Capillary volume (10^5 µm^3)	8.2[1,2]	7.12	6.09	6.32	5.54
Capillary surface area (10^5 µm^2)	5.4[1,2]	3.42	3.23	3.12	2.93
Capillary surface area, available for gas exchange (10^5 µm^2)		1.11	1.09	0.98	0.95

Table 3.3: Our *in silico* models of the human ACN have lower surface area and volume in comparison to corresponding estimates derived from morphometric studies. Four different morphological models were introduced: Around the bases of *Alveolus*$_D$ and *Alveolus*$_V$, sheet-flow and tube-flow models of the capillary network were constructed, respectively. In this process, input parameters were aligned with literature reference values. Subsequently, output parameters were determined and compared with corresponding literature benchmarks for evaluation. References: [1]Mühlfeld et al. (2010), [2]Ochs et al. (2004). *Derived from interpillar distance, assuming a ratio between pillar diameter and interpillar distance of 0.5.

values: mean flow velocity within the capillaries and arteriole-to-venule pressure drop (Figure 3.8 A and B, respectively). We observed a linear increase in both quantities as the volume of supply vessels rose. Notably, the mean flow velocity exhibited consistent behavior regardless of whether the volume increase resulted from alterations in vessel diameter or the number of vessels. The regression lines, represented by $v = -0.01 + 0.000032 \cdot V$ and $v = 0.03 + 0.000030 \cdot V$, respectively, closely aligned. However, the pressure drop showed a more pronounced increase with vessel volume when the vessel diameter was

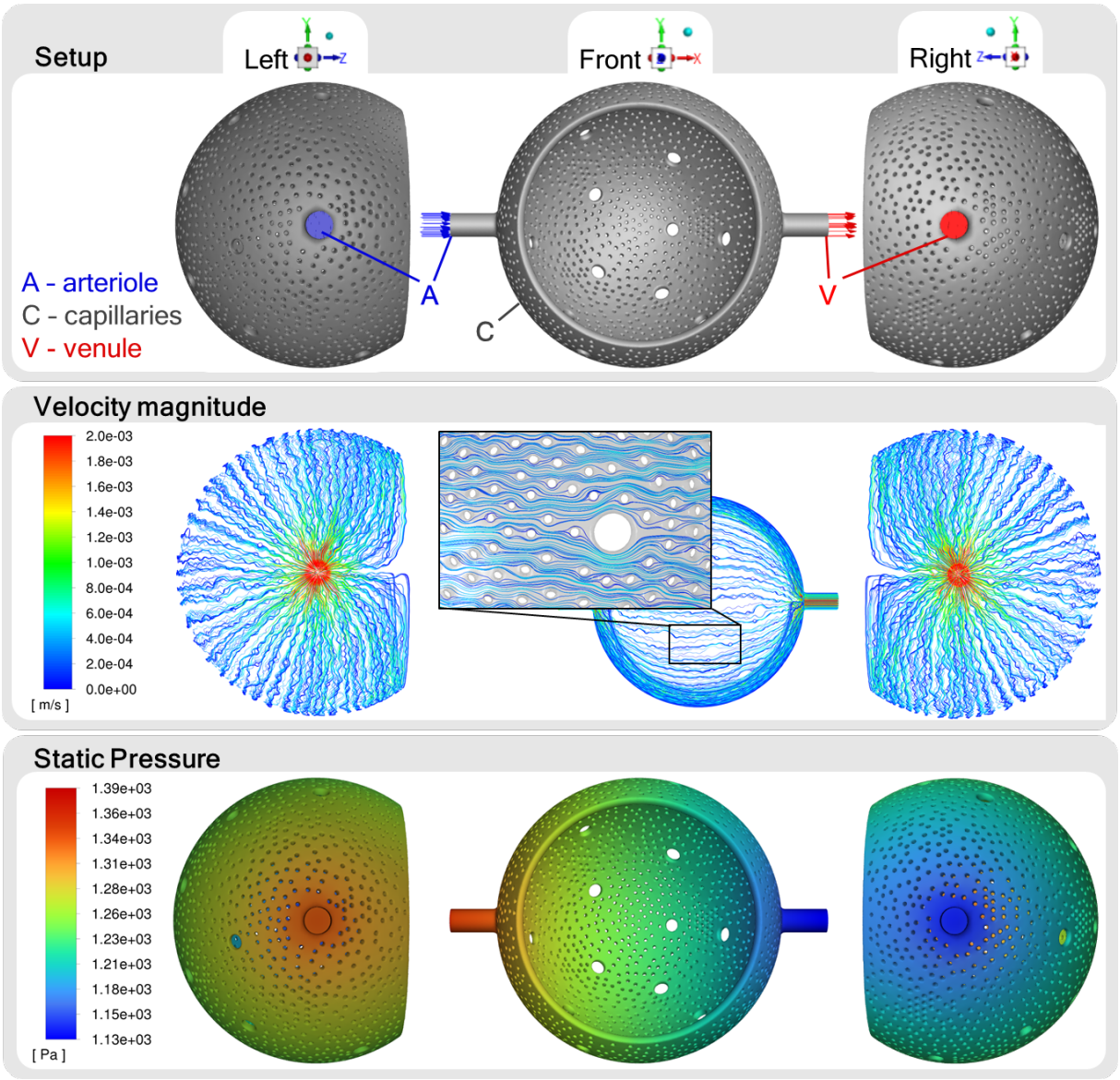

Figure 3.7: Results from computational fluid dynamics simulations in the sheet-flow model of the alveolar capillary network. One arteriole (inlet) and one venule (outlet), both with a diameter of 20 µm, were connected to the capillary sheet. Blood was approximated as a Newtonian fluid. Pathlines are color-coded based on the magnitude of flow velocity. The distribution of pressure is represented by a heatmap.

enlarged ($v = 0.83 + 0.00008 \cdot V$) in comparison to the increase resulting from a higher number of vessels ($v = 1.01 + 0.00005 \cdot V$).

In the following step, we introduced asymmetric model sets. In these sets, the modifications were limited to either the number or the diameter of one type of vessel, while the other type of vessel remained at its default setting (one vessel with a diameter of 20 µm). Again, CFD simulations were performed with a Newtonian viscosity model. The CFD results of the

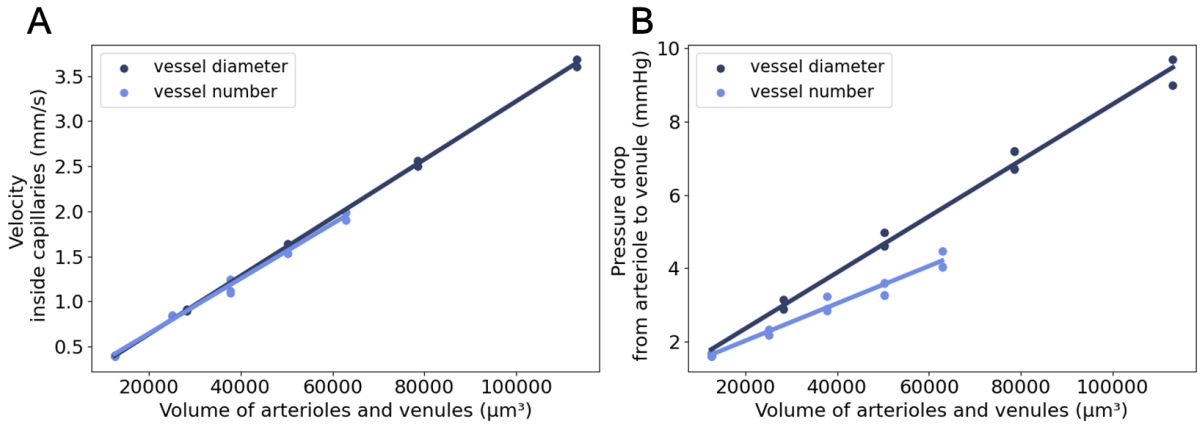

Figure 3.8: Comparison of CFD simulation results between models with different connectivity settings. Either diameter (dark blue) or number (light blue) of arterioles and venules connected to the ACN were increased. Blood was approximated as a Newtonian fluid. From the CFD simulation results, the mean flow velocity within capillaries (A) and the pressure drop from arteriole to venule (B) were plotted against the volume of the inlet- and outlet vessels.

target values were juxtaposed with the results of the symmetric connectivity models (Figure 3.9). When only arterioles were added or their diameter was increased, we observed no substantial change in flow velocity compared to the symmetric models. However, there was a slightly more pronounced increase in pressure drop in the asymmetric models with increased arteriolar supply compared to the symmetric models. On the other hand, increasing the number or diameter of connected venules alone did not result in a clear effect on the target values. Measurements at various locations within the 3D model unveiled that the asymmetric configuration of venules exclusively affected flow velocity within the venules, but not within the capillaries (supplementary Figures S.1 and S.2).

Our CFD results were compared with available reference values for different species, starting with the mean flow velocity (Figure 3.9 A). We set the boundary condition for inlet velocity at 2.29 mm/s based on measurements in arterioles of bullfrogs with a diameter of 50 µm (Horimoto et al., 1979). In alveolar capillaries, a mean velocity of 1.78 mm/s has been documented in the same study. Notably, our models featuring arterioles with a diameter of 50 µm exhibited a higher mean capillary flow velocity of 2.53 mm/s. Instead, capillary velocities closely matched those observed in bullfrogs when our models were connected to either a single arteriole with a 40 µm diameter (1.61 mm/s) or five arterioles with 20 µm diameters each (1.95 mm/s). In a study on rabbits reporting supply vessels with a mean diameter of 25 µm, a capillary velocity of 0.75 mm/s has been measured (Schlosser et al., 1965). This observation agrees well with our findings, as the value falls within the range of mean capillary velocities measured in our models connected to single arterioles

of 20 µm (0.39 mm/s) and 30 µm (0.91 mm/s) diameter. Alternatively, this benchmark was also closely approximated in our models linked to two arterioles, each with a diameter of 20 µm (0.84 mm/s). Regarding the boundary condition for pressure at the outlet (venules), we selected a value of 8.46 mmHg based on measurements in cats (Nagasaka et al., 1984). This study also provided pressure measurements in arterioles, allowing us to calculate a pressure drop of 2.87 mmHg. In this reference, arterioles had reported diameters ranging from 30 µm to 40 µm, while venules ranged from 30 µm to 50 µm in diameter. In the case of dogs and vessels with diameters between 30 µm and 50 µm, a pressure drop of 3.9 mmHg has been measured (Bhattacharya and Staub, 1980). Consistent with this, we detected pressure drop values ranging from 3.02 mmHg to 4.8 mmHg in our models with single arterioles ranging from 30 µm to 40 µm in diameter (Figure 3.9 B). Bhattacharya and Staub (1980) have reported a pressure drop of 3.3 mmHg between arterioles and venules with diameters of 20 µm, closely matched by a value of 3.1 mmHg in our models with three 20-µm-arterioles and -venules. In summary, our simulation results were within the range of literature values from various species.

3.5.2 Connectivity analyses using blood flow simulations with a non-Newtonian viscosity model

Complementary, we conducted the connectivity analyses using a non-Newtonian viscosity model (Figure 3.10). Again, the resulting mean capillary flow velocities closely resembled those obtained with the Newtonian viscosity model. Generally, the velocity values aligned similarly well with literature values, including the minor discrepancies in arteriolar diameter. The pressure drop exhibited an even stronger increase with values reaching up to 23.01 mmHg ($\pm$0.64) in the model with a 60 µm-diameter-arteriole and a 20-µm-diameter-venule. Notably, only the pressure drop in models with a single arteriole of 20 µm diameter fell within the range of literature values. Thus, a contradiction arose, as velocity values suggest that the ACN of an alveolus is supplied by at least two arterioles or a single arteriole with a diameter of at least 30 µm.

Concluding, the blood flow simulations in our connectivity models, on the whole, produced results consistent with published benchmarks of blood flow dynamics in alveolar capillaries. While the choice of viscosity model had little effect on the mean flow velocity, substantial variations were observed in the pressure drop results.

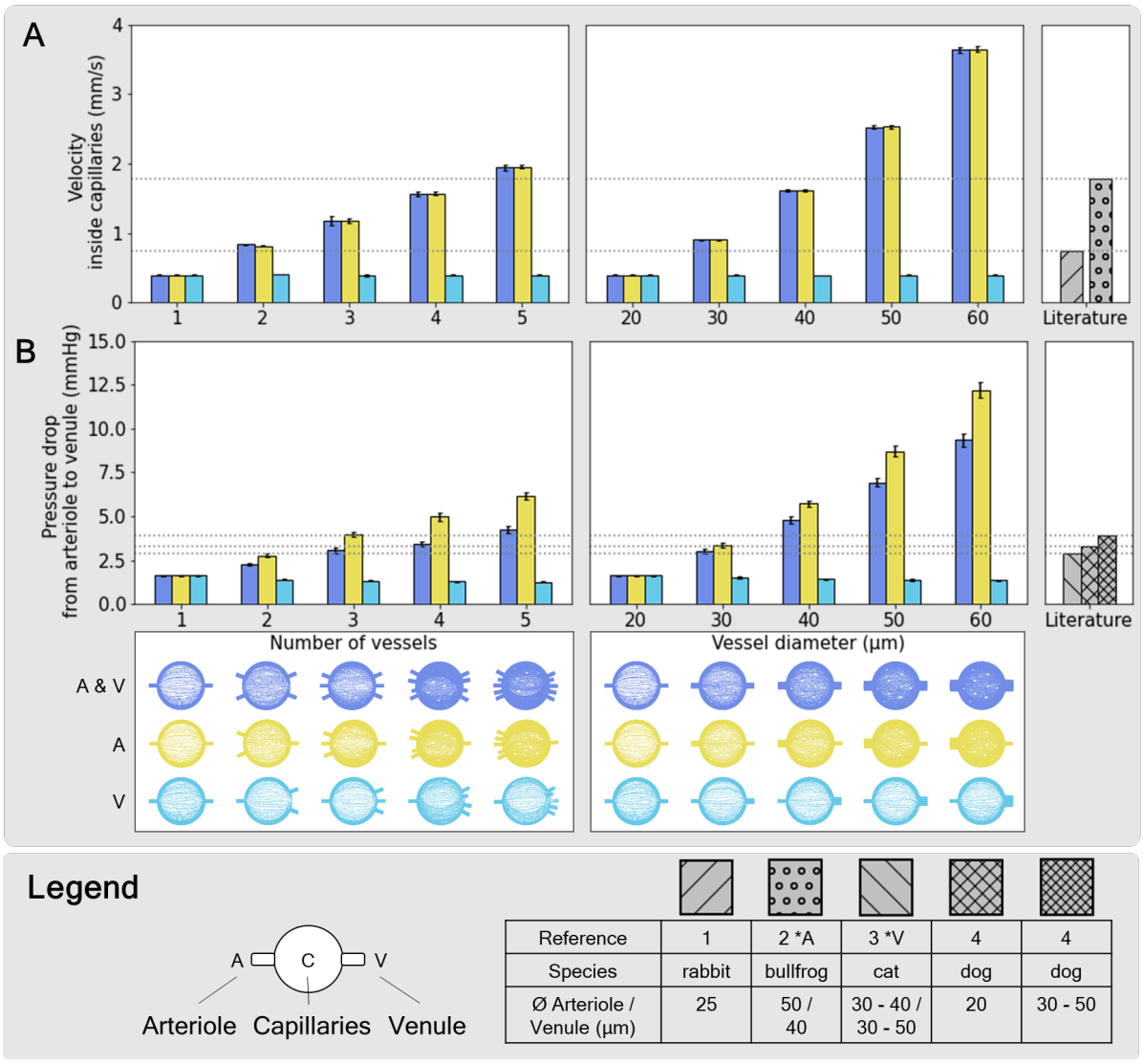

Reference	1	2 *A	3 *V	4	4
Species	rabbit	bullfrog	cat	dog	dog
Ø Arteriole / Venule (µm)	25	50 / 40	30 - 40 / 30 - 50	20	30 - 50

Figure 3.9: Results from blood flow simulations in our connectivity models were compared with reference values from the literature. Computational fluid dynamics simulations were performed with a Newtonian viscosity model. The alveolar capillary network models were linked to varying numbers (left panels) or diameters (right panels) of arterioles (yellow), venules (turquoise), or both (blue). Measurements of capillary flow velocity (A) and of arteriole-to-venule pressure drop (B) were juxtaposed with respective literature values of [1]rabbit (Schlosser et al., 1965), [2]bullfrog (Horimoto et al., 1979), [3]cat (Nagasaka et al., 1984) and [4]dog (Bhattacharya and Staub, 1980). *A The inlet velocity boundary condition at the arterioles in the simulation were chosen based on a value from this publication. *V The outlet pressure boundary condition at the venules in the simulation was chosen based on a value from this publication.

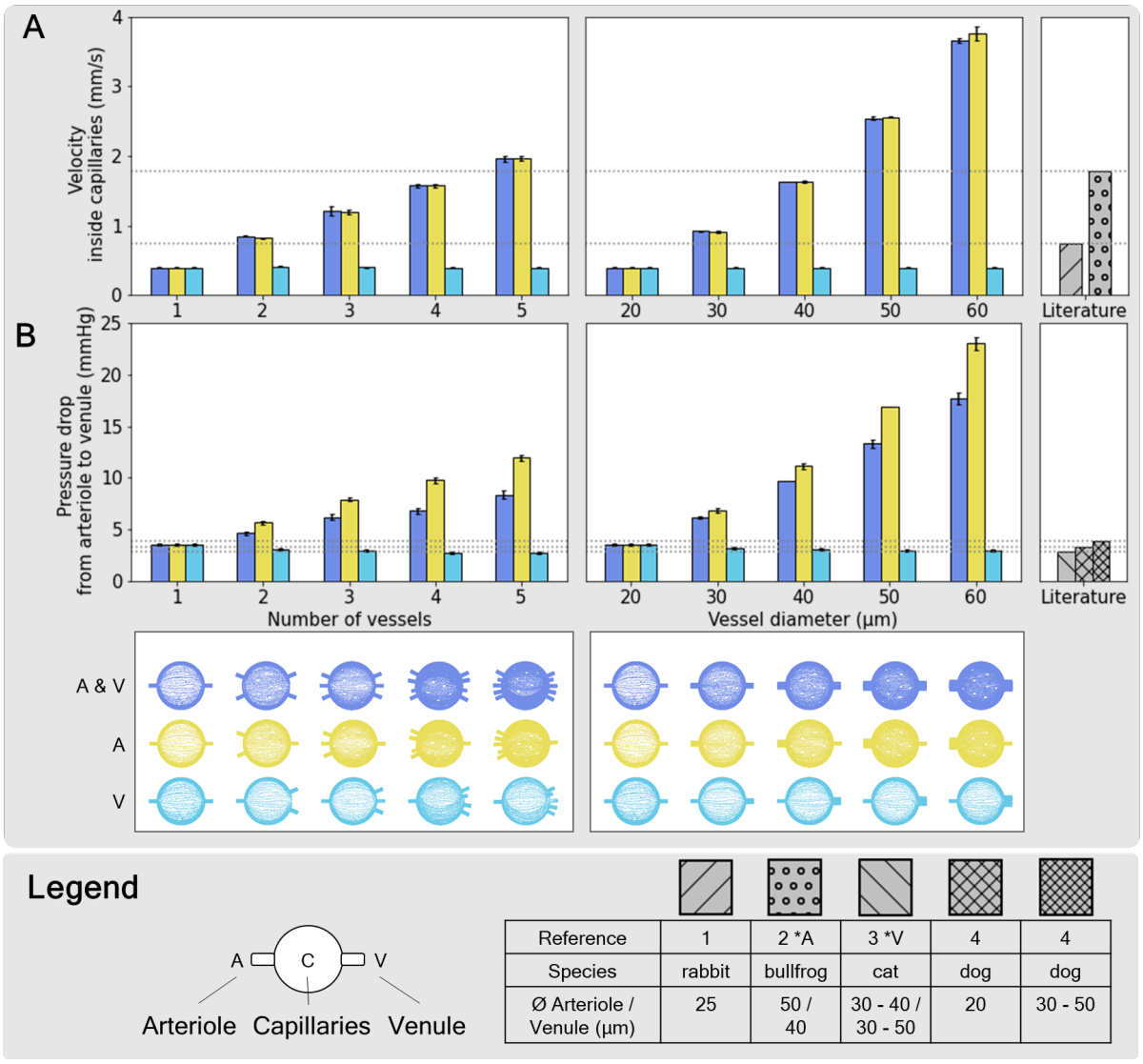

Reference	1	2 *A	3 *V	4	4
Species	rabbit	bullfrog	cat	dog	dog
Ø Arteriole / Venule (µm)	25	50 / 40	30 - 40 / 30 - 50	20	30 - 50

Figure 3.10: Results from blood flow simulations in our connectivity models were compared with reference values from the literature. Computational fluid dynamics simulations were performed with a non-Newtonian viscosity model. The alveolar capillary network models were linked to varying numbers (left panels) or diameters (right panels) of arterioles (yellow), venules (turquoise), or both (blue). Measurements of capillary flow velocity (A) and of arteriole-to-venule pressure drop (B) were juxtaposed with respective literature values of [1]rabbit (Schlosser et al., 1965), [2]bullfrog (Horimoto et al., 1979), [3]cat (Nagasaka et al., 1984) and [4]dog (Bhattacharya and Staub, 1980). *A The inlet velocity boundary condition at the arterioles in the simulation were chosen based on a value from this publication. *V The outlet pressure boundary condition at the venules in the simulation was chosen based on a value from this publication.

3.5.3 Inference of connection of the ACN to arterioles from physiological measurements.

The experimental data to which we compared our simulation results of the connectivity analyses constitute a limitation. They were taken from different studies in different species.

In the next step, we highlight the potential of our approach if consistent data sets were available. We demonstrate how quantitative insight into arteriole and venule configurations can be derived from blood flow parameters.

To quantify the relationship between capillary velocity and pressure drop with the volume of arterioles in our models, we performed regression analyses (Figure 3.11). The regression lines for capillary velocity overlap to such an extent that distinctions between different model sets, representing symmetric or asymmetric variation of number of diameter of vessels, become imperceptible. In contrast, the pressure drop regression lines show distinct variations. Equipped with these analyses, we intend to predict the volume of arterioles from a pair of sample values. For lack of corresponding experimental measurements, we have opted for values from our simulation results. Consider a capillary flow velocity of 1.56 mm/s and a pressure drop of 3.44 mmHg, as predicted within the model with four arterioles and four venules. Using the regressions, one can assign this velocity to models with an arteriolar volume of roughly 50000 μm^3, which corresponds to models with single 40-µm-diameter vessels or models with four 20-µm-diameter vessels (Figure 3.11 A).

Following the same procedure with the pressure drop value, we obtained different arterial volumes from the distinct regression lines (Figure 3.11 B). The regression of the symmetrical model set with variations in the number of vessels indicates a volume of 48000 μm^3, which is closest to four vessels and aligns with the results from velocity regression. According to the other regression lines, this pressure drop value could also be found in models with arteriolar volume less than 40000 μm^3, for example in models with a 30-µm-arteriole and a 20-µm-venule. However, these models can be ruled out because they do not fit the velocity regression analysis.

In essence, we could use capillary flow velocity to deduce the arteriolar volume. The pressure drop analysis gave us additional insights into possible configurations of arterioles and venules. By combining these findings, we could identify the model geometry associated with this pair of values. We conducted similar analyses with various pairs of values and usually found two plausible connectivity configurations in terms of vessel diameter and number (supplementary Figure S.3). In this way, we could make unique or dichotomous predictions about the number and / or diameter of vessels connected to the ACN around an alveolus if experimental measurements on capillary flow velocity and pressure drop from arteriole to venule were available to us.

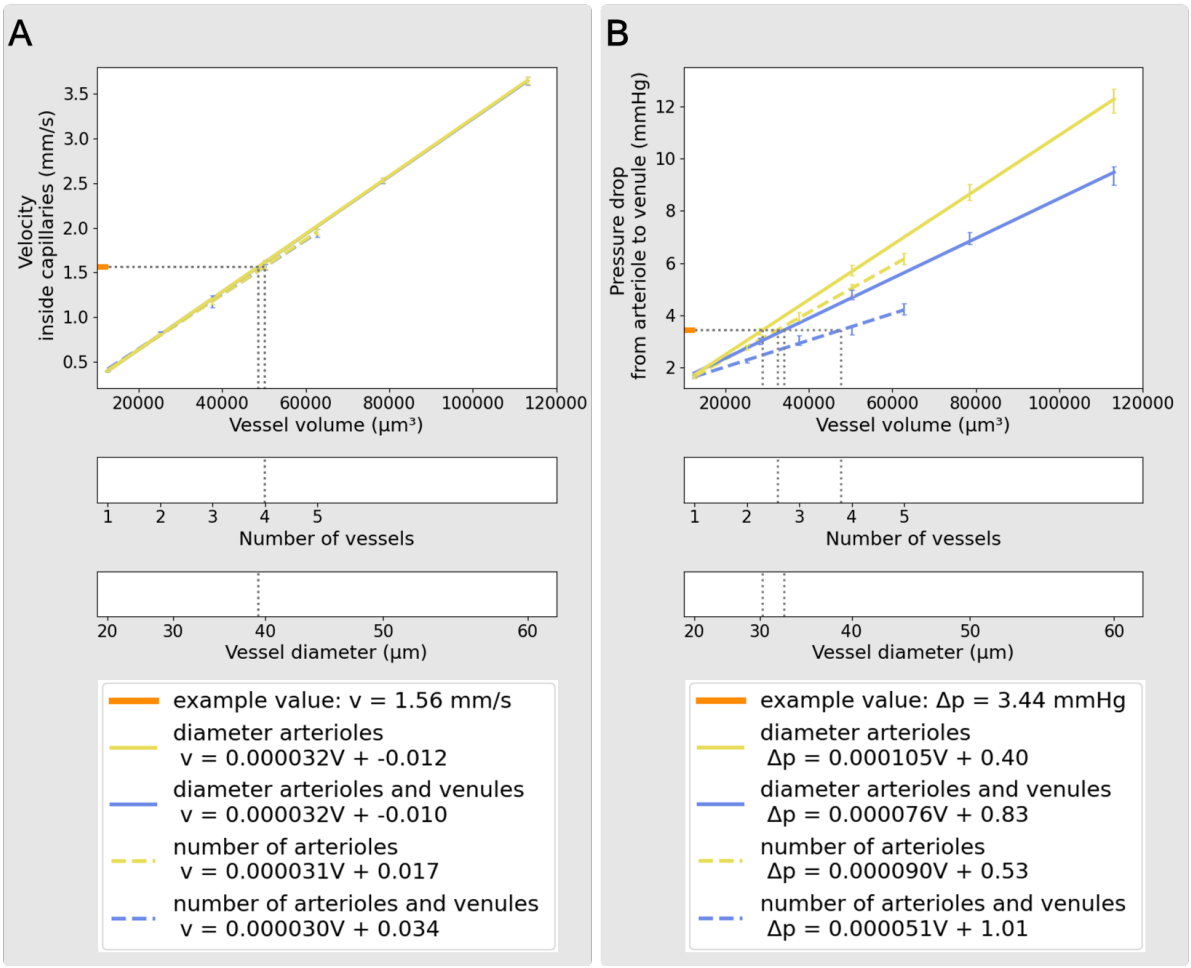

Figure 3.11: Inference of vessel arrangement from flow velocity and pressure drop. The simulation results from a model with each four arterioles and venules were chosen as an example pair of values (orange). Regression analyses yielded quantitative relationships between the target values and the arrangement of arterioles and venules in our models. These arrangements comprise variations in the number (dashed) or diameter (continuous) of solely arterioles (yellow) or both arterioles and venules (blue). A) In terms of the mean flow velocity within capillaries, the regression curves for the different model geometries overlap. B) The regression curves for pressure drop of the different model types are distiguishable. Simulations were performed with a Newtonian viscosity model.

3.6 Refined estimation of gas exchange efficiency in *Alvin*

We return to our integrative *in silico* model of gas exchange in the alveolus. How do the differences in capillary blood flow dynamics we observed in our connectivity analyses affect gas exchange efficiency? Parameter settings in *Alvin* were revisited with the knowledge gained from 3D morphological modeling (Figure 3.12 A). Specifically, the capillary

volume was set to 712.000 µm^3 and the surface area available for gas exchange was set to 111.300 µm^2 (Table 3.3). Further, the velocity parameter in *Alvin* was adjusted to the CFD results for the mean capillary velocity in each case. The simulation results showed that oxygen saturation reached an equilibrium early during blood transit along the capillary. To quantify the efficiency of gas exchange, we analyzed two output parameters in *Alvin*: DLO_2 (Figure 3.12 B) and the reaction half-time normalized to transit time (t_{half} / $t_{transit}$, Figure 3.12 C). For better comparability, this value was normalized to the total transit time. At a blood flow velocity of 0.4 mm/s, which was measured in our default model, we obtain a DLO_2 of 95.3 ml/(mmHg·min) and a normalized reaction half-time of 0.03 in *Alvin*. As the number or diameter of connected arterioles rises, and with it the blood flow velocity within capillaries, both output parameters also increase. DLO_2 increases quadratically with the arterial number (n) or diameter (d) according to $DLO_2 = a\cdot(n|d)^2 + b\cdot(n|d) + c$ (supplementary Figure S.4). For the normalized reaction half-time, this occurs linearly (supplementary Figure S.5).

In conclusion, an increase in blood flow velocity in the alveolar capillaries had a positive effect on oxygen diffusion capacity. Although the reaction half-time was reached ever later as the blood flow increased, it remained within the first quarter of the total transit time.

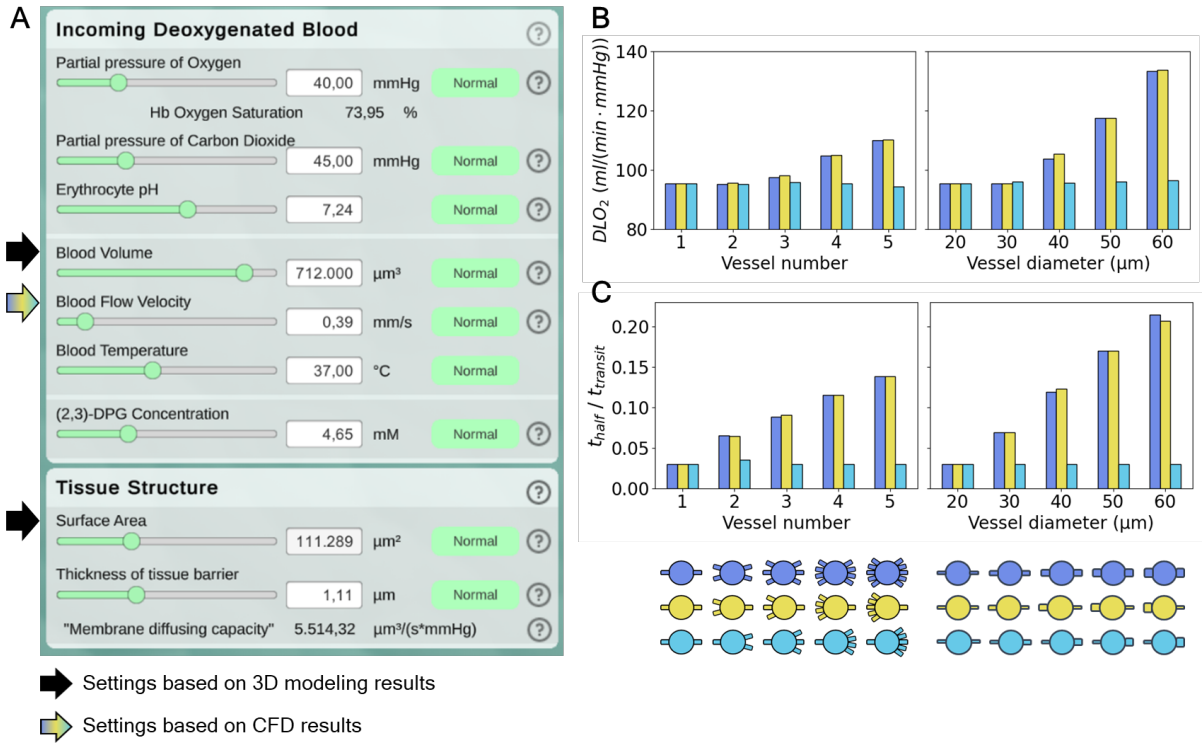

Figure 3.12: Variations in blood flow impact the results of gas exchange simulations in *Alvin*. A) Parameter settings in *Alvin* were revisited with the knowledge gained from 3D morphological modeling (black arrows) and CFD simulations (colored arrow). The blood volume was set to the volume of our sheet-flow *Alveolus*$_V$ ACN model. The value for surface area was chosen according to the surface area available for gas exchange on our sheet-flow *Alveolus*$_V$ ACN model. The blood flow velocity within capillaries was adjusted based on the CFD results from the different connectivity models (blue, yellow and turquoise). From the gas exchange simulations in *Alvin*, the following output parameters were analyzed : B) Pulmonary diffusion capacity for oxygen ($D_{L_{O_2}}$) and C) reaction half time normalized to transit time (t_{half} / $t_{transit}$). Reaction half time is the time point at which 50% of the oxygenation that blood undergoes during its transit along the alveolus is completed.

Chapter 4

Discussion

The main objective of this study was to characterize and differentiate the influences of various morphological and physiological factors on the process of gas exchange in the human alveolus. To this end, the first crucial step involved the development of a suitable mathematical model for calculating gas exchange within the alveolar micro-environment.

4.1 An integrative, spatio-temporal model of alveolar gas exchange

We successfully combined existing mathematical models of different processes of gas exchange (Weibel et al., 1993; Dash et al., 2016). The model describes the entire transport process of oxygen from the air to the hemoglobin in the blood. The previous models, that we have adapted and adopted, have described the individual processes as stationary states. In our integrative model, however, these processes are coupled in such a way that a spatio-temporal resolution is achieved. This temporal resolution is a significant advancement in our model, providing valuable insights into the gas exchange process (Sapoval et al., 2020). It allows us to calculate the diffusion gradient and changes in oxygen saturation along the erythrocyte flow direction within the capillary. With a constant velocity along the capillary, we can use the transit time of an erythrocyte to determine its position within the capillary, and vice versa. Further, the temporal resolution enabled us to derive additional physiological parameters. For instance, the reaction half-time was determined for validation purposes. The reaction half-time of 40 ms obtained from our model closely approximated the experimentally measured value of 37 ms in mice (Tabuchi et al., 2013). In the same study, the authors have argued that gas exchange commences in the terminal arterioles - a consideration not taken into account in our theoretical estimate. Our model solely focuses on processes in the alveolar capillary network. Consequently, it is reasonable to assume that our value likely underestimates the *in vivo* reaction half-time in humans.

In summary, we have created a spatio-temporal mathematical model of the complete transport of oxygen from alveolar air into the blood and erythrocytes and its binding to hemoglobin. The spatio-temporal resolution was an essential feature of our model and a prerequisite for its use at the core of our interactive simulation software *Alvin*.

4.2 The simulation software *Alvin* enables interactive exploration of the underlying mathematical model

The interactive simulation software *Alvin* represents a progressive approach to making theoretical models accessible. It is designed to enable exploration of the influence of individual factors on gas exchange and thus to reveal the underlying intricate relationships. The decisive factor for this is allowing the user to configure model parameters. Parameter value changes lead to an immediate response that can be observed both qualitatively through the 3D visualisation and quantitatively through dynamic graphs. The system further illuminates interdependencies within the model by visually highlighting components of the 3D model associated to the currently selected parameters. A key strength of the application is its ability to run and compare multiple simulation instances simultaneously.

Alvin's versatility was demonstrated in both educational and research context. The application was successfully integrated into a university level lab course. By working on tasks with the help of *Alvin*, a deeper understanding of the complex intricacies of gas exchange, including well-known phenomena like the Bohr effect (Riggs, 1988), were to be conveyed. The interactive nature of *Alvin* was highly regarded by course participants, evident from their responses in post-course surveys. To establish a quantitative assessment of usability and aesthetics, a comparative study with *Alvin* and similar systems would be necessary, although initial results of the standardized QUESI and VISAWI questionnaires suggest that the students found its use appealing and relatively intuitive.

Alvin also serves as a valuable tool for examining published data. For instance, Kulish (2006) have estimated DLO_2 as a function of blood flow. We found that we could only replicate their results by considering additional dependencies on surface area. Kulish's estimations were grounded in physiological measurements. While invaluable, such measurements in living organisms present challenges, as it is difficult to ensure the observation solely reflects the impact of a single variable (in this case, blood flow) on the measured value. It is possible that other factors, such as changes in surface area, also play a role. In *Alvin*, all model parameters can be configured individually, providing a more nuanced analysis.

While existing interactive approaches (Winkler et al., 1995; Kapitan, 2008) have focused on the distribution of ventilation and perfusion ratios affecting gas exchange at a higher organ

level, *Alvin* delves into the alveolar level of gas exchange. The ability to analyze multiple simulation instances concurrently sets our approach apart from previous simulations. In summary, *Alvin* serves as an interactive platform for investigating the gas exchange process on an alveolar level. It can be employed in advanced university teaching and as a tool for interpreting and complementing published data.
So far, the values for the model parameters were chosen based on individual reference values from the literature. An objective of this work was to characterize these parameters more precisely and to take into account their interdependencies. We began by modeling the morphology of the alveolar capillary network in detail and based on data.

4.3 Comprehensive modeling of the human alveolar capillary network morphology: Navigating interdependencies in stereological data

We obtained the 3D geometry of the ACN using a data-driven sheet-flow model. Our modeling approach relied on the existing literature, incorporating a 3/4 spheroid shape for the alveolar base (Hansen and Ampaya, 1975) and considering sheet-flow (Fung and Sobin, 1969) and tube-flow (Mühlfeld et al., 2010) geometries for the ACN. To ensure accurate scaling, our models were based on stereological measurements. However, we observed that the combination of these assumptions and parameters did not always align, for example concerning alveolar base diameter and volume. In sum, our ACN models exhibited smaller volumes and surface areas compared to values reported in the literature, with sheet-flow models showing a better fit than tube-flow models.
Minor discrepancies in data were anticipated. Our modeling parameters were collated from measurements across different studies, which employed various fixation methods such as airway instillation (Hansen and Ampaya, 1975; Ochs et al., 2004; Kawakami and Takizawa, 1987; Stone et al., 1992; Mühlfeld et al., 2010; Gehr et al., 1978), vascular perfusion of fixative (Mercer et al., 1994), or other techniques (Toshima et al., 2004; Matsuda et al., 1987). Besides potential measurement inaccuracies, it is necessary to acknowledge further biases and information loss associated with tissue fixation. Additionally, assuming the alveolus corresponds to a 3/4 spheroid is a simplification.
Although these limitations exist, the experimental data is invaluable and so far the only source available. Nevertheless, we advocate that the parameters used to characterize alveolar morphology should not be considered in isolation.
By integrating stereological data from multiple studies, our comprehensive approach to understanding ACN morphology extends beyond parameter measurements, taking into account the interdependencies among various variables. This is important since ACN geom-

etry plays a critical role in gas exchange function, influencing the volume of blood that can flow through alveolar tissue and the available surface area for diffusion.

4.4 Blood flow dynamics in the alveolar capillary network: A comparative CFD study on Newtonian and non-Newtonian viscosity models

Blood flow dynamics in the alveolar region are crucial for understanding gas exchange efficiency. In this study, we employed CFD simulations to predict blood flow in our ACN geometry, comparing results between Newtonian and non-Newtonian viscosity models.
The simulations showed that, in both viscosity models, flow velocity in the capillaries was notably lower than in arterioles and venules, averaging around 0.4 mm/s. However, the drop from inlet to outlet differed substantially between the two models, with the non-Newtonian model resulting in more than double the pressure drop (3.54 mmHg) compared to the Newtonian model (1.64 mmHg). To contextualize these findings, we compared them to existing data. With their *in vitro* sheet-flow model, Stauber et al. (2017) have observed a flow velocity of 0.3 mm/s at a 7 µm interpillar distance and a 3.75 mmHg pressure drop. Burrowes et al. (2004) have developed a tube-flow model of blood flow in the capillaries of several interconnected alveoli. At a pressure drop of 5.88 mmHg and different transmural pressures, transit times have been measured from which flow velocities between 0.15 mm/s and 1.07 mm/s could be derived. Zurita and Hurtado (2022) have simulated blood flow in a simplified geometry of the murine capillary bed. At a pressure drop of 3 mmHg, they have observed a velocity distribution between 0.07 mm/s and 0.36 mm/s. As such, the mean flow velocity we measured in the capillaries agrees well with the literature. The same applies to the pressure drop in our simulations with non-Newtonian fluid.
Notably, our sensitivity analyses revealed a linear relationship between pressure drop and fluid viscosity. The selection of the Newtonian and Carreau viscosity models was deliberate, with the former reflecting a realistic value for apparent viscosity in pulmonary capillaries (Fung, 1984; Kiani and Hudetz, 1991; Fung, 1997; Grotberg and Romanò, 2023), while the latter accounts for non-Newtonian properties, despite higher potential viscosity values.
In order to validate our CFD model, including the viscosity model, we need a suitable set of experimental data. The experimental data available to us so far comes from various studies carried out on different species. To further complicate matters, the measurements were carried out on vessels with different diameters. A consistent data set would be necessary for the selection of our boundary conditions and as a benchmark for comparing the simulation results. Ideally, this should come from the same experiment, or at least from the same species. It should contain the flow velocities in arterioles and capillaries, the blood pressure

in arterioles and venules and the mean diameters of these vessels.
In summary, we have successfully simulated the blood flow in our alveolar capillaries. Our results align with existing literature but emphasize the substantial impact of viscosity models on pressure drop. In order to validate the CFD model, a coherent set of experimental data is required.

4.5 A novel perspective on structure-function relationships in the pulmonary vasculature

Our approach of 3D modeling coupled with CFD simulations provides a means to quantify the influence of morphological variations of blood flow dynamics in the ACN. Consequently, it can be used to investigate structural details such as the connectivity of the ACN with the vascular tree using physiological indices. Comparison of our connectivity analysis with the literature revealed either consistent or contradictory evidence for the configuration of arterioles and venules. This depended on whether the simulations were performed with Newtonian or non-Newtonian viscosity models. Consistent experimental data are needed to identify realistic connectivity configurations.
Our research involves systematically altering the number and diameter of arterioles and venules connected to the ACN model, thereby introducing morphological variations. The results of the CFD simulations in these connection models were juxtaposed and compared with literature values. The behavior of the simulation results, as these variations were introduced, can be explained by the continuity equation (Equation 2.5), which is fundamentally dependent on the total mass flow within the system. In our simulations, the latter is defined as the velocity at the inlet and therefore depends linearly on the inlet surface area. The linear or non-linear increase in the target values in CFD simulations in our connectivity models is therefore a direct consequence of the linear or non-linear increase in the total inlet surface area.
Overall, our simulation results across different model geometries fell within the range of the published reference values for different species (Schlosser et al., 1965; Horimoto et al., 1979; Nagasaka et al., 1984; Bhattacharya and Staub, 1980). When comparing velocity values, we concluded that the ACN of an alveolus must be connected to at least two arterioles with a diameter of 20 µm or to an arteriole with a diameter of at least 30 µm. The pressure drop results from simulations with the Newtonian viscosity model confirmed this conclusion. Conversely, simulations with the non-Newtonian viscosity model indicated that the ACN of a single alveolus is not associated with more than a single arteriole of 20 µm.
In morphological studies, the classification of the terminal arterioles varies slightly (Huang et al., 1996; Pump, 1966; Horsfield, 1978). In order to compare the findings of these publi-

cations, the vessel diameter must be taken into account. All studies indicate that an arteriole with a 20 µm diameter is connected to the ACN of multiple alveoli, with the specific number ranging from 4.8 (Huang et al., 1996) to 24 (Horsfield, 1978). Based on these observations, one could assume that simulations with a single arteriole of 20 µm would result in excessively high blood flow indices. Yet, our findings did not align with this assumption, underscoring the need for experimental data to resolve this discrepancy. With an appropriate experimental data set, regression analyses of the simulation results could be used to identify the connectivity configurations that most closely correspond to reality. Based on physiological indices, conclusions are thus drawn about structural details of the morphology. This approach represents a departure from previous *in silico* models for simulating blood flow in the pulmonary vasculature, which typically rely on the most accurate morphological representation possible to make predictions about function, such as blood flow dynamics (Clark et al., 2010, 2011; Clark and Tawhai, 2018; Ebrahimi et al., 2022). The inverse approach on structure-function-relationships, as we have proposed it, has so far only been pursued on a cellular level. Chen et al. (2021, 2023) have inferred the position and morphology of neurons from *in vivo* extracellular voltage recordings using biophysical modeling.

This novel strategy can be transferred to other tissues and organs. It contributes to the field of computational biology by shifting the perspective and potential insights gained by emphasizing the connection between structural configuration and functional outcomes.

4.6 Deciphering the influences on gas exchange: Insights from 3D modeling and simulations of blood flow and gas exchange in the human alveolus

By combining the findings of our study, we could characterize the impact of morphological and physiological parameters at the alveolar level on gas exchange. The results show that our alveolar model captures 50% of the discrepancy between the physiological and morphological estimates of DLO_2. Furthermore, they confirm that, under normal circumstances, the gas exchange process is not diffusion-limited.

By integrating the outcomes of our 3D modeling and blood flow simulations in *Alvin*, we can predict DLO_2, accounting for prevailing structural and functional influences in the alveolus. This encompasses factors such as the available surface area for gas exchange and the volume and flow velocity of capillary blood. For our default connectivity model, we calculated a DLO_2 of 95.3 ml/(mmHg·min). This value falls right in the middle between the physiological estimate of 30 ml/(mmHg·min) (Hsia et al., 2016) and the morphological estimate of 158 ml/(mmHg·min) (Weibel, 2009). This signifies that factors related to

alveolar-level processes and structures account for half of the discrepancy between the physiological and morphological estimates of DLO_2. The remaining half is likely caused by factors associated with higher-level processes such as ventilation to perfusion mismatch or with non-pulmonary processes of oxygen transport (Hsia, 2002).
The potential limiting factors at the alveolar level can be further dissected. Under normal conditions, the partial pressures of respiratory gases reach equilibrium early during blood transit through the alveolar zone (West, 2012). Our results align with this observation, showing that even at higher blood flow velocities, the reaction half-time remains within the first quarter of the transit time, highlighting blood flow as the limiting factor for oxygen uptake. If the reaction were diffusion-limited, the respiratory gases would not reach equilibrium by the end of transit.
In summary, our model can predict the course of gas exchange resulting from the joint influence of various morphological and physiological parameters under normal conditions. Previous computational approaches have directly coupled calculations of ventilation and gas exchange (Hofemeier et al., 2016), of perfusion and gas exchange (Zurita and Hurtado, 2022) or even of ventilation, gas exchange and perfusion (Ben-Tal, 2006; Foy and Kay, 2019; Si and Xi, 2022) in their simulations. In contrast, we manually integrate intermediate results in *Alvin*. However, the unique selling points of our approach lie in the morphological detail of our model and the accessibility of the gas exchange simulation gained through interactivity.

4.7 Conclusion and outlook

In this study, we addressed the question of how morphological and physiological characteristics influence gas exchange in the human alveolus both collectively and individually. Using 3D geometric modeling and blood flow simulations, we characterized key parameters. The interactive features within *Alvin*'s gas exchange simulation provide an ideal opportunity to explore the individual influences of different model parameters on gas exchange.
A major challenge for our approach is the lack of suitable experimental data, specifically a coherent data set comprising flow velocities in arterioles and capillaries, blood pressure in arterioles and venules and the mean diameters of these vessels. This data is required for the selection of boundary conditions and validation of our blood flow simulations. The sensitivity analyses revealed that the simulation results strongly depended on the inlet velocity and the fluid viscosity. In the absence of experimental data meeting the desired requirements, a temporary solution to identify an appropriate viscosity model could involve leveraging the data provided by Stauber et al. (2017). A comparative analysis of various viscosity models should be undertaken to pinpoint the most suitable one for the physiological problem (Krivovichev, 2022; Abbasian et al., 2020). Beyond classical models like the

Carreau model, our exploration should encompass such that are designed for microvessel flow. Yen and Fung (1973) and Secomb (2011) have introduced models that consider the dependence of apparent viscosity on hematocrit and sheet thickness - factors that play major roles in capillary flow (Burrowes et al., 2004).

One of the strengths of our work lies in the morphological detail of our 3D model. In order to exploit this further, it would be beneficial to refine the spatial resolution of our gas exchange simulation in the future. To achieve this, we would integrate oxygen diffusion and transport calculations directly into the blood flow simulations, following the example of Foy and Kay (2019), Zurita and Hurtado (2022) and Si and Xi (2022). The Ansys software offers the necessary functionalities to realize this. The diffusion of gases according to Fick's law would be implemented as a boundary condition on the capillary wall and gas transport within the blood would be simulated using additional species. With this nuanced spatial resolution of oxygen transport in the 3D model, our approach could then also be used to study the gas exchange process under pathological conditions, such as those present in pulmonary fibrosis. This includes deformations of the capillaries which affect the size and number of pillars and the surface area of the capillaries (Schraufnagel et al., 1986).

Furthermore, we could consider the dependence of alveolar morphology on pressure differences during a respiratory cycle. The alveolar microvasculature is very delicate and elastic, undergoing deformation based on variations in transmural pressure, the pressure difference between alveolus and capillary (West, 2012). Fung and Sobin (1972) and Sobin et al. (1972) have established the relationship between transmural pressure and capillary sheet thickness based on measurements in the cat. Leveraging Ansys' capability for dynamic mesh simulation, this relation could be included in our model to study the effects of breathing dynamics on gas exchange. Si and Xi (2022) have shown that different breathing depths have a notable influence on blood flow dynamics in the alveolar capillaries. It would therefore be of great interest to investigate the effects of altered breathing dynamics as they prevail under pathological conditions that are accompanied by aberrations in alveolar- (COPD, asthma, ARDS, mechanical ventilation) or vascular pressure (pulmonary arterial hypertension).

In summary, our methodology holds immense potential to contribute to the broader field of respiratory research, providing a nuanced exploration of the structural and functional intricacies that govern the process of gas exchange in the human alveolus.

Bibliography

Majid Abbasian, Mehrzad Shams, Ziba Valizadeh, Abouzar Moshfegh, Ashkan Javadzadegan, and Shaokoon Cheng. Effects of different non-Newtonian models on unsteady blood flow hemodynamics in patient-specific arterial models with in-vivo validation. *Computer Methods and Programs in Biomedicine*, 186:105185, April 2020. ISSN 0169-2607.

Carlos Albors, Andy L. Olivares, Xavier Iriart, Hubert Cochet, Jordi Mill, and Oscar Camara. Impact of Blood Rheological Strategies on the Optimization of Patient-Specific LAAO Configurations for Thrombus Assessment. In Olivier Bernard, Patrick Clarysse, Nicolas Duchateau, Jacques Ohayon, and Magalie Viallon, editors, *Functional Imaging and Modeling of the Heart*, Lecture Notes in Computer Science, pages 485–494, Cham, 2023. Springer Nature Switzerland. ISBN 978-3-031-35302-4.

Inc. ANSYS. 1.2 Continuity and Momentum Equations. In *Ansys® Fluent Theory Guide*, Release 12.0. Release 12.0 edition, January 2009a.

Inc. ANSYS. 18. Solver Theory. In *Ansys® Fluent Theory Guide*, Release 12.0 ©. January 2009b.

Inc. ANSYS. 26.13 Monitoring Solution Convergence. In *Ansys® Fluent Theory Guide*, Release 12.0 ©. January 2009c.

Inc. ANSYS. 6.2 Mesh Requirements and Considerations. In *ANSYS FLUENT User's Guide*, Release 12.0 ©. January 2009d.

Inc. ANSYS. Ansys® Academic Research CFD, 2022.

H. Bachofen, S. Schurch, M. Urbinelli, and E. R. Weibel. Relations among alveolar surface tension, surface area, volume, and recoil pressure. *Journal of Applied Physiology*, 62(5): 1878–1887, May 1987. ISSN 8750-7587.

Alona Ben-Tal. Simplified models for gas exchange in the human lungs. *Journal of Theoretical Biology*, 238(2):474–495, January 2006. ISSN 0022-5193.

J. Bhattacharya and N. C. Staub. Direct Measurement of Microvascular Pressures in the Isolated Perfused Dog Lung. *Science*, 210(4467):327–328, October 1980.

R. Byron Bird, Warren E. Stewart, and Edwin N. Lightfoot. *Transport Phenomena*. John Wiley & Sons, December 2006. ISBN 978-0-470-11539-8.

S. Braber, K. a. T. Verheijden, P. a. J. Henricks, A. D. Kraneveld, and G. Folkerts. A comparison of fixation methods on lung morphology in a murine model of emphysema. *American Journal of Physiology-Lung Cellular and Molecular Physiology*, 299(6):L843–L851, December 2010. ISSN 1040-0605.

Tobias Buchacker, Christian Mühlfeld, Christoph Wrede, Willi L. Wagner, Richard Beare, Matt McCormick, and Roman Grothausmann. Assessment of the Alveolar Capillary Network in the Postnatal Mouse Lung in 3D Using Serial Block-Face Scanning Electron Microscopy. *Frontiers in Physiology*, 10, 2019. ISSN 1664-042X.

Kelly S. Burrowes, Merryn H. Tawhai, and Peter J. Hunter. Modeling RBC and Neutrophil Distribution Through an Anatomically Based Pulmonary Capillary Network. *Annals of Biomedical Engineering*, 32(4):585–595, April 2004. ISSN 1573-9686.

Pierre J. Carreau. Rheological Equations from Molecular Network Theories. *Transactions of The Society of Rheology*, 16(1):99–127, March 1972. ISSN 0038-0032.

Ziao Chen, Dan Dopp, Satish S Nair, and Drew B Headley. Inferring Morphology of a Neuron from In Vivo LFP Data. In *2021 10th International IEEE/EMBS Conference on Neural Engineering (NER)*, pages 774–777, May 2021.

Ziao Chen, Matthew Carroll, and Satish S. Nair. Inferring Pyramidal Neuron Morphology using EAP Data. *International IEEE/EMBS Conference on Neural Engineering: [proceedings]. International IEEE EMBS Conference on Neural Engineering*, 2023, April 2023. ISSN 1948-3546.

A. R. Clark and M. H. Tawhai. TEMPORAL AND SPATIAL HETEROGENEITY IN PULMONARY PERFUSION: A MATHEMATICAL MODEL TO PREDICT INTERACTIONS BETWEEN MACRO- AND MICRO-VESSELS IN HEALTH AND DISEASE. *The ANZIAM Journal*, 59(4):562–580, April 2018. ISSN 1446-1811, 1446-8735.

A. R. Clark, K. S. Burrowes, and M. H. Tawhai. Contribution of serial and parallel microperfusion to spatial variability in pulmonary inter- and intra-acinar blood flow. *Journal of Applied Physiology*, 108(5):1116–1126, May 2010. ISSN 8750-7587.

A. R. Clark, M. H. Tawhai, E. A. Hoffman, and K. S. Burrowes. The interdependent contributions of gravitational and structural features to perfusion distribution in a multiscale

model of the pulmonary circulation. *Journal of Applied Physiology*, 110(4):943–955, April 2011. ISSN 8750-7587.

James D. Crapo and Robert O. Crapo. Comparison of total lung diffusion capacity and the membrane component of diffusion capacity as determined by physiologic and morphometric techniques. *Respiration Physiology*, 51(2):183–194, February 1983. ISSN 0034-5687.

Ranjan K. Dash and James B. Bassingthwaighte. Erratum to: Blood HbO2 and HbCO2 dissociation curves at varied O2, CO2, pH, 2,3-DPG and temperature levels. *Annals of Biomedical Engineering*, 38(4):1683–1701, April 2010. ISSN 1573-9686.

Ranjan K. Dash, Ben Korman, and James B. Bassingthwaighte. Simple Accurate Mathematical Models of Blood HbO2 and HbCO2 Dissociation Curves at Varied Physiological Conditions–Evaluation and Comparison with other Models. *European journal of applied physiology*, 116(1):97–113, January 2016. ISSN 1439-6319.

T.L. Davis and R.G. Mark. Teaching physiology through simulation of hemodynamics. In *[1990] Proceedings Computers in Cardiology*, pages 649–652, September 1990.

David G. Dewhurst, Guy J. Brown, and Anthony S. Meehan. Microcomputer Simulations of Laboratory Experiments in Physiology. *Alternatives to Laboratory Animals*, 15(4):280–289, June 1988. ISSN 0261-1929.

Xiaohua Du, Xia Liu, and James Blackar Mawolo. The Architecture of Alveolar Capillaries in the Lungs of Bactrian Camels (Camelus bactrianus). *International Journal of Morphology*, 38(6):1779–1785, December 2020. ISSN 0717-9502.

Behdad Shaarbaf Ebrahimi, Haribalan Kumar, Merryn H. Tawhai, Kelly S. Burrowes, Eric A. Hoffman, and Alys R. Clark. Simulating Multi-Scale Pulmonary Vascular Function by Coupling Computational Fluid Dynamics With an Anatomic Network Model. *Frontiers in Network Physiology*, 2:867551, April 2022. ISSN 2674-0109.

Joel H. Ferziger, Milovan Perić, and Robert L. Street. *Numerische Strömungsmechanik*. Springer, Berlin, Heidelberg, 2020. ISBN 978-3-662-46543-1 978-3-662-46544-8.

Adolf Fick. Ueber Diffusion. *Annalen der Physik*, 170(1):59–86, 1855. ISSN 1521-3889.

C. Alberto Figueroa, Irene E. Vignon-Clementel, Kenneth E. Jansen, Thomas J. R. Hughes, and Charles A. Taylor. A coupled momentum method for modeling blood flow in three-dimensional deformable arteries. *Computer Methods in Applied Mechanics and Engineering*, 195(41):5685–5706, August 2006. ISSN 0045-7825.

R. E. Forster. Diffusion of Gases. In *Handbook of Physiology*, pages 839–872. Waverly Press, 1964.

Brody H. Foy and David Kay. A computationally tractable scheme for simulation of the human pulmonary system. *Journal of Computational Physics*, 388:371–393, July 2019. ISSN 0021-9991.

Y. C. Fung. Microcirculation. In Y. C. Fung, editor, *Biodynamics: Circulation*, pages 224–289. Springer, New York, NY, 1984. ISBN 978-1-4757-3884-1.

Y. C. Fung. Circulation. In *Biomechanics*, pages XVIII, 572. Springer New York, 2 edition, 1997.

Y C Fung and S S Sobin. Theory of sheet flow in lung alveoli. *Journal of Applied Physiology*, 26(4):472–488, April 1969. ISSN 8750-7587.

Y. C. Fung and S. S. Sobin. Elasticity of the Pulmonary Alveolar Sheet. *Circulation Research*, 30(4):451–469, April 1972.

Peter Gehr, Marianne Bachofen, and Ewald R. Weibel. The normal human lung: ultrastructure and morphometric estimation of diffusion capacity. *Respiration Physiology*, 32(2): 121–140, February 1978. ISSN 0034-5687.

Karim Ghaib. *Einführung in die numerische Strömungsmechanik*. essentials. Springer Fachmedien, Wiesbaden, 2019. ISBN 978-3-658-26922-7 978-3-658-26923-4.

J. Gil, H. Bachofen, P. Gehr, and E. R. Weibel. Alveolar volume-surface area relation in air- and saline-filled lungs fixed by vascular perfusion. *Journal of Applied Physiology*, 47(5): 990–1001, November 1979. ISSN 8750-7587.

James B. Grotberg and Francesco Romanò. Computational pulmonary edema: A microvascular model of alveolar capillary and interstitial flow. *APL Bioengineering*, 7(3):036101, July 2023. ISSN 2473-2877.

J. E. Hansen and E. P. Ampaya. Human air space shapes, sizes, areas, and volumes. *Journal of Applied Physiology*, 38(6):990–995, June 1975. ISSN 8750-7587.

Roland Hausmann, Horst Bock, Teresa Biermann, and Peter Betz. Influence of lung fixation technique on the state of alveolar expansion—a histomorphometrical study. *Legal Medicine*, 6(1):61–65, March 2004. ISSN 13446223.

Chen He, Luana Micallef, Liye He, Gopal Peddinti, Tero Aittokallio, and Giulio Jacucci. Characterizing the Quality of Insight by Interactions: A Case Study. *IEEE Transactions*

on Visualization and Computer Graphics, 27(8):3410–3424, August 2021. ISSN 1941-0506.

Philipp Hofemeier, Lihi Shachar-Berman, Janna Tenenbaum-Katan, Marcel Filoche, and Josué Sznitman. Unsteady diffusional screening in 3D pulmonary acinar structures: from infancy to adulthood. *Journal of Biomechanics*, 49(11):2193–2200, July 2016. ISSN 0021-9290.

M. Horimoto, T. Koyama, H. Mishina, T. Asakura, and M. Murao. Blood flow velocity in pulmonary microvessels of bullfrog. *Respiration Physiology*, 37(1):45–59, May 1979. ISSN 0034-5687.

K Horsfield. Morphometry of the small pulmonary arteries in man. *Circulation Research*, 42(5):593–597, May 1978.

Connie C. W. Hsia. Recruitment of lung diffusing capacity: update of concept and application. *Chest*, 122(5):1774–1783, November 2002. ISSN 0012-3692.

Connie C. W. Hsia, Dallas M. Hyde, and Ewald R. Weibel. Lung Structure and the Intrinsic Challenges of Gas Exchange. *Comprehensive Physiology*, April 2016.

W. Huang, R. T. Yen, M. McLaurine, and G. Bledsoe. Morphometry of the human pulmonary vasculature. *Journal of Applied Physiology*, 81(5):2123–2133, November 1996. ISSN 8750-7587.

Jorn Hurtienne and Anja Naumann. QUESI A Questionnaire for Measuring the Subjective Consequences of Intuitive Use. In *Focus Theme: Play, Act and Learn*, page 536. 2010.

C. Jacob, S. von Mammen, T. Davison, A. Sarraf-Shirazi, V. Sarpe, A. Esmaeili, D. Phillips, I. Yazdanbod, S. Novakowski, S. Steil, C. Gingras, H. Jamniczky, B. Hallgrimsson, and B. Wright. LINDSAY Virtual Human: Multi-scale, Agent-based, and Interactive. In Joanna Kołodziej, Samee Ullah Khan, and Tadeusz Burczy´nski, editors, *Advances in Intelligent Modelling and Simulation: Artificial Intelligence-Based Models and Techniques in Scalable Computing*, Studies in Computational Intelligence, pages 327–349. Springer, Berlin, Heidelberg, 2012. ISBN 978-3-642-30154-4.

A. P. Javed, W. F. Whimster, M. H. Deverell, and M. J. Cookson. Distribution of alveolar wall per unit volume in the human lung. *Analytical cellular pathology*, 6(2):129–136, February 1994. ISSN 1878-3651.

Kent S. Kapitan. Teaching pulmonary gas exchange physiology using computer modeling. *Advances in Physiology Education*, 32(1):61–64, March 2008. ISSN 1043-4046.

M. Kawakami and T. Takizawa. Distribution of pores within alveoli in the human lung. *Journal of Applied Physiology (Bethesda, Md.: 1985)*, 63(5):1866–1870, November 1987. ISSN 8750-7587.

Mohammad F. Kiani and Antal G. Hudetz. A semi-empirical model of apparent blood viscosity as a function of vessel diameter and discharge hematocrit. *Biorheology*, 28(1-2): 65–73, January 1991. ISSN 0006-355X.

Gerasim V. Krivovichev. Computational analysis of one-dimensional models for simulation of blood flow in vascular networks. *Journal of Computational Science*, 62:101705, July 2022. ISSN 1877-7503.

Vladimir Kulish. *Human Respiration: Anatomy and Physiology, Mathematical Modeling, Numerical Simulation and Applications*. WIT Press, 2006. ISBN 978-1-85312-944-5.

S. L. Lindstedt. Pulmonary transit time and diffusing capacity in mammals. *American Journal of Physiology-Regulatory, Integrative and Comparative Physiology*, 246(3):R384–R388, March 1984. ISSN 0363-6119.

M. Matsuda, Y. C. Fung, and S. S. Sobin. Collagen and elastin fibers in human pulmonary alveolar mouths and ducts. *Journal of Applied Physiology (Bethesda, Md.: 1985)*, 63(3): 1185–1194, September 1987. ISSN 8750-7587.

R. R. Mercer, M. L. Russell, and J. D. Crapo. Alveolar septal structure in different species. *Journal of Applied Physiology (Bethesda, Md.: 1985)*, 77(3):1060–1066, September 1994. ISSN 8750-7587.

Wolter Mooi and C. A. Wagenvoort. Decreased numbers of pulmonary blood vessels: Reality or artifact? *The Journal of Pathology*, 141(4):441–447, 1983. ISSN 1096-9896.

Morten Moshagen and Meinald T. Thielsch. Facets of visual aesthetics. *International Journal of Human-Computer Studies*, 68(10):689–709, October 2010. ISSN 1071-5819.

Christian Mühlfeld. Stereology and three-dimensional reconstructions to analyze the pulmonary vasculature. *Histochemistry and Cell Biology*, 156(2):83–93, August 2021. ISSN 1432-119X.

Christian Mühlfeld, Ewald R. Weibel, Ute Hahn, Wolfgang Kummer, Jens R. Nyengaard, and Matthias Ochs. Is Length an Appropriate Estimator to Characterize Pulmonary Alveolar Capillaries? A Critical Evaluation in the Human Lung. *The Anatomical Record*, 293(7): 1270–1275, 2010. ISSN 1932-8494.

Y Nagasaka, J Bhattacharya, S Nanjo, M A Gropper, and N C Staub. Micropuncture measurement of lung microvascular pressure profile during hypoxia in cats. *Circulation Research*, 54(1):90–95, January 1984.

Anja Naumann and Jörn Hurtienne. Benchmarks for intuitive interaction with mobile devices. In *Proceedings of the 12th international conference on Human computer interaction with mobile devices and services - MobileHCI '10*, page 401, Lisbon, Portugal, 2010. ACM Press. ISBN 978-1-60558-835-3.

Matthias Ochs, Jens R. Nyengaard, Anja Jung, Lars Knudsen, Marion Voigt, Thorsten Wahlers, Joachim Richter, and Hans Jørgen G. Gundersen. The number of alveoli in the human lung. *American Journal of Respiratory and Critical Care Medicine*, 169(1): 120–124, January 2004. ISSN 1073-449X.

Herbert Oertel, Martin Böhle, and Thomas Reviol. *Strömungsmechanik: für Ingenieure und Naturwissenschaftler*. Springer Fachmedien, Wiesbaden, 2015. ISBN 978-3-658-07785-3 978-3-658-07786-0.

O Okada, R. G. Presson Jr, K. R. Kirk, P. S. Godbey, R. L. Capen, and W. W. Wagner Jr. Capillary perfusion patterns in single alveolar walls. *Journal of Applied Physiology*, May 1992.

Kathleen Pagana, Timothy Pagana, and Theresa Pagana. *Mosby's Diagnostic and Laboratory Test Reference*. Elsevier, 14 edition, 2019.

Johan Petersson and Robb W. Glenny. Gas exchange and ventilation–perfusion relationships in the lung. *European Respiratory Society*, 2014.

F. Pierigè, S. Serafini, L. Rossi, and M. Magnani. Cell-based drug delivery. *Advanced Drug Delivery Reviews*, 60(2):286–295, January 2008. ISSN 0169-409X.

William A. Pike, John Stasko, Remco Chang, and Theresa A. O'Connell. The Science of Interaction. *Information Visualization*, 8(4):263–274, January 2009. ISSN 1473-8716.

A.R. Pries, T.W. Secomb, and P. Gaehtgens. Biophysical aspects of blood flow in the microvasculature1. *Cardiovascular Research*, 32(4):654–667, October 1996. ISSN 0008-6363.

K. K. Pump. The Circulation in the Peripheral Parts of the Human Lung. *Diseases of the Chest*, 49(2):119–129, February 1966. ISSN 0096-0217.

Osborne Reynolds. An experimental investigation of the circumstances which determine whether the motion of water shall be direct or sinuous, and of the law of resistance in

parallel channels. *Philosophical Transactions of the Royal Society of London*, 174:935–982, March 1883.

A F Riggs. The Bohr Effect. *Annual Review of Physiology*, 50(1):181–204, 1988.

J. Rotta. Experimenteller Beitrag zur Entstehung turbulenter Strömung im Rohr. *Ingenieur-Archiv*, 24(4):258–281, July 1956. ISSN 1432-0681.

F. J. W. Roughton and R. E. Forster. Relative Importance of Diffusion and Chemical Reaction Rates in Determining Rate of Exchange of Gases in the Human Lung, With Special Reference to True Diffusing Capacity of Pulmonary Membrane and Volume of Blood in the Lung Capillaries. *Journal of Applied Physiology*, September 1957.

Bernard Sapoval, Min-Yeong Kang, and Anh Tuan Dinh-Xuan. Modeling of Gas Exchange in the Lungs. *Comprehensive Physiology*, 11(1):1289–1314, December 2020. ISSN 2040-4603.

Dieter Schlosser, Ernst Heyse, and Heinz Bartels. Flow rate of erythrocytes in the capillaries of the lung. *Journal of Applied Physiology*, 20(1):110–112, January 1965. ISSN 8750-7587.

Kerstin Schmid, Andreas Knote, Alexander Mück, Keram Pfeiffer, Sebastian von Mammen, and Sabine C. Fischer. Interactive, Visual Simulation of a Spatio-Temporal Model of Gas Exchange in the Human Alveolus. *Frontiers in Bioinformatics*, 1, 2022. ISSN 2673-7647.

D. E. Schraufnagel, D. Mehta, R. Harshbarger, K. Treviranus, and N. S. Wang. Capillary remodeling in bleomycin-induced pulmonary fibrosis. *The American Journal of Pathology*, 125(1):97, October 1986.

Rüdiger Schwarze. *CFD-Modellierung*. Springer, Berlin, Heidelberg, 2013. ISBN 978-3-642-24377-6 978-3-642-24378-3.

Timothy W. Secomb. Mechanics and computational simulation of blood flow in microvessels. *Medical engineering & physics*, 33(7):800–804, September 2011. ISSN 1350-4533.

Sandeep Sharma, Muhammad F. Hashmi, and Bracken Burns. Alveolar Gas Equation. In *StatPearls*. StatPearls Publishing, Treasure Island (FL), 2020.

Xiuhua April Si and Jinxiang Xi. Pulmonary Oxygen Exchange in a Rhythmically Expanding–Contracting Alveolus–Capillary Model. *Journal of Respiration*, 2(4):159–173, November 2022. ISSN 2673-527X.

S. S. Sobin, H. M. Tremer, and Y. C. Fung. Morphometric basis of the sheet-flow concept of the pulmonary alveolar microcirculation in the cat. *Circulation Research*, 26(3):397–414, March 1970. ISSN 0009-7330.

Sidney S. Sobin, Y. C. Fung, Herta M. Tremer, and Thomas H. Rosenquist. Elasticity of the Pulmonary Alveolar Microvascular Sheet in the Cat. *Circulation Research*, 30(4): 440–450, April 1972.

Luisa Costa Sousa, Catarina F. Castro, and Carlos Conceição António. Blood Flow Simulation and Applications. In Renato M. Natal Jorge, João Manuel R. S. Tavares, Marcos Pinotti Barbosa, and A.P. Slade, editors, *Technologies for Medical Sciences*, Lecture Notes in Computational Vision and Biomechanics, pages 67–86. Springer Netherlands, Dordrecht, 2012. ISBN 978-94-007-4068-6.

Hagit Stauber, Dan Waisman, Netanel Korin, and Josué Sznitman. Red blood cell dynamics in biomimetic microfluidic networks of pulmonary alveolar capillaries. *Biomicrofluidics*, 11 (1):014103, January 2017. ISSN 1932-1058.

K. C. Stone, R. R. Mercer, P. Gehr, B. Stockstill, and J. D. Crapo. Allometric relationships of cell numbers and size in the mammalian lung. *American Journal of Respiratory Cell and Molecular Biology*, 6(2):235–243, February 1992. ISSN 1044-1549.

Arata Tabuchi, Beata Styp-Rekowska, Arthur S. Slutsky, Peter D. Wagner, Axel R. Pries, and Wolfgang M. Kuebler. Precapillary Oxygenation Contributes Relevantly to Gas Exchange in the Intact Lung. *American Journal of Respiratory and Critical Care Medicine*, 188(4): 474–481, June 2013. ISSN 1073-449X.

Masahiro Toshima, Yuko Ohtani, and Osamu Ohtani. Three-dimensional architecture of elastin and collagen fiber networks in the human and rat lung. *Archives of Histology and Cytology*, 67(1):31–40, March 2004. ISSN 0914-9465.

Harun Tuğcu, Gülşin Canoğullari, Yıldırım Karslioğlu, Yasemin Günay Balci, Kubilay Uzuner, and Coşkun Yorulmaz. Comparison of the Effects of Two Different Fixation Methods on Lung Morphology: An Experimental Study. *Turkiye Klinikleri Journal of Medical Sciences*, 33(1):177–183, 2013. ISSN 1300-0292, 2146-9040.

J. Tworek, H. Jamniczky, C. Jacob, B. Hallgrímsson, and Bruce Wright. The LINDSAY Virtual Human Project: An immersive approach to anatomy and physiology. *Anatomical sciences education*, 2013.

H K Versteeg and W Malalasekera. *An Introduction to Computational Fluid Dynamics. The finite volume method.* Pearson Education Limited, 2 edition, 2007. ISBN 978-0-13-127498-3.

P. D. Wagner. Ventilation/perfusion relationships. *Clinical Physiology (Oxford, England)*, 1 (5):437–451, October 1981. ISSN 0144-5979.

Ewald R. Weibel. Morphometric estimation of pulmonary diffusion capacity: I. Model and method. *Respiration Physiology*, 11(1):54–75, December 1970. ISSN 0034-5687.

Ewald R. Weibel. What makes a good lung? *Swiss Medical Weekly*, 139(27-28):375–386, July 2009. ISSN 1424-7860.

Ewald R. Weibel, William J. Federspiel, Fabienne Fryder-Doffey, Connie C. W. Hsia, Martin König, Vilma Stalder-Navarro, and Ruth Vock. Morphometric model for pulmonary diffusing capacity I. Membrane diffusing capacity. *Respiration Physiology*, 93(2):125–149, August 1993. ISSN 0034-5687.

John B. West. *Respiratory physiology: the essentials*. Wolters Kluwer Health/Lippincott Williams & Wilkins, Philadelphia, 9th ed edition, 2012. ISBN 978-1-60913-640-6.

T. Winkler, A. Krause, and S. Kaiser. Simulation of mechanical respiration using a multicompartment model for ventilation mechanics and gas exchange. *International Journal of Clinical Monitoring and Computing*, 12(4):231–239, 1995. ISSN 0167-9945.

R T Yen and Y C Fung. Model experiments on apparent blood viscosity and hematocrit in pulmonary alveoli. *Journal of Applied Physiology*, 35(4):510–517, October 1973. ISSN 8750-7587, 1522-1601.

F. Y. Zhuang, M. R. T. Yen, Y. C. Fung, and S. S. Sobin. How many pulmonary alveoli are supplied by a single arteriole and drained by a single venule? *Microvascular Research*, 29(1):18–31, January 1985. ISSN 0026-2862.

Pablo Zurita and Daniel E. Hurtado. Computational modeling of capillary perfusion and gas exchange in alveolar tissue. *Computer Methods in Applied Mechanics and Engineering*, 399:115418, September 2022. ISSN 0045-7825.

Appendix A

Supplements

S.1 Questionnaire for evaluation of the integration of *Alvin* in a university level physiology lab course

The questionnaire was translated from the German original.

Demographics

In this section, we ask you to answer questions for general demographic information. These are relevant for a correct interpretation of your further answers.

1. Please indicate your age.
2. Please indicate your biological sex.
3. Do you have a visual impairment and will it be compensated for while using the system?
4. Are you affected by color vision deficiency or color blindness?
5. What handedness do you have?
6. On average, how often do you use the following media?
    - Internet
    - Computer (in general)
    - Computer games
    - Smartphone
    - Tablet
7. How would you rate your fluency in German?

In this section, we ask you to answer questions about your prior knowledge in the subject area of the course and regarding your previous educational background.

8. In the context of which study program are you attending this event?
9. What semester are you in?
10. Did you attend the Human Biology lecture in the summer semester of 2020?
11. Have you studied the literature recommended in the above lecture on the subject of respiration?
    - N.A. Campbell and J.B. Reece. *Biology*. Always learning. Pearson Deutschland, 2015. ISBN: 9783868942590.
    - Robert F. Schmidt, Florian Lang, and Manfred Heckmann. *Physiologie des Menschen*. Springer-Lehrbuch. Springer-Verlag Berlin Heidelberg, 2011. ISBN: 978-3-642-01651-6.
12. Do you have other relevant prior knowledge from other sources?
    - School
    - Apprenticeship
    - Personal initiative

Subject-related exercises

In this group of questions, you will be given tasks that you can answer using the system. We ask you to discuss comments on the use of the app only in a joint round at the end of the event in order to minimize influencing the other participants. Now, familiarize yourself with the application. Look at how the graphs change in response to the controllers. Also observe how different disease patterns affect the values.

1. Which correlations between the course of the oxygen saturation curve ("Oxygen saturation along capillary") and the visualized simulation can you identify?

In this and the following blocks of questions, you will be given tasks to answer using the system. After each task (there are 3 tasks in total, each with subtasks), the answers will be discussed in plenary. We ask you to discuss comments on the use of the application only in a joint round at the end of the event in order to minimize influencing the other participants.

2. How does the oxygen dissociation curve change, when the body temperature rises to 40 °C (fever)?

3. How does this affect the ability of hemoglobin to bind oxygen in the lungs?

4. How does it affect the ability of hemoglobin to deliver oxygen to tissues?

Fever is normally accompanied by an increase in respiratory rate. By increasing the respiratory rate, the increased CO_2 produced by the increased metabolism during fever can be better exhaled. The partial pressure of CO_2 in the blood affects the ability of hemoglobin to bind O_2.

5. By how many mmHg must the venous CO_2 partial pressure be lowered to achieve the same oxygen saturation at 40 ℃ as at 37 °?

The cruising altitude of passenger aircrafts is around 10 to 13 km. At this altitude, the partial pressure of oxygen is only between 30 and 44 mmHg. Therefore, the air pressure in the cabins of passenger aircrafts is artificially increased, but only to a level corresponding to the air pressure at about 2000-2500 m above sea level. Thus, an oxygen partial pressure of approx. 60 mmHg is achieved in venous blood.

6. What oxygen saturation does this correspond to?

7. At what alveolar pO_2 can a healthy person achieve this?

8. What oxygen saturation does the blood of a patient suffering from COPD reach at the same atmospheric pressure?

9. What happens to the oxygen saturation of a person suffering from COPD if he or she develops a fever during a flight?

In this block of questions, you will be given tasks to answer using the system. Please configure the application using the activation code provided in the lecture. We ask that you do not discuss comments on the use of the application until a joint round at the end of the course to minimize influencing the other participants.

10. Sometimes a lung has to be surgically removed due to a disease. What effects does this have on the oxygen saturation of the blood?

In tissues with very high metabolic rates, for example heavily used muscles, the CO_2 concentration can increase.

11. How does this affect the oxygen dissociation curve?

12. How does it affect oxygen uptake in the lungs and oxygen delivery in the tissues?

Start two simulation instances with the parameters for a healthy person. Increase the partial pressure of CO_2 in the arterial blood of one instance to 75 mmHg. Using the oxygen dissociation curves, measure the absorbed oxygen in the lungs and the delivered oxygen in the tissues.

13. At which blood pCO_2 is more oxygen available to the tissue? This phenomenon is called the Bohr effect.

Athletes, especially high-altitude mountaineers, can adapt to conditions at high altitude by training for longer periods at low oxygen partial pressure. This increases the diphosphoglycerate (DPG) concentration in the erythrocytes. Now, we would like to understand why this is beneficial. Start a simulation instance with the parameters for a healthy subject. First, reconstruct the conditions that exist when climbing at high altitudes: Decrease atmospheric pressure until alveolar pO_2 drops to a low value such as 40 mmHg. Arterial pO_2 is also reduced in these conditions. Set this to 30 mmHg.

14. What is the oxygen saturation of the blood?

Duplicate the instance. Now, set the DPG concentration in one of the two instances to the maximum value (adjustment to high altitude).

15. What happens to the oxygen dissociation curve?

16. What happens to the oxygen saturation of the blood?

17. The effect you observed initially appears to be rather disadvantageous. Now, measure the oxygen saturation in the lungs and in the tissue in the respective graphs and determine the difference between these values.

The questions will now be discussed in the plenum of the event. We ask you to discuss comments on the use of the application only in a joint round at the end of the event to minimize influencing the other participants.
The phase of active use of the system is now complete. In the following, we ask you to answer questions about your user experience. This is for systematic evaluation of the system. Please note that for the first two questions a "soft" inquiry will appear if you do not answer them or answer them only partially. The corresponding groups of questions are standardized questionnaires, where a complete answer has a lot of value. Of course, you can still skip them unanswered if you wish.

QUESI – Questionnaire for Measuring the Subjective Consequences of Intuitive Use

This is a standardized questionnare (Hurtienne and Naumann, 2010). Try to base your assessment of the system solely on the use of the system (and not, for example, on the difficulty of the task itself). There are no right or wrong answers. Please answer spontaneously and do not omit any questions.
Answer scale with equidistant levels: 1 = "Fully disagree", 2 = "Mainly disagree", 3 = "Neutral", 4 = "Mainly agree", 5 = "Fully agree".

1. I could use the system without thinking about it.
2. I achieved what I wanted to achieve with the system.
3. The way the system worked was immediately clear to me.
4. I could interact with the system in a way that seemed familiar to me.
5. No problems occurred when I used the system.
6. The system was not complicated to use.
7. I was able to achieve my goals in the way I had imagined to.
8. The system was easy to use from the start.
9. It was always clear to me what I had to do to use the system.
10. The process of using the system went smoothly.
11. I barely had to concentrate on using the system.
12. The system helped me to completely achieve my goals.
13. How the system is used was clear to me straight away.
14. I automatically did the right thing to achieve my goals.

Visawi-s - Visual Aesthetics of Websites Inventory- short version

This is a standardized questionnare (Moshagen and Thielsch, 2010). On a scale of 1 (strongly disagree) to 7 (strongly agree), please rate the extent to which you agree with the following statements regarding the system.

1. The layout appears too dense. (r)

2. The layout is pleasantly varied.
3. The color composition is attractive.
4. The layout appears professionally designed.
5. The layout is easy to grasp.
6. The layout is inventive.
7. The colors do not match. (r)
8. The layout is not up-to-date. (r)
9. Everything goes together on this site.
10. The design appears uninspired. (r)
11. The choice of colors is botched. (r)
12. The site is designed with care.
13. The site appears patchy. (r)
14. The layout appears dynamic.
15. The colors are appealing.
16. The design of the site lacks a concept. (r)
17. The layout appears well structured.
18. The design is uninteresting. (r)

Negatively-keyed items are indicated by (r) and are reverse-scored.

Customized questions on the use of *Alvin*

1. On a scale of 1 (strongly disagree) to 7 (strongly agree), please rate the extent to which you agree with the following statements regarding the system.
    - I frequently changed the "Incoming Deoxygenated Blood" parameter values for completing the tasks.
    - I frequently changed the "Alveolar Space" parameter values for completing the tasks.

- I frequently changed the "Tissue Structure" parameter values for completing the tasks.
- The system supported me in the configuration and interpretation of the parameters.
- I was confused by the information provided by the system.
- Assessment of the parameter values was useful for my understanding of the processes.
- I found the ability to create, configure, and compare multiple instances useful.
- I found the ability to copy instances useful.
- I found the ability to reset instances to initial configuration useful.
- I have used the output graphs frequently during my use of the system.
- I could easily extract the information relevant to me from the graphs.
- I regularly read the exact numerical values of a plot using the mouse-over function.
- I found the visual highlighting of the simulated components of the alveolus when the cursor was over a parameter group helpful.
- I found the visual highlighting distracting.
- I have disabled visual highlighting for most of the time I used it.
- I found the ability to reset the simulation time helpful.
- The mouse-over tooltips help assisted me in using the system.

2. On which device or which version(s) of the system did you use? You can use detailed information and multiple selections if, for example, you used multiple usage paths. Detailed information about the operating system (for example, "Windows 10 version 1903", "macOS 10.13"), as well as the device (for example, processor (i5-5700) or graphics card (GeForce 2 MX), or computer model (MacBookPro Late 2015)) or browser (for example, Firefox 83.0, Safari 12) is helpful, especially if problems occurred.
    - Windows Desktop (.exe)
    - macOS Desktop (.app)
    - Linux Desktop
    - Browser (WebGL)
    - iOS Tablet
    - Android Tablet
    - iOS Smartphone
    - Android Smartphone

3. On a scale of 1 (strongly disagree) to 7 (strongly agree), please rate the extent to which you agree with the following statements regarding the system.

- The system responded to my input immediately.
- Animations were smooth and without annoying leaps.
- The performance of the system affected my desired use.

4. Which benefits do you see in this system compared to a traditional text book?
5. For which topics from your previous studies would you have appreciated a comparable application?
6. Assuming you'll be teaching physiology - Could you imagine integrating this application into your own teaching?
7. Could you imagine using a similar system on an appropriate topic in your classes (or a similar event)?
8. Please share general comments, suggestions and feedback.

S.2 Connectivity analyses

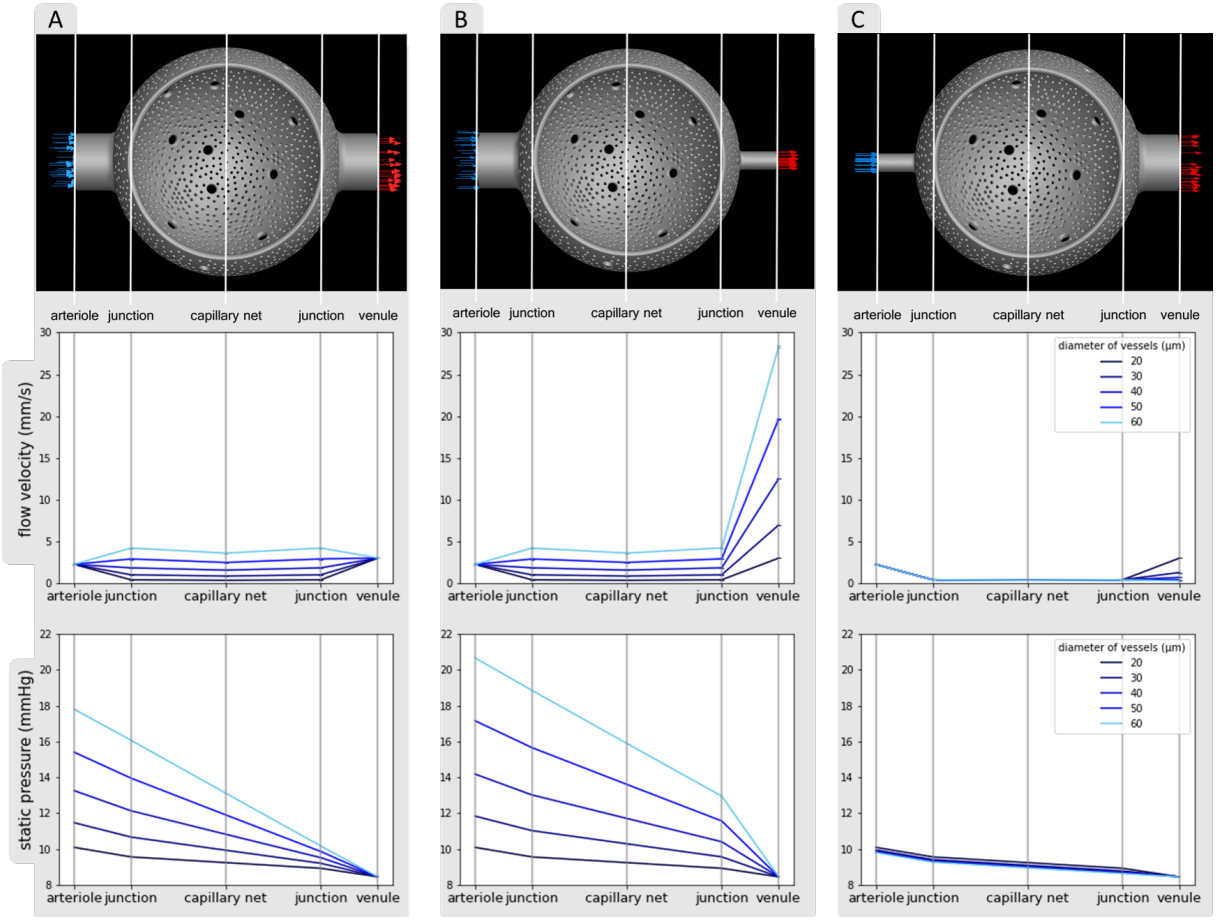

Figure S.1: Flow velocity and static pressure were assessed at various locations within the system: Specifically, at the arteriole (inlet), the junction connecting the arteriole and the capillary net, the central region of the capillary net, the junction connecting the capillary net and venule, and finally at the venule (outlet). Three sets of models were compared, differing in whether the diameters of A) arterioles and venules, B) arterioles only or C) venules only were varied.

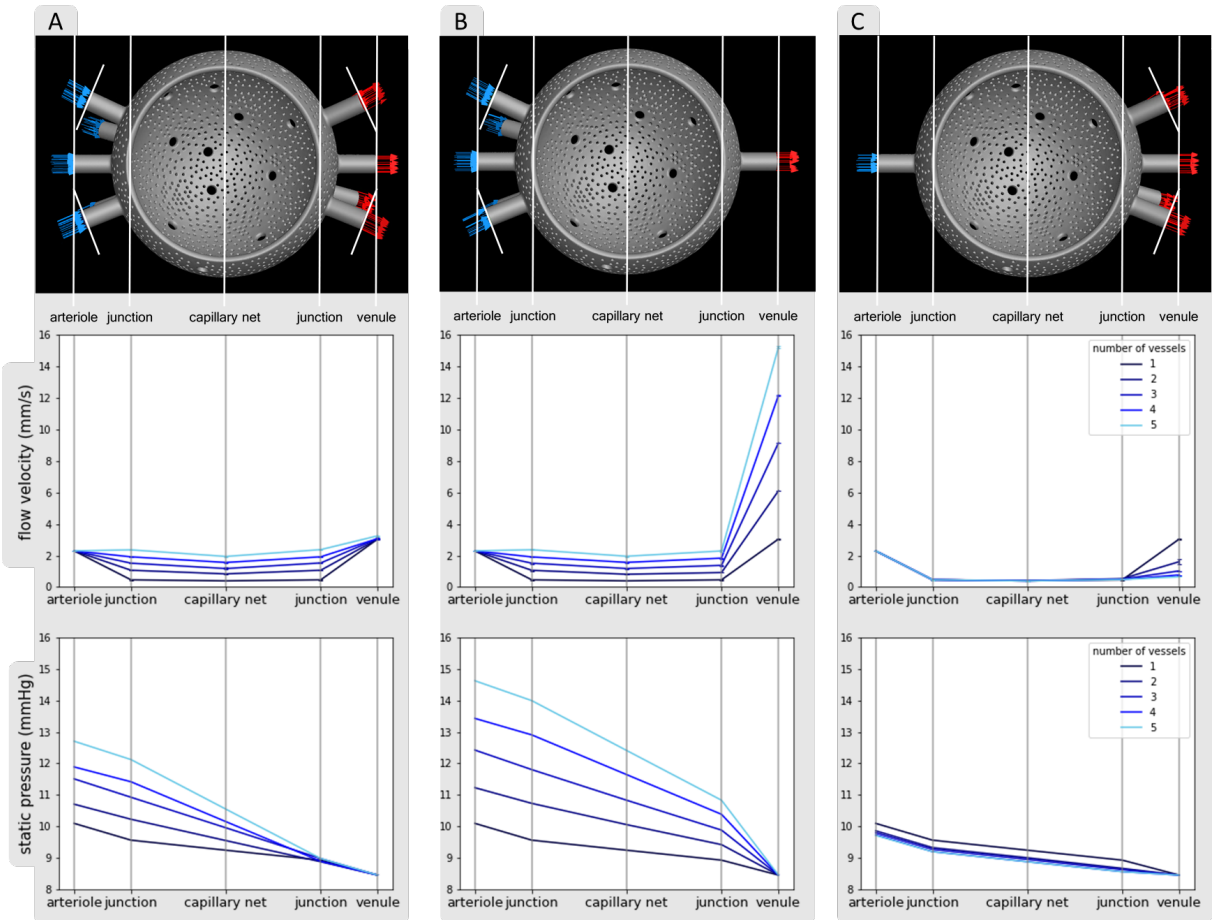

Figure S.2: Flow velocity and static pressure were assessed at various locations within the system: Specifically, at the arteriole (inlet), the junction connecting the arteriole and the capillary net, the central region of the capillary net, the junction connecting the capillary net and venule, and finally at the venule (outlet). Three sets of models were compared, differing in whether the number of A) arterioles and venules, B) arterioles only or C) venules only were varied.

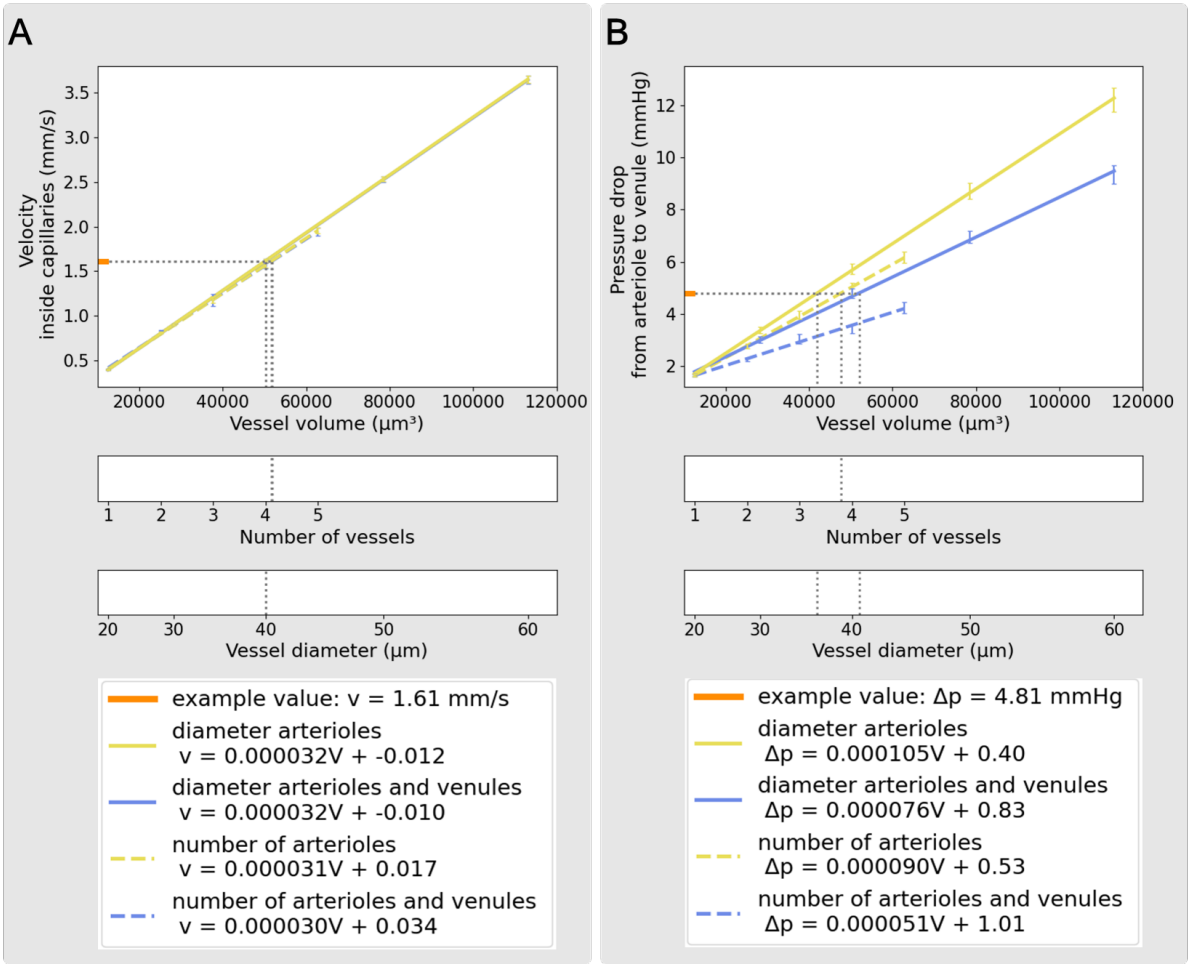

Figure S.3: Inference of vessel arrangement from mean flow velocity within capillaries and pressure drop from arteriole to venule. The simulation results from a model with a single arteriole and a single venule, each 40 µm in diameter, were chosen as an example pair of values (orange). Regression analyses yielded quantitative relationships between the target values and the arrangement of arterioles and venules in our models. These arrangements comprise variations in the number (dashed) or diameter (continuous) of solely arterioles (yellow) or both arterioles and venules (blue). A) In terms of the mean flow velocity within capillaries, the regression curves for the different model geometries overlap. B) The regression curves for pressure drop of the different model types are distiguishable. Simulations were performed with a Newtonian viscosity model.

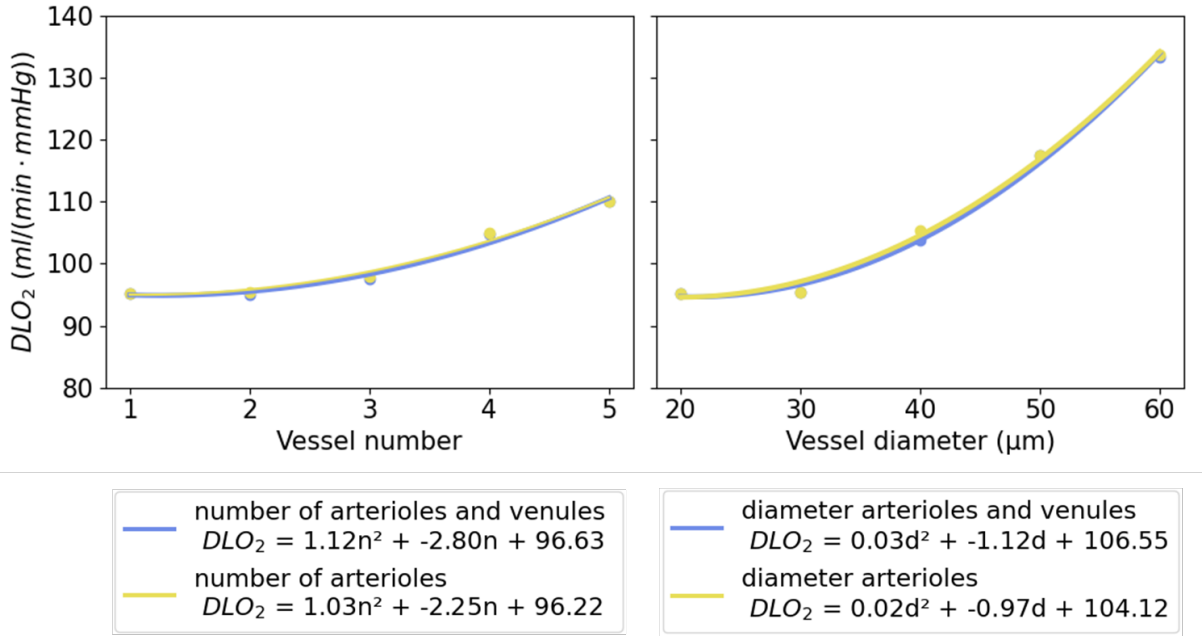

Figure S.4: The pulmonary diffusion capacity for oxygen (DLO_2) was estimated in *Alvin* for various blood flow velocities corresponding to different connectivity models. These flow velocity values were specified based on the results obtained from simulations using the Newtonian viscosity model. Comparisons were made between models featuring symmetric (blue) and asymmetric (yellow) arteriolar configurations, and regression analyses were conducted to assess the non-linear relationship between DLO_2 and vessel configurations.

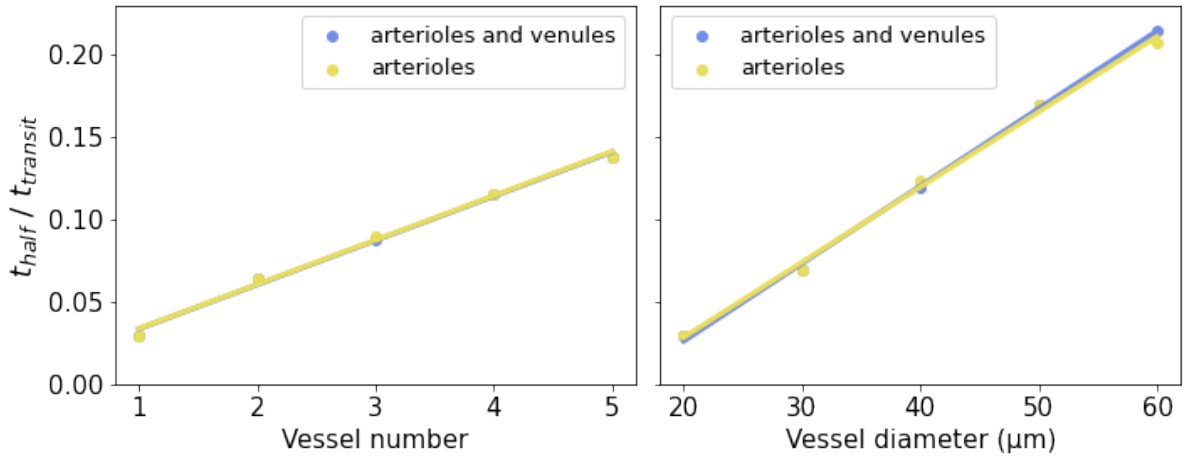

Figure S.5: The reaction half-time, normalized to the transit time (t_{half} / $t_{transit}$), was estimated in *Alvin* for various blood flow velocities corresponding to different connectivity models. These flow velocity values were specified based on the results obtained from simulations using the Newtonian viscosity model. Comparisons were made between models featuring symmetric (blue) and asymmetric (yellow) arteriolar configurations, and regression analyses were conducted to assess the linear relationship between t_{half} / $t_{transit}$ and vessel configurations.

Eidesstattliche Erklärungen nach §7 Abs. 2 Satz 3, 4, 5 der Promotionsordnung der Fakultät für Biologie

Eidesstattliche Erklärung

Hiermit erkläre ich an Eides statt, die Dissertation: **„Integrative, dreidimensionale *in silico* Modellierung des Gasaustauschs in der menschlichen Alveole“**, eigenständig, d. h. insbesondere selbständig und ohne Hilfe eines kommerziellen Promotionsberaters, angefertigt und keine anderen, als die von mir angegebenen Quellen und Hilfsmittel verwendet zu haben.
Ich erkläre außerdem, dass die Dissertation weder in gleicher noch in ähnlicher Form bereits in einem anderen Prüfungsverfahren vorgelegen hat.
Weiterhin erkläre ich, dass bei allen Abbildungen und Texten bei denen die Verwertungsrechte (Copyright) nicht bei mir liegen, diese von den Rechtsinhabern eingeholt wurden und die Textstellen bzw. Abbildungen entsprechend den rechtlichen Vorgaben gekennzeichnet sind sowie bei Abbildungen, die dem Internet entnommen wurden, der entsprechende Hypertextlink angegeben wurde.

Affidavit

I hereby declare that my thesis entitled: **„Integrative, three-dimensional *in silico* modeling of gas exchange in the human alveolus”** is the result of my own work. I did not receive any help or support from commercial consultants. All sources and / or materials applied are listed and specified in the thesis.
Furthermore I verify that the thesis has not been submitted as part of another examination process neither in identical nor in similar form.
Besides I declare that if I do not hold the copyright for figures and paragraphs, I obtained it from the rights holder and that paragraphs and figures have been marked according to law or for figures taken from the internet the hyperlink has been added accordingly.

Würzburg, March 11, 2024 Kerstin Schmid .....